DOCTOR OF PHILOSOPHY

Design and Multi-physical Fields Analysis of High Speed Permanent Magnet Machines

Zhang, Yue

Award date:
2018

Awarding institution:
Queen's University Belfast

Design and Multi-physical Fields Analysis of High Speed Permanent Magnet Machines

By

Yue Zhang

A thesis presented on application for the degree of

Doctor of Philosophy

School of Electronics, Electrical Engineering and Computer Science

The Queen's University of Belfast

September 2018

To my parents

Acknowledgements

I would like to acknowledge everyone who has knowingly and unknowingly helped me and wished me the best in successfully accomplishing this research.

I would like to express my particular thanks to Professor Seán McLoone. His supportive encouragement and supervision have been extremely helpful and essential, and make my study and life in Queens University Belfast become a wonderful experience. My sincere gratitude also goes to Professor Wenping Cao for his help and support to me.

I would like to thank the Engineering and Physical Sciences Research Council (EPSRC) for their sponsorship of this research (Reference: EPSRC/D9103URO).

I would like to give my special thanks to my parents for their invaluable support and encouragement.

Abstract

Due to the advantages of high power density, high efficiency and compact size, high speed permanent magnet machines (HSPMMs) have found wide application in industrial areas. Compared with a conventional speed permanent magnet machine, a HSPMM rotor can reach speeds of more than 10,000 rpm, which brings challenges with regard to electromagnetic, thermal and mechanical aspects of machine design. The higher power density also results in larger power loss per unit volume; due to the small machine size, machine thermal dissipation becomes difficult. Moreover, air frictional loss rises dramatically when the rotor is in high speed operation and this may also further increase rotor temperature. Therefore, research into HSPMM power losses and improving machine thermal dissipation capability is of significant interest. HSPMM mechanical issues also need to be considered to ensure safe and reliable machine operation. As rotor speeds rise, rotor strength becomes prominent and critical as the permanent magnets are vulnerable to the large centrifugal force. In addition, the machine rotor should also have enough rigidity and avoid operating at critical speeds. As such, this dissertation focuses on HSPMM design and research. Multi-physical fields analysis of a HSPMM is carried out to calculate machine power losses and temperature distribution, with factors influencing machine performance considered; HSPMM rotor mechanical research and analysis are also carried out and presented in this study.

Firstly, the HSPMM design methodology and process are illustrated with machine rotor parameters, PM material, pole numbers and rotor sleeve considered for a 150 kW, 17000 rpm HSPMM. Then, HSPMM performance for different machine stator structures and PM pole arc pole pitches is investigated using the Finite Element Method (FEM) for the machine operating at both no load and full load conditions; HSPMM electromagnetic performance and how it is impacted by machine parameters is also studied.

HSPMM power losses are comprehensively investigated in the following chapter. As machine core loss can be significantly increased with increasing machine frequency, it is critical to accurately estimate HSPMM iron loss. Based on the machine iron core

magnetic field variation that is obtained by FEM analysis, machine steel iron core loss estimation for HSPMM is performed using an improved method with the influences of alternating and rotating magnetic fields, as well as harmonics effects, considered for high precision. Then the HSPMM air gap magnetic flux density distribution considering machine stator slotting effect is also analytically calculated with its effectiveness verified by FEM results.

Then rotor eddy current loss is studied by time-stepping FEM, while the effects of rotor sleeve dimensions and properties, copper shielding composite rotor structure, air gap length, as well as slot opening width are further researched in depth. A PM bevelling method is also proposed and investigated to reduce HSPMM rotor eddy current loss while having little effect on machine output torque. Then a fluid field analysis is carried out to study HSPMM rotor air frictional loss when the rotor is in high speed operation.

According to the characteristics of a machine axial forced air cooling system, the HSPMM temperature distribution is investigated by 3-D fluid–thermal coupling CFD modelling with the calculated power losses results. The machine thermal analysis theory and modelling method are also detailed and further explained. HSPMM thermal performance variation due to impacting factors of cooling air velocity, rotor eddy current loss and sleeve thermal conductivity are also comprehensively investigated and studied in this dissertation. The designed HSPMM is prototyped, and temperature experimental tests are also carried out to verify the effectiveness of the research and analysis for HSPMM.

Then, thick-walled cylinder theory is introduced to study rotor mechanical strength analytically, while it also verifies the FEM calculation results. Then based on FEM analysis, HSPMM rotor stress distribution is investigated with sleeve material effects on rotor strength discussed. In order to alleviate the rotor sleeve stress, three pole filler materials are comparatively studied, while the temperature impacts on rotor mechanical stress is further considered; sleeve thickness and the interference between PM and sleeve are investigated in an integrated fashion for HSPMM rotor strength analysis, with some conclusions also drawn for HSPMM rotor mechanical design. HSPMM rotor critical speeds are also calculated by the established 3D rotor dynamic analysis FEM model to ensure the rotor is operating in a desirable condition.

Key words: High speed permanent magnet machine, power loss, thermal analysis, rotor design, multi-physical analysis

Nomenclature

Symbols

B_0	Nominal Flux Density
B_m	Flux Density Amplitude
B_r	Radial Component of Flux Density
B_t	Tangential Component of Flux Density
C_{fe}	Calibration Factor
E	Young's Modulus
G_{fe}	Iron Core Weight
H_r	Radial Component of Magnet Field Intensity
H_θ	Tangential Component of Magnet Field Intensity
J	Eddy Current Density
K_0	Specific Iron Loss at Nominal Flux Density
K_c	Carter Coefficient
K_a	Anomalous Loss Coefficient
K_e	Eddy current Loss Coefficient
K_h	Hysteresis Loss Coefficient
K_{dv}	Winding Distribution Factor
K_{pv}	Winding Pitch Factor
K_{slv}	Slot Opening Factor

M	Magnetization Vector
M_r	Radial Magnetization Vector
M_θ	Tangential Magnetization Vector
N	Winding Turns In Series Per Phase
N_u	Nusselt Number
P_a	Anomalous Loss
P_e	Eddy current Loss
P_{exc}	Excessive Loss
P_h	Hysteresis Loss
P_{iron}	Iron Loss
P_r	Prandtl Number
Q_s	Stator Slot Number
R_a	Rayleigh Number
R_e	Reynolds Number
R_m	Magnet Outer radius
R_r	Rotor Core Outer Radius
R_s	Stator Bore Radius
T_{cog}	Cogging Torque
Y_p	Winding Coil Pitch
b_0	Stator Slot Opening Width
f_0	Nominal Frequency

f	Frequency
g	Air Gap Length
h_m	Magnet Thickness
p	Pole Pair Number
q	Slot Number Per Pole Per Phase
v_{fl}	Fluid speed
α	Steinmetz Coefficient; Heat Transfer Coefficient
α_m	Pole Arc to Pole Pitch Factor
μ	Permeability; Fluid Viscosity; Poisson's Ratio
μ_0	Free Space Permeability
μ_r	Relative Permeability
μ_t	Turbulence Viscosity Factor
ρ	Resistivity; Density
Λ	Permeance Function Coefficient
φ	Scalar Magnetic Potential
δ	Fit Shrink Range
λ	Fluid Thermal Conductivity
ε	Turbulence Consuming Ratio
σ	Electrical Conductivity; Strain
σ_{equ}	Equivalent Stress
σ_r	Stress in radial

σ_θ	Stress in Tangential
ω	Angular Velocity

Abbreviations

2D	Two Dimensional
3D	Three Dimensional
BLAC	Brushless AC Machine
BLDC	Brushless DC Machine
CFD	Computational Fluid Dynamics
CTE	Coefficient of Thermal Expansion
EMF	Electromotive Force
FDM	Finite Difference method
FEM	Finite Element Method
FFT	Fast Fourier Transform
GCD	Greatest Common Divisor
HSPMM	High Speed Permanent Magnet Machine
IM	Induction Machine
LPTN	Lumped-Parameter Thermal Network
MMF	Magnetomotive Force
NdFeB	Neodymium-Iron-Boron
PM	Permanent Magnet
RANS	Reynolds-Averaged Navier-Stokes
SmCo	Samarium-Cobalt
SRM	Switched Reluctance Machine

SST	Single Sheet Tester
TFFEA	Time-Frequency Finite Element Analysis
rpm	Resolution(s) Per Minute

Contents

Chapter 1
Introduction

This chapter firstly introduces the background of the research, as well as the major research topics for high speed machines. The main contributions of the research work are presented, with the outline of the thesis followed. Then the publications of the research are listed.

1.1 Introduction

High speed machines have been extensively and intensively researched in recent years with the development of new materials and the advances in high frequency electrical switching devices. High speed machines have already been found widely utilized in multiple industrial applications, such as centrifugal compressors, electrical turbochargers, blowers, pumps, distributed generation, flywheel energy storage systems, aero engines, spindles, machine tools, grinding machines, mixers and so on [1-9]. A high speed machine is defined as a machine whose rated rotational speed can be in excess of 10,000 rpm or where the multiplication of operational speed with the

square root of power (rpm$\times\sqrt{\text{kW}}$) is higher than 100,000 [1]. By employing high speed machines in direct drive systems, the mechanical transmission component can be eliminated in the drive system leading to the advantages of high efficiency and high reliability, while reducing the weight, noise and maintenance cost of the whole system [10]. Based on the well-known electrical machine design principle, the relationship between machine torque and size are in reverse proportion if the machine constant output power is maintained; namely, the machine size decreases as its operational speed increases: hence, high speed machines are normally small in size with high power density. With the low moment of inertia, the high speed machine dynamic response can also be increased. Therefore, high speed machines are especially suitable for automotive applications where space and energy savings are in high demand [11]; with the rapid growth in industrial applications requiring high speed machines in recent years, it can be expected that research on high speed machine design will remain at the cutting-edge of electrical engineering.

High speed machine design is always recognised as a challenging task due to the tight interaction between the electromagnetic, mechanical and thermal aspects [10] [12] of the machine, while machine electromagnetic performance is also constrained by the applied material capability. The high rotating speed of rotors also brings several challenges that need to be addressed. In order to obtain a suitable high speed machine scheme, a subtle design compromise needs to be achieved between the different machine multi-physical fields [13]. Some issues, which can be neglected in conventional speed machines, inversely, have critical impacts on high speed machine performance. With increasing machine speed, the alternating frequency of the rotating magnetic field in the machine core is also significantly raised and can reach the level of hundreds of Hz (sometimes even up to one thousand Hz). Such high frequencies can remarkably influence the machine magnetic material characteristics and power losses distribution. Though the merit of high power density per volume can be obtained, the power loss per volume is also significantly increased in high speed machines. Moreover, frictional loss, which is due to the reaction between the high speed rotating rotor and air fluid, is also significantly increased. Therefore, it is critical to precisely estimate high speed machine power losses, as these losses cause machine temperature rise. Overheating can noticeably deteriorate machine output performance or even lead to damage to machine components.

In order to keep high speed machines operating at a steady state, machine working temperature should be controlled within a reasonable range and steps taken to avoid the overheating problem. High speed machines normally have a small size compared to conventional machines at the same power rate. Therefore, high speed machine thermal issues become fundamentally important due to the limited heat dissipation area arising from the compact machine structure. Thus, it is necessary to consider machine temperature performance by carrying out extensive and reliable thermal analysis as part of the machine design process [12] [14]. As high speed machines can be depicted as small size with high power loss per volume, a cooling system that is integrated into the machine becomes an effective method of dissipating the heat generated by machine power losses. An effective cooling system is helpful for limiting machine temperature rise and protecting machine components from over-heating. In addition, extra attention should be given to high speed machine (especially high speed permanent magnet machine) rotor temperature distribution. Rotor cooling is normally regarded as more difficult than stator cooling as it can only be performed via the air gap; hence, the over-heating problem is found to be more prone to occur with the high speed machine rotor component.

Mechanical issues of high speed machines are not of secondary importance with respect to the electrical and thermal ones in machine design. Rotor strength and dynamics are of particular concern in high speed machine mechanical research. The rotor not only has to endure the large centrifugal force induced by high speed rotation, but also the thermal stress induced by the increased operational temperature. The objective of rotor strength analysis is to ensure that the rotor mechanical integrity is maintained when the machine is in high speed operation, which can be achieved by rotor stress analysis and verification of the safety factor. The safety factor is defined as the ratio of the yield strength to the maximum stress in the lamination [15]. The aim of the safety factor in rotor strength analysis is to leave a sufficient margin between the rotor operational stress and rotor material maximum permissible stress. As for the rotor shape for high speed machines, it is always designed to be slender; namely, long in axial length and short in the outer diameter. The reason for this [10] is that rotor external diameter must be made as small as possible to reduce the centrifugal force. (as the centrifugal force is proportional to the square of rotor rotational speed); consequently the rotor axial length has to be

increased to develop the specific torque. With the above design principle, the rotor can also benefit from air frictional loss reduction, as the air frictional loss is proportional to the rotor axial length and the fourth power of rotor external diameter [16]. However, there is limited space to increase machine rotor length based on the reason that rotor dynamic performance is closely dependent on rotor parameters. Vibration, which is due to resonance and unbalance forces, is prone to occur in rotors in high speed applications, while mechanical failures (such as rotor distortion) may occur in extreme cases when the rotor is designed with unreasonable rotor structure or dimensions. Therefore, in order to prevent triggering of any mechanical resonance effects, rotor dynamic analysis should be carried out to identify the critical speeds, which the machine needs to avoid during operation. As for the cases of some super high speed machines which can operate at supercritical speeds, the machine critical speeds must be passed through as quickly as possible to avoid any external mechanical perturbation or interference [10]. Reasonably designed high speed machine rotors can effectively decrease the possibilities of excessive acoustic noise, bearing damage and other mechanical failures. Rotor bearings also present practical challenges in high speed machine manufacture and application. Conventional bearings for medium and low speed machines cannot satisfy the requirement for high speed machines, due to the large centrifugal force and rotor friction effects acting on high speed rotors. The bearings for high speed machine application should be available to offer higher performances in terms of the factors such as maximum permissible rotational speed, working temperature, stiffness, precision and noise [13]. In the literature, it is found that ball bearings [17], air bearings [18] and magnetic bearings [19] are the choices available for high speed machines, with practical circumstances on a case-by-case basis dictating the optimal choice.

From the introduction above, we can draw the conclusion that high speed machines are regarded as a desirable and promising machine type bringing advantages such as high power density, high efficiency, small size and compact structure. High speed machines are also being widely adopted in industrial applications in recent years. The necessity for further research on high speed machines has also been revealed and illustrated. High speed machine research is a process relevant to machine coupling and multi-physical fields' research, relating to electromagnetic, mechanical and thermal topics. The major challenges for high speed machines can be summarised as

follows: electromagnetic losses due to the high frequency power supply and mechanical losses due to the rotor in high speed operation; machine temperature field analysis with an effective cooling system desired; high speed rotor strength, rotor dynamic analysis, reasonable rotor bearing selection and so on. Therefore, design of high speed machines remains a priority area for research, with particular consideration given to electromagnetic, thermal and mechanical aspects of machines in high speed operation.

Based on the introduction above, this thesis focuses on the design and multi-physical research for a 150 kW, 17,000 rpm high speed permanent magnet machine (HSPMM) for compressor application. It comprises of electromagnetic, thermal and mechanical analysis for the machine. Design considerations and factors affecting HSPMM performance are studied and discussed in detail. Machine power losses, including iron losses, rotor eddy current losses and mechanical air frictional losses are investigated and studied. Machine iron losses are estimated with practical flux density waveforms in the iron core considered to achieve high precision. Factors effecting machine rotor eddy current losses are discussed with PM bevelling proposed to reduce such losses in the machine; CFD modelling is developed for the HSPMM to investigate the machine temperature field. Rotor strength analysis is performed for the HSPMM rotor structure with pole filler by FEM. As a rotor sleeve is a necessity for surface-mounted rotors in high speed applications, the impacts of rotor material, temperature, sleeve thickness and interference on rotor stress are researched. Rotor cortical speeds are predicted by FEM to ensure machine is not operating at these speeds.

1.2 Main contributions

The contributions of this thesis can be summarized and listed as below:

- The design process for high speed permanent magnet machine (HSPMM) is studied, with a research on machine configurations and materials presented. Machine structures are investigated and compared with respect of machine performances such as cogging torque, back EMF, on-load torque, losses and air gap flux density.

- Machine iron loss calculation method with consideration of magnetic field variation is proposed. Rotor eddy current loss is investigated with respect of machine

configurations and parameters, including sleeve conductivity and thickness; composite rotor structure; air gap length and stator slotting width. Rotor PM bevelling is also proposed to reduce HSPMM rotor eddy current loss while maintaining machine output torque. HSPMM air frictional loss is also studied by fluid field analysis.

• HSPMM temperature is investigated by CFD analysis. Factors effecting HSPMM thermal performance are further discussed, including cooling air velocity, rotor eddy current loss and sleeve thermal conductivity.

• A prototype HSPMM is developed and tested, with machine analysis results validated by experiments.

• HSPMM rotor mechanical performances are researched by FEM. Machine rotor stress is further discussed with pole filler material selection and temperature effecting. Rotor sleeve thickness and interference are integrally studied in machine rotor strength analysis. HSPMM rotor dynamics analysis is also performed for machine critical speeds calculation.

1.3 Outline

The thesis is organized as follows:

Chapter 2 provides an extensive review of the previous work and current state-of-the-art in electrical machine design for high applications. Induction machines, switched reluctance machines and permanent magnet machines, the electrical machine types normally selected for high speed operation, are introduced. Then the principles and calculation development for high speed machine power losses are presented; LPTN, FEM and CFD methods are studied and compared in high speed machine temperature prediction; issues impacting rotors in high speed rotation, such as shaft bearing system selection, rotor strength and dynamics are also further studied and summarized.

Chapter 3 presents the basic design principle and the factors influencing HSPMM performances. Firstly, the HSPMM design process is proposed and illustrated with multi-physical fields coupling effects considered; then machine materials, as well as design configurations are further discussed to find a reasonable machine design

scheme. HSPMM performance parameters, including cogging torque, back-EMF, loses, on-load torque performances and air gap flux density distribution, are also extensively studied for different operational conditions as machine design parameters vary.

Chapter 4 investigates HSPMM power losses comprehensively. Machine flux density variation characteristics are studied by FEM analysis at first; then HSPMM iron loss is estimated by an improved method. This method is based on the practical flux density waveform in the iron core, while harmonics and rotational magnetic field effects are also considered for high precision in HSPMM iron loss estimation. HSPMM air gap flux density distribution is analytically calculated with the stator slotting effect considered; good agreement is achieved between analytical and FEM analysis results.

HSPMM rotor eddy current loss is investigated using time-stepping FEM, and the impacts of different machine configurations and parameters assessed. The effects from the rotor sleeve are discussed in depth, while eddy current loss variation due to conductivity is also further explained and presented; a rotor composite structure is studied with different rotor sleeve materials; and rotor eddy current loss variation due to machine parameters, including air gap length and stator slotting width, are further researched. A PM bevelling method is also proposed as a means of reducing rotor eddy current loss while maintaining machine output torque.

HSPMM air frictional loss is studied by CFD fluid analysis, while a 3D air frictional loss calculation model is established based on the machine structure and rotor cooling method; rotor speed, roughness and cooling air speed effects on machine air frictional loss are also studied.

Chapter 5 studies the HSPMM temperature field using CFD. At first, machine cooling air fluid flow regulation is studied based on thermal and fluid flow principles. Then a HSPMM 3D fluid-temperature coupling calculation model is set up for machine temperature distribution estimation with the obtained power losses and boundary conditions. Factors effecting machine thermal performance are also researched and discussed in this study, including cooling air velocity, rotor eddy current loss and sleeve thermal conductivity. A HSPMM is prototyped with

experimental tests carried out on it, enabling the machine temperature results by CFD analysis to be verified experimentally.

Chapter 6 illustrates the mechanical research for HSPMMs. At first, rotor strength is discussed using a thick-walled cylinder model to represent rotor elasticity, and the results by FEM are verified against analytical method results. HSPMM rotor stress distributions are investigated with sleeve material and operational temperature considered. In order to reduce sleeve stress, three pole filler materials are compared with their thermal expansion effects on permanent magnet stress also discussed; then the variation in the stresses on HSPMM rotor components due to temperature are further studied. Rotor sleeve thickness and interference are also integrally researched for machine rotor strength analysis. HSPMM rotor dynamic analysis is performed with a FEM 3D dynamic rotor model for critical speeds calculation.

Chapter 7 summarizes the outcomes of the work in this thesis and possible future directions for HSPMM research.

1.4 Publications

Papers based on the thesis

Journal (relating to Chapter 4 and Chapter 5):

1. Yue Zhang, Seán McLoone and Wenping Cao, “Electromagnetic loss modeling and demagnetization analysis for high speed permanent magnet machine”, IEEE Transactions on Magnetics, Vol.54, No. 3, #8200405. Mar. 2018.

2. Yue Zhang, Seán McLoone, Wenping Cao, Fengyi Qiu and Chris Gerada, “Power loss and thermal analysis of a MW high speed permanent magnet synchronous machine”, IEEE Transactions on Energy Conversion, Vol. 32, No.4, pp. 1468-1478. Dec. 2017.

Conference (relating to Chapter 3 and Chapter4):

3. Yue Zhang, Seán McLoone and Wenping Cao, “High speed permanent magnet motor design and power loss analysis”, 2017 IEEE Transportation Electrification Conference and Expo, Asia-Pacific (ITEC-AP).

4. Y. Zhang, S. McLoone and W. Cao, "Power Loss and Demagnetization Research for High Speed Permanent Magnet Electrical Machine", 2017 IEEE International Magnetics Conference (Intermag).

Further Contributed papers

Journal:

5. Yue Zhang, Wenping Cao, Seán McLoone and John Morrow, "Design and flux-weakening control of an interior permanent magnet synchronous motor for electric vehicles", IEEE Transactions on Applied Superconductivity, Vol. 26, No. 7, #0606906. Oct. 2016.

6. Yue Zhang, Wenping Cao and John Morrow, "Design of an interior permanent magnet synchronous motor (PMSM) for EV traction", Transactions of China Electrotechnical Society, Vol.30, No.14, pp. 108-115. Jul. 2015.

Conference

7. Yue Zhang, Wenping Cao and John Morrow, "Interior permanent magnet motor parameter and torque ripple analysis for EV traction", 2015 IEEE International Conference on Applied Superconductivity and Electromagnetic Device (ASEMD).

8. Yue Zhang, Wenping Cao and John Morrow, "Dual three phase induction motor power loss analysis with its modeling and simulation of vector-controlled system", 2015 IEEE International Conference on CYBER Technology Automation, Control and Intelligent Systems (IEEE CYBER).

Chapter 2
Development of high speed electrical machines

2.1 Machine types for high speed applications

With their remarkable performance and extensive industrial application prospects, the development of high speed machines has found rapid growth in recent years. The advantages of system weight reduction and reliability improvement brought by application to direct drives has fuelled research into high speed machine technology. In industrial applications, various machine types have been considered as suitable candidates meeting the requirements for high speed operation [20], with induction machines, switched reluctance machines, claw pole machines and permanent magnet machines successfully employed for high speed operation. In this chapter, the development of several kinds of high speed machine is introduced, and the main technology challenges for high speed machines are also illustrated in detail.

2.1.1 Induction machine

The induction machine has a simple structure and is relatively insensitive to temperature variation, making it a widely used machine type for high speed applications. Many high speed induction machines have been introduced in the literature. A 300 kW, 60,000 rpm solid rotor induction machine for a next generation air compressor system has been investigated by Sundyne Corporation. This induction machine provides good performance and can be characterized as small volume, high power density and high tip speed [21]. The air compressor system equipped with a high speed induction machine is shown in Fig. 2.1 and the machine rotor is given in Fig.2.2.

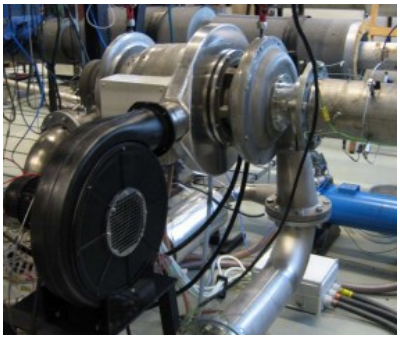

Fig.2.1. Air compressor system equipped with high speed induction machine (300 kW 60,000 rpm) [21].

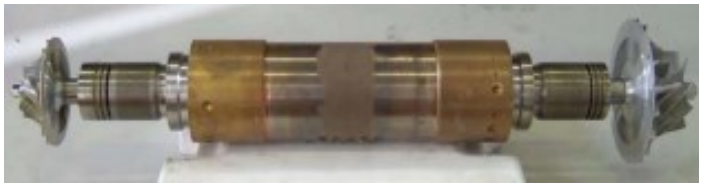

Fig.2.2. 300 kW 60,000 rpm copper coated solid rotor induction machine [21].

The ABB Company designed and invented a 20,000 rpm induction motor with its power up to 15 MW for a gas compression application [22]. Electrical vehicle propulsion powered by a 40 kW, 40,500 rpm induction machine is proposed with its performance displayed and compared in [23]. A 10 kW, 80,000 rpm induction machine is modelled, prototyped and tested under several operational conditions including no load, locked rotor and on load in [24].

In order to achieve the desirable performance in both electromagnetic and

mechanical aspects, a series of design methods have been proposed for high speed induction machines in the literature. A novel design of solid rotor with radial rotor surface grooves is proposed for a 4 pole, 24,000 rpm induction motor as described in [25]. It is proven that by radial grooving the rotor outer surface and cutting the path of high frequency rotor harmonic currents, machine rotor eddy current loss can be considerably reduced accordingly. New materials have also found utilization in high speed induction machines. For example, application of an amorphous material for the stator core can lead to a significant reduction in stator core losses when compared to a conventional design, however, punching the material becomes difficult in machine manufacture [26]. A squirrel cage embedded in closed slots has been put forward for high machine rotor speeds reaching up to 300 m/s using this arrangement [27]. An advanced end-ring rotor topology is introduced and applied for a 2 MW 15,000 rpm induction machine rotor with the end-ring and machine rotor presented in Fig. 2. 3 (a) and (b), respectively. The structure of non-uniform cross section, hoop stress relief and an integrated joint boss on the rotor can reduce the stress concentration problem, allowing the machine rotor to run over a large speed and temperature range [1] [28].

(a) End-ring to bar solder joints (b) Rotor

Fig.2.3. 2 MW 15,000 rpm induction machine [28].

High speed induction machine rotor structure design is a critical technical topic discussed in several papers. Compared to a solid rotor, laminated rotors can dramatically decrease rotor loss to achieve high efficiency; while the solid rotor still presents its mechanical advantages in higher speed operation. Three kinds of high speed induction motor solid rotor topologies (shown in Fig.2.4) are compared, while it is reported in [29] that the coated solid rotor has higher efficiency but lower power factor when compared with the smooth solid rotor structure, as its equivalent air gap is larger than the other types; the smooth solid rotor has the most robust structure but

relatively lower conductivity for induced current [1] [30].

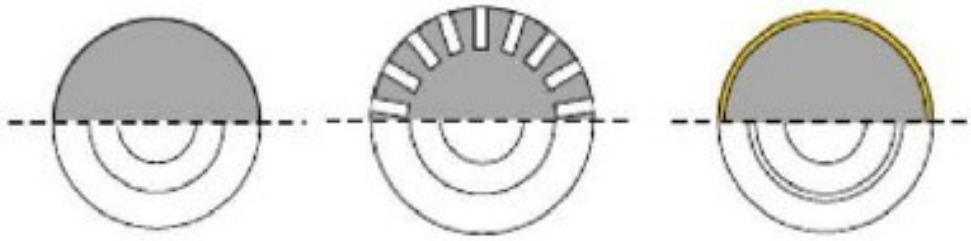

(a) Smooth solid rotor (b) Solid rotor with slitting (c) Coated solid rotor

Fig.2.4. Solid rotor topologies [29].

Five types of squirrel cage rotor topologies, as shown in Fig.2.5, are presented and discussed in [31] to find out the most suitable rotor format for a 4 MW high speed induction machine by comparison of mechanical constraints, frictional loss and electromagnetic performance.

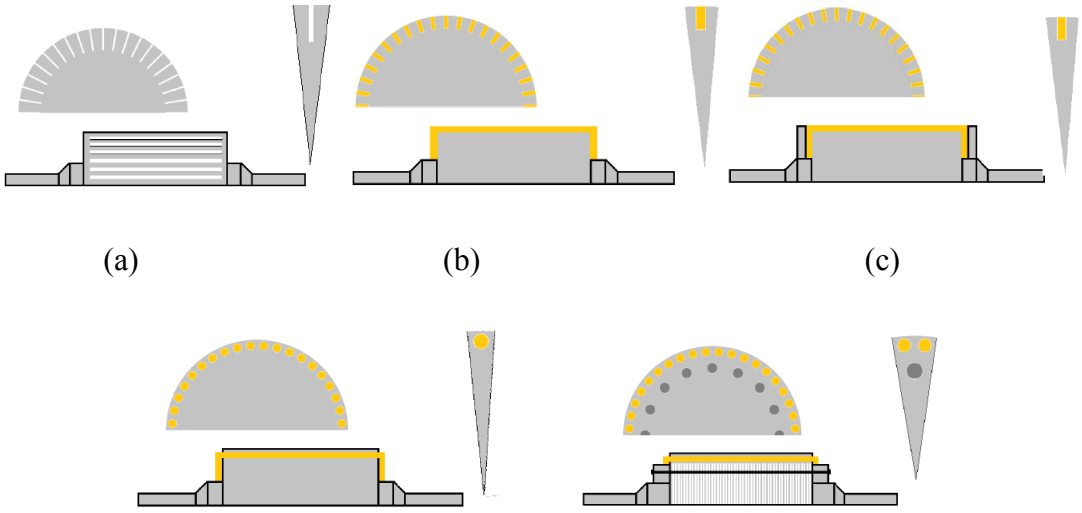

Fig.2.5. Rotor topologies for high speed induction machine [31]. (a) Solid rotor slitted radially (b) Solid rotor with rectangular open slots with brazed squirrel cage (c) Solid rotor with embedded squirrel cage by isostatic pressure (d) Solid rotor with round embedded copper bars inserted in a solid rotor core with drill holes (e) Laminated rotor with embedded copper bars with copper end plates and end shafts assembled by tie rods

It is reported that a rotor of type (a) can offer the most desirable mechanical performance and the lowest frictional losses, but its rotor loss is higher leading to unsatisfactory efficiency; higher rotor conductivity can be achieved by (b), but its power factor is relatively low; rotors of type (c) have the same electromagnetic performance as (b) but have higher manufacturing cost than (b); (d) type rotors suffer from low power factor, high rotor loss; while rotors of type (e) act as an elaborated solution, which brings both mechanical and electromagnetic advantages with relatively low manufacturing cost. The optimization of high speed induction machine rotor bar shape is further revealed in [12]. It can be proven that by replacing the circular rotor bar (Fig.2.6 (a)) by the drop rotor bar (Fig.2.6. (b)), machine power density can be boosted by allowing more current density, albeit the lamination stress level is also increased for machines in high speed operation.

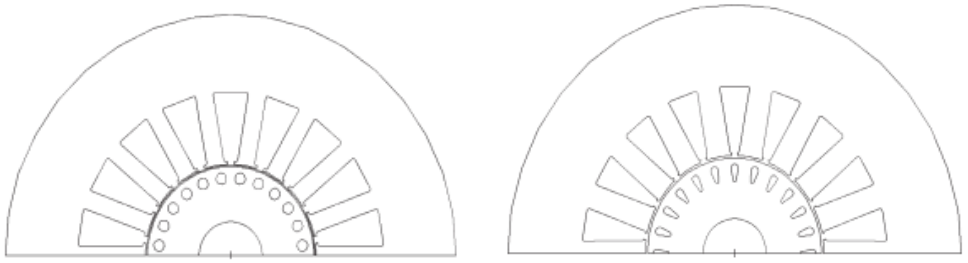

(a) Circular rotor bar (b) Drop shape bar

Fig.2.6. High speed induction machine rotor bar optimization [12].

2.1.2 Switched reluctance machine

Switched reluctance machines (SRMs) have also been used for high speed applications, due to their simple robust structure and low manufacturing cost. However, SRM applications are also constrained by factors such as torque ripple, excessive vibration and acoustic noise.

A SRM is a type of machine that is characterised by a double salient single excitation structure, with simple concentrated windings (each coil becomes one pole) with no windings or permanent magnet material employed on the rotor side. These features make it possible for SRMs to operate at an ultra-high speed. Most SRMs operate at kW power levels and utilize one of several characteristic stator/ rotor structures, such as three phase 6/4, 12/8 or four phase 8/6 topologies. A 30 kW 14,000 rpm high

speed SRM with conical magnetic bearings for aircraft application is designed and studied in [32]. A machine system with conical magnetic bearings configuration is illustrated in Fig.2.7 (a), while the SRM prototype is displayed in Fig.2.7 (b).

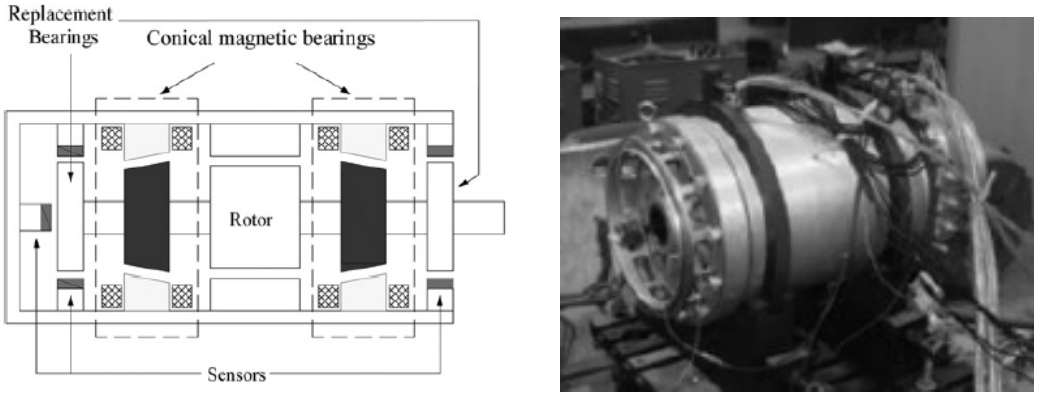

(a) Conical magnetic bearing system (b) Prototype

Fig. 2.7. 30 kW 14,000 rpm SRM with conical magnetic bearing [32].

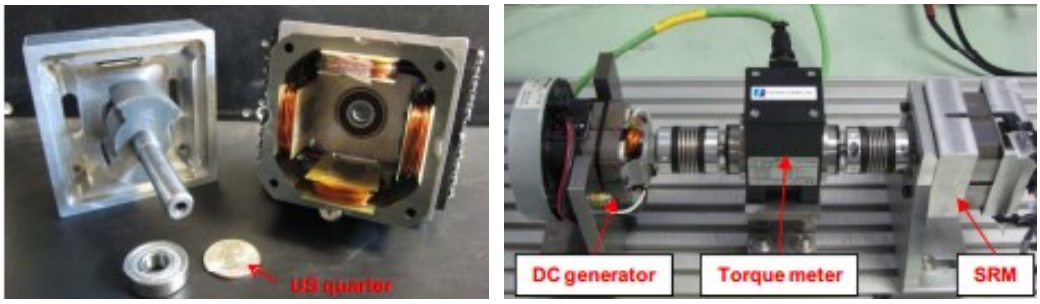

(a) Two phase SRM prototype (b) Experiment dynamometer setup

Fig. 2.8. 48,000 rpm high speed SRM [33].

Fig. 2.8 shows details of a low manufacturing cost, 48,000 rpm, two-phase high speed SRM designed and experimentally verified with machine parameters effects discussed in [33]. Optimization of the rotor structure for high speed SRMs is an effective method to improve machine performance. A 1 kW ultra-high speed SRM (maximum speed can reach up to 200,000 rpm) using a new rotor structure and composite material is reported in [34]. In order to improve the start-up performance of a 1 kW 130,000 rpm 3-phase high speed SRM, a novel rotor is proposed by employing a stepped shape topology in [35], while Fig.2.9 (a) shows the machine topology and Fig. 10 (b) shows the prototype machine. Stator tooth width W_{sp}, rotor

tooth width W_{rp} and rotor step width W_{rs} are also optimized to improve machine start-up performance.

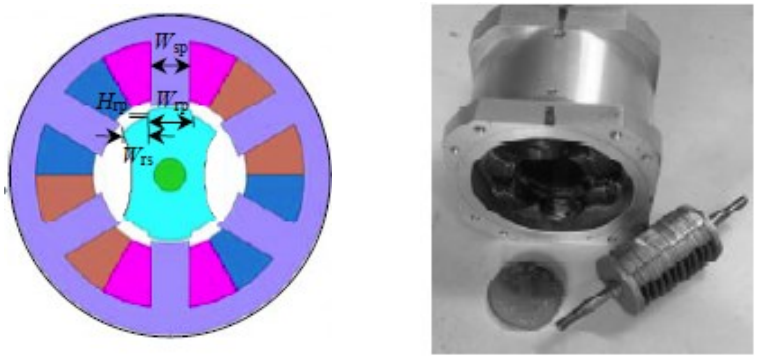

(a) Stepped rotor (b) Prototype

Fig. 2.9. 1 kW 130,000 rpm SRM [35].

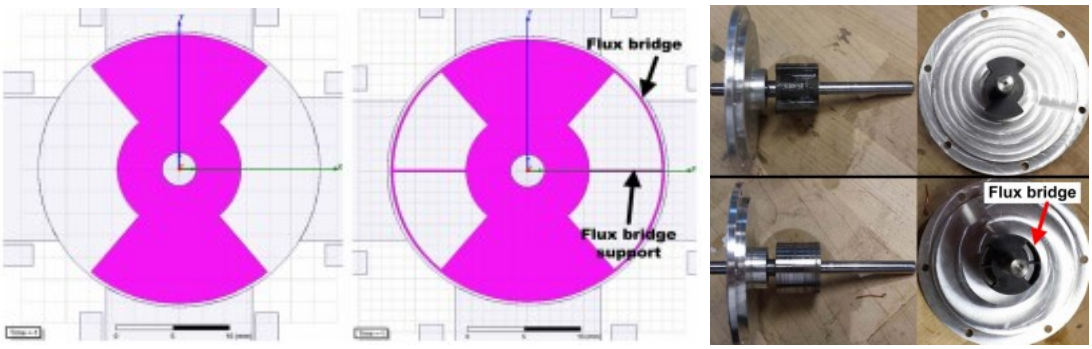

(a) Cross-sectional view (b) prototype

Fig. 2.10. SRM rotor design with and without flux bridge [36].

The shape of SRM rotors is normally with the structure of salient poles. This may lead to notable windage loss when compared to conventional cylindrical shaped rotors for machines in high speed operation. Hence, it is necessary to elaborate SRM rotor topology for windage loss reduction. It is advisable to add a flux bridge for rotor lamination, which is already implemented on a 50,000 rpm high speed SRM as shown in Fig.2.10. Moreover, machine performance effects by variation in flux bridge dimensions are also further discussed in [36]. The main benefit of using flux bridge on the rotor is to reduce the windage loss. It is noted that that careful mechanical design is required. The flux bridge thickness cannot be too small given the limitations from the mechanical considerations and the manufacturing capability.

Another method for high speed SRM windage loss minimization is introduced in [37], namely a structure with a rotor rib. From the driving test results for a 15,000 rpm SRM, it is found that distinct windage loss reduction effects can be obtained by using the rotor rib component, while also maintaining the advantages of the conventional SRM rotor structure.

Several papers have discussed sensorless control technology for high speed SRMs, as the installed encoders or resolvers for rotor position detection obviously increase machine cost and decrease the SRM system reliability. Sensorless control strategies for the SRM drive can be categorised as follows [38]: open-loop methods, signal injection methods, passive waveform monitoring and computationally intensive methods. An improved method is proposed in [39] for high speed SRMs to overcome the low frequency disadvantage resulting from the traditional SRM control strategy. It provides a better and simple scheme to achieve machine ultra-high speed operation. The current gradient sensorless (CGS) scheme for high speed SRMs has been experimentally achieved on a 1.6 kW, 100,000 rpm 4/2 SRM. This method also has the potential to be realized on low-cost domestic products. However, it becomes necessary to map the current peak movement to obtain good drive control performance using the CGS method [40]. A novel speed control strategy for a high speed SRM drive, which only relies on DC-link voltage and current measurement without speed or position sensors utilized, is proposed with closed-loop simulation carried out to verify its stability in high speed operation in [41].

2.1.3 Permanent magnet machine

Permanent magnet machines are frequently employed in high speed applications due to their dominant advantages over other machine types. High speed Permanent magnet machines (HSPMMs) can deliver high efficiency, high power density, compact structure and high power factor. Basically, HSPMMs should employ brushless configurations with the help of power electronic converter devices, as the brush component constrains the brushed DC machine from being developed towards high speed application. HSPMMs normally adopt a high energy density permanent magnet material, such as NdFeB or SmCo with large coercive force H_c and residual flux density B_r, to provide magnetic field excitation. Moreover, the high speed permanent magnet machine has two operation models in general, as a brushless AC

machine (BLAC) which is powered with a sinusoidal waveform and a brushless DC machine (BLDC) which is powered with a square waveform. Compared to BLAC, BLDC has a less complex control system, but higher output torque ripple and power loss due to the abundant harmonic components existing in the winding current.

(a) 1.2 MW 23,000 rpm PM generator [42]. (b) 7 MW high speed PM generator [43].

Fig. 2.11. High speed permanent magnet machine product from (a) UK Turbopower System Inc. and (b) ABB Inc.

Permanent magnet machines have great potential for industrial applications and have become desirable solutions for high speed applications. Several commercial products have been launched on the market. UK TurboPower Systems Inc. [42] has invented a 1.2 MW, 23,000 rpm high speed permanent magnet generator system, which can operate at a net 96% efficiency. The generator is shown in Fig. 2.11 (a); ABB Inc [43] have introduced a 7 MW high speed permanent magnet machine product, as shown in Fig. 2.11 (b), which offers high efficiency and high reliability for turbines.

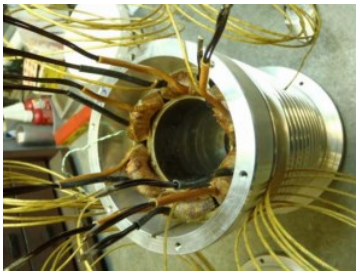

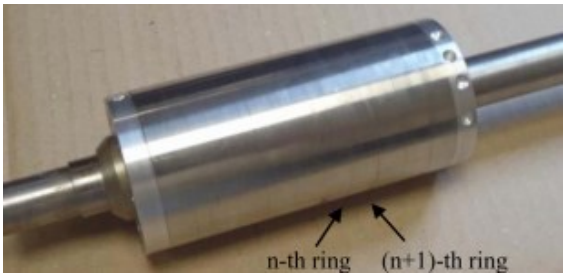

(a) Wound stator (b) Rotor assembly

Fig. 2.12. Photographs of high speed fault tolerant permanent magnet machine [45].

There is a wealth of literature published on HSPMMs addressing cutting-edge technology research and development. The University of Nottingham in the U.K. had

a particular focus on high speed machine research including permanent magnet machines for several years. In [44], D. Gerada and C. Gerada have discussed the design issues associated with an 84,000 rpm HSPMM that is required to operate in a high temperature environment. It is found that optimization for higher efficiency and material saving can be achieved by adjusting some critical machine design parameters, such as sleeve thickness, air gap length and split ratio. L. Papinoi, T.Raminosoa and C.Gerada [45] proposed a type of six slot-four pole HSPMM for fault tolerant drivetrains. They investigate and discuss the influence on rotor eddy current loss and average torque from machine parameters, including split ratio, tooth width and slot opening, using FEM analysis [45]. The introduced machine is also prototyped (as depicted in Fig. 2.12) with several experimental tests (Fig.2.13.) carried out to verify machine simulation results. H. Zhang, C. Gerada and D. Gerada [46], [47] also presented a 3 kW, 80,000 rpm concentrated-wound high speed permanent magnet generator with its stator tooth designed as a shoe shape. Both analytical and FEM methods are utilized to investigate the machine performance. In addition, the shoe shape coefficient (defined as the ratio of the stator tooth top pith length l_c to the pole pitch length l_p) is also proposed and optimized by genetic algorithm (GA) to promote better generator performance. The cross-section for the shoe shape teeth machine is shown in Fig. 2.14 (a), while the shoe shape coefficient is shown as 2.14 (b). It is also noted that the applications of the shoe shape teeth generator may be restricted due to the complicated manufacture processing required.

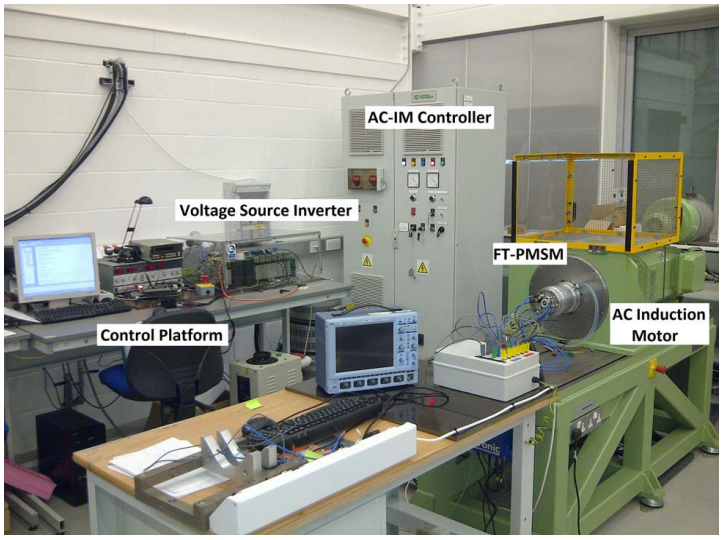

Fig. 2.13. Experimental test rig for a high speed fault tolerant permanent magnet machine [45].

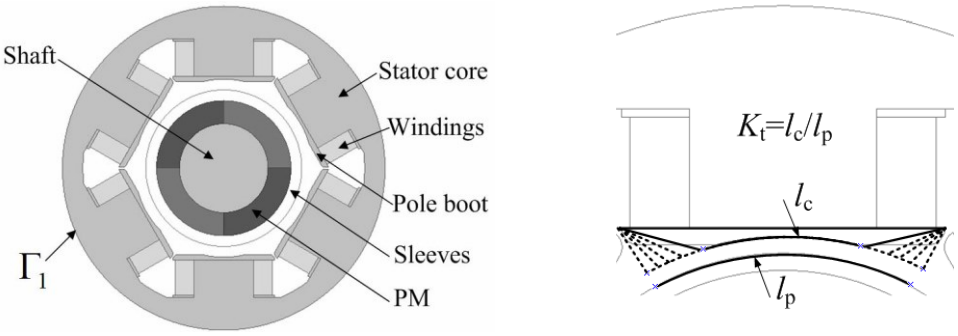

(a) High speed machine with shoe shape teeth (b) shoe shape coefficient

Fig. 2.14. 3 kW 80,000 rpm shoe shape high speed permanent magnet generator [46].

Nocolas and his colleagues from Laboratoire IREENA, France illustrated a design methodology for HSPMM design. A design methodology for a non-salient synchronous machine is revealed in [48], which allows estimation of machine size using parameters from effective torque. Besides general multi-physics methods, a new analytical approach to solving the surface-mounted HSPMM optimization issues (such as maximizing power-to-volume ratio) is further proposed in [49]. It is performed based on several machine mathematical analytical models, including electromagnetic power, power loss, mechanical loss, thermal constraint and mechanical constraints models. The effectiveness of the optimization method is verified by both FEM and experiment measurements.

C. Zwyssig et al. from the Swiss Federal Institute of Technology Zurich (ETH) reported their invitation of a 1 kW, 500,000 rpm HSPMM with drive control system [50]. The machine cross-section is shown in Fig. 2.15 (a) while the control hardware system is given in Fig.2.15 (b). A slotless stator configuration is utilized for this HSPMM to achieve high power density with less high frequency loss. The whole cylindrical permanent magnet is enclosed by a titanium sleeve and cup-shaped air-gap windings are placed between the rotor and the slotless iron core. It is noted that the winding eddy current loss for the machine with air gap windings could be high, particular for high speed applications. A similar machine structure for ultra-high speed operation can also be found in the study of a 100 W, 500,000 rpm permanent magnet machine for a mesoscale gas turbine application [51]. Besides the conventional losses such as copper, iron and eddy current losses, air frictional loss is also taken into considerations in the research for loss minimization using the Nelder-

Mead simplex method. It is proven that optimization of the magnet radius and stator core inner radius, the minimization of the rotor sleeve thickness and the utilization of an amorphous material for stator lamination, can significantly decrease the ultra-high speed permanent magnet machine power losses.

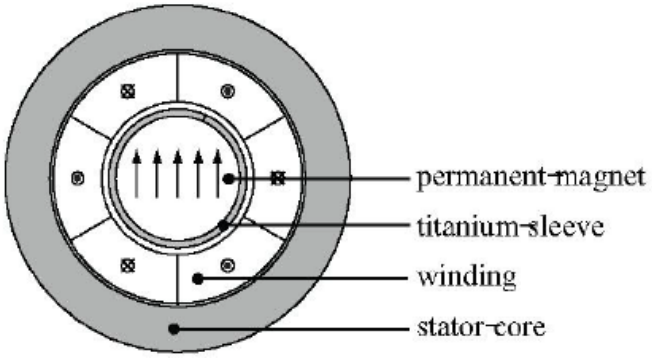

(a) 1 kW, 500,000 rpm PM machine

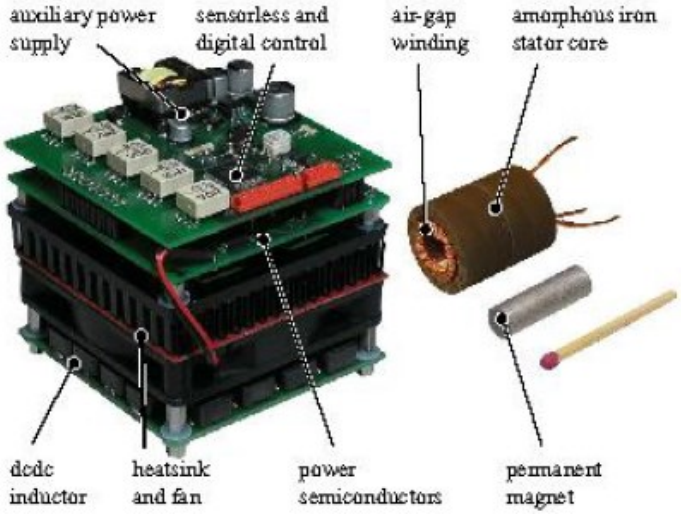

(b) Control hardware system

Fig.2.15. 1 kW, 500,000 rpm PM machine with control system [50].

Munteanu, Binder, and Schneider *et al* performed an investigation of a 40 kW, 40,000 rpm high speed surface-mounted bearingless permanent magnet machine. Machine no-load test performance is reported in [52] with the design procedure illustrated in more detail in [53]. From the analysis results, it is pointed out that rotor losses can be significantly reduced by PM segmentation and a rotor back-iron lamination; Schneider investigated the effect of pole pair number for bearingless

HSPMMs in [54]; Binder compared rotor structure (surface-mounted PM rotor and buried PM rotor, as shown Fig. 2.16) effects on a 40 kW, 40,000 rpm HSPMM from a mechanical prospective [55]. It is found that a surface-mounted PM rotor fixed by carbon-fibre bandage is a better choice for machines in high speed operation, as such a rotor configuration has much higher mechanical strength and allows a higher maximum operational speed.

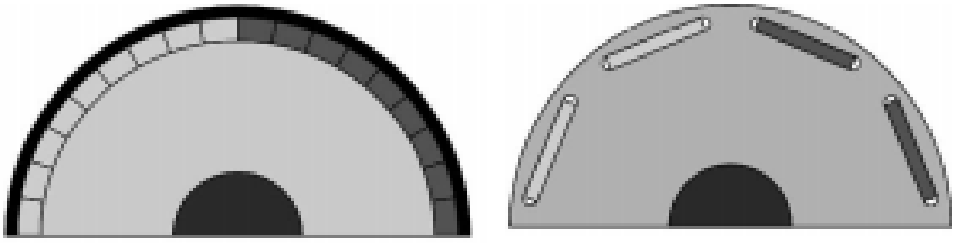

(a) Surface-mounted magnet rotor (b) Buried magnet rotor

Fig.2.16. 40 kW, 40,000 rpm PM machine with control system [55].

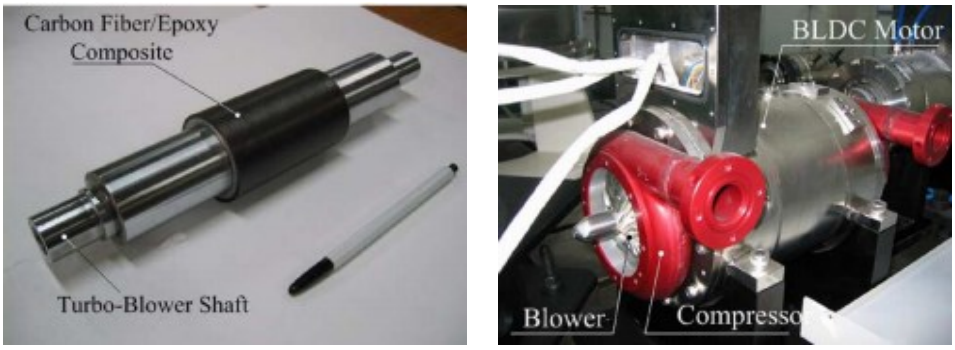

(a) Permanent magnet rotor (b) Motor assembly

Fig.2.17. 50 kW, 70,000 rpm high speed BLDC [56].

Seok-Jang and Han-Wook Cho *et al* focused on the design of a series of HSPMMs. A 50 kW, 70,000 rpm high speed BLDC for centrifugal turbo-compressor application (shown as Fig.2.17) is reported in [56]. Machine performances, including air gap flux density and back-EMF, are predicted by an analytical method, and then compared with FEM results. Satisfactory agreement can be found between the results from the analytical method and FEM analysis. Moreover, machine electromagnetic and mechanical loss characteristics are also provided. The analytical solution to predict

magnetic field distribution and machine output characteristics for a 2 kW high speed permanent magnet generator is also proposed in [57].

F. Luise *et al* discussed design issues for a 640 kW, 10,000 rpm Halbach- array PM slotless machine with active magnetic bearings, as shown in Fig.2.18. Several preliminary basic considerations for the compromise between machine performance and machine production cost are reported. The study includes machine shaft design, motor type choice, as well as stator, rotor design, power converter design and cooling system design. Moreover, machine optimization performed by genetic algorithms has also been reported to search for the best trade-off solution for machine efficiency-cost [58]. The manufacture and testing of for the Halbach-array permanent magnet machine are further illustrated in [59]. It is proven from the prototype testing results that this machine efficiency can be up to 98%. Bianchi *et al* further investigated permanent magnet brushless machines in high speed operation (20,000-40,000 rpm). Factors including PM materials, as well as slotted and slotless machine configurations (as in Fig. 2.19), are considered in machine design [60]. It has been reported that the slotless configuration with NdFeB permanent magnet material proved to be a good solution: it realized good performance both in terms of specific power and torque overload capability. HSPMM design is fully analysed in [61], indicating that the slotless PM rotor configuration is less sensitive to PM demagnetization and is also characterized by lower rotor losses.

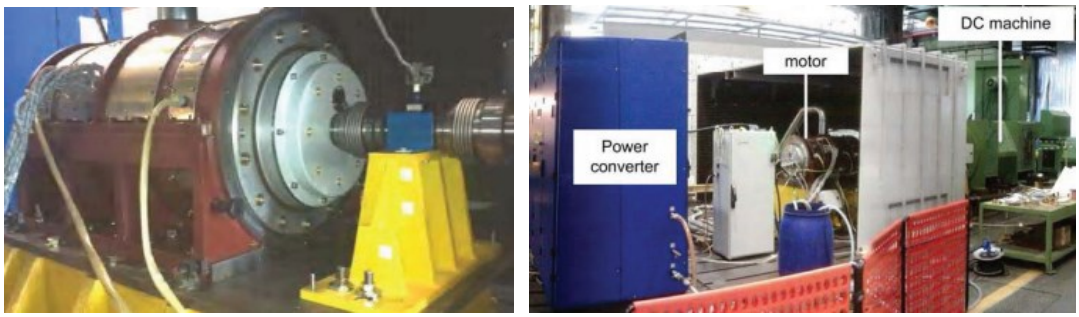

(a) Motor prototype mounted on the base (b) Test bench

Fig.2.18. 640 kW, 10,000 rpm Halbach- array PM slotless machine [59].

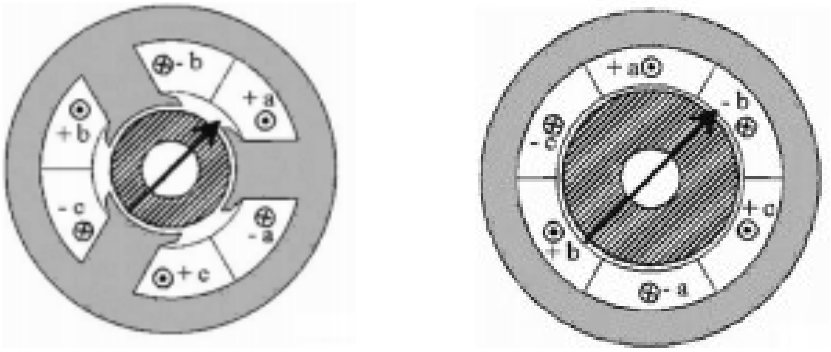

(a) Slotted PM motor configuration (b) Slotless PM motor configuration

Fig. 2.19. Slotted and slotless configurations [60].

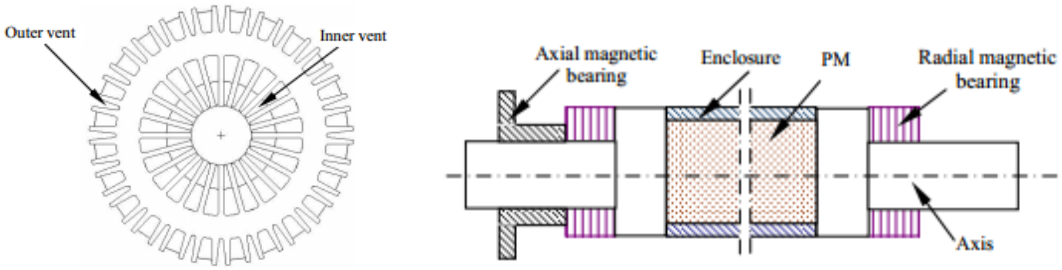

(a) Stator structure (b) Rotor structure

(c) Photo of prototype

Fig. 2.20. High speed PM generator for distributed micro-turbines [62].

Wang. *et al* have carried out an overall investigation for a novel 75 kW, 60,000 rpm high speed permanent magnet generator for distributed micro-turbines. The stator structure is as shown in Fig. 2.20 (a). Its rotor structure is shown in Fig.2.20 (b), and the prototype of the high speed generator is shown in Fig.2.20 (c) [62]. The stator has series-wound connected windings around the stator circumferential direction. Ring type winding is utilized for the machine to reduce the axial length of winding end part greatly, which is important to increase the rigidity of the high speed rotor system.

Therefore, the winding axial-end length of a conventional machine structure can be transferred to the stator yoke side by the novel machine structure. Moreover, the machine also benefits by an increase in the heat- radiation area. Hence, the stator surface and the windings can both be cooled by the airflow in the axial-direction. The machine rotor is magnetically suspended by magnetic bearings with a non-magnetic alloy enclosure used to protect the PM from mechanical damage when the machine is operating at high speed. Machine PM material type is N30UH. Machine multi-physical fields have been analysed to investigate machine performance. The iron core loss calculation model is implemented and verified by experimental measurement [63]. The relationship between power losses (iron loss and eddy current loss) and rotor speed is developed in [64]. Both the heat circuit method and fluid-solid coupled method are applied to estimate machine temperature rise. Compared with the experimental test results, it is found that the fluid-solid method better approximates the experimental measured results; while the equivalent heat circuit provides a simpler approach to machine temperature estimation [65]. Mechanical stiffness and rotor dynamics for the high speed machine are also researched and verified in [66] and [67]; machine anti-demagnetization performance is further discussed in [68]. It is found that the rotor high strength non-magnetic steel enclosure not only protects the PM from mechanical damage, but also reduces PM eddy current loss, which is helpful in reducing PM temperature. In addition, effective cooling is also necessary to ensure the machine operates with high reliability and that the rotor PM is protected from demagnetization by overheating when the machine is in high speed operation. For the researched high speed PM machine structure in 2.20 (a), the stator core has both inner and outer vents for cooling. Through the axial ventilation in the inner and outer vents, the temperature of the PM rotor can be reduced. Therefore, adding inner cooling vents inside the stator slots is also a simple and effective approach to limit machine rotor temperature rise.

2.2 Power loss analysis for HSPMMs

Due to the machine operating at high electromagnetic frequency and high mechanical rotor rotation, HSPMM power loss density is significantly higher than conventional speed machines for the same power rating. Power loss is a primary and fundamental consideration for HSPMM design, as machine temperature rise is closely dependent on its power losses. The main HSPMM power losses can be categorised as follows:

1. Stator side:

(a) Stator iron loss: high frequency variation magnetic fields in the stator iron core result in considerable iron loss, as machine iron loss is closely related to the magnetic flux density and frequency in the iron core. In addition, iron loss is a considerable proportion of the total power losses in a HSPMM.

(b) Stator copper loss: As currents flow through the machine winding strands, then copper loss is generated due to the resistance of the winding strands. Moreover, with the high frequency varying current acting in the HSPMM windings, HSPMM winding resistance is also increased due to skin and proximity effects.

2. Rotor side

(a) Rotor eddy current loss: harmonic components in the machine magnetic field, which rotate with an asynchronous rotational speed to the rotor generate eddy currents. Machine rotor eddy current loss can lead to an over-heating problem (especially for HSPMMs), which degrades machine performance and reliability. The overheating problem usually occurs on permanent magnet machine rotors due to their poor heat dissipation capability. Therefore, it is necessary to predict and investigate HSPMM rotor eddy current loss and to seek to optimize rotor topology in order to minimize eddy current loss.

(b) Air frictional loss: With the frictional effect between the air fluid and rotor surface, high speed machine air frictional loss can be significantly higher than in conventional speed machines. Hence, air frictional loss should also be taken into consideration in high speed machine design. Machine air frictional loss is dependent on rotor rotational speed, air fluid flow speed and rotor surface roughness.

2.2.1 Iron loss

Iron loss increases remarkably in HSPMMs and therefore needs to be estimated accurately [63][69][70]; hence, a considerable number of iron loss models have been proposed and investigated. It is pointed out in [71] that the field variation in a permanent magnet brushless machine is similar to the rotating field in induction machines; hence, iron loss estimation methods for permanent magnet brushless machines are also applicable to induction machines (IMs). It is worth mentioning that

the field variation of a switched reluctance machine (SRM) is different from the brushless permanent magnet machine, thus, a unique method needs to be employed to predict SRM iron loss.

The traditional and simple iron loss estimation method is as follows [71]:

$$P_{iron}=C_{fe}K_0(B/B_0)^2(f/f_0)^{1.3}G_{Fe} \tag{2.1}$$

where P_{iron} is iron loss; K_0 is the specific iron loss at the nominal flux density; B_0 is nominal flux density; f_0 is the nominal frequency; B and f are the actual flux density and actual frequency respectively; G_{fe} is iron core weight; C_{fe} is a calibration factor for the anisotropic characteristic of the material. Equation (2.1) is based on the assumption that iron loss is under the nominal iron loss frame with the actual flux density B and frequency f in proportion to the nominal flux density B_0 and nominal frequency f_0, respectively; then the iron loss can be rectified further with the calibration factor. Equation (2.1) has under gone long term verification and has already been widely utilized for conventional frequency machines due to its ease of implementation and fast solution features. However, the flux density in the machine iron core may get distorted, resulting in machine harmonic components that cannot be ignored; the machine iron core flux density characteristic is also subject to acute fluctuation. Hence, application of equation (2.1) in machine iron loss estimation has limited accuracy, especially for high speed machines.

The classical iron loss estimation model is the Bertotti iron loss separation model, which can be expressed as [72]:

$$P_{iron}=P_h+P_e+P_{\text{exc}}=K_h f B_m^{\alpha}+\frac{\sigma d^2}{12\rho T}\int_0^T\left(\frac{dB(t)}{dt}\right)^2 dt+\frac{\sqrt{\sigma G V_0 S}}{\rho T}\int_0^T\left|\frac{dB(t)}{dt}\right|^{1.5} dt \tag{2.2}$$

where P_{iron}: Iron loss P_h: Hysteresis loss

P_e: Eddy current loss P_{exc}: Excessive loss

σ : Iron core conductivity d: iron core thickness

ρ : Iron core density T: Magnetic flux density waveform period

S: Iron core area K_h, α : coefficients for hysteresis loss

G, V_0 : coefficients for iron core features.

In this model, the iron losses are divided into three terms, namely, hysteresis loss, eddy current loss and excessive loss with the associated iron loss coefficients obtained from experimental measurement [73]. Given the assumption that machine flux density varies sinusoidally, machine iron core loss then can be simplified further as [72][74]:

$$P_{iron} = P_h + P_e + P_a = K_h f B_m^{\alpha} + K_e f^2 B_m^2 + K_a f^{1.5} B_m^{1.5} \tag{2.3}$$

where K_h, K_e and K_a are the coefficients of hysteresis loss, eddy current loss and anomalous loss, respectively. The precision of machine iron loss estimation is affected by core flux density and iron core material coefficients. The standard Epstein frame and the single sheet tester (SST) measurement are conventional methods to evaluate iron core material power loss features, which have been widely accepted and utilized [75]; however, equation (2.3) is only effective for measuring the iron loss due to alternating magnetization. In fact, the flux magnetization dynamics in the machine iron core are normally complicated. There are two forms of magnetization in the machine iron core, namely, alternating magnetization and circular rotational magnetization. Moreover, iron core loss features are different due to the distinction in core magnetization type, as it has been revealed that the iron loss due to the rotational magnetic field is much larger than that of the alternating magnetic field counterpart [76].

Based on the Bertotti's iron loss model, several sophisticated and optimized iron loss models have been proposed to estimate electrical machine iron loss with greater accuracy. An iron loss estimation method which takes core rotational magnetization into consideration is proposed in [77], but extra 2-dimentional iron loss measurement equipment becomes a necessity to evaluate the iron core loss properties [72]. Ma Lei [78] also discussed iron core loss including rotational loss by assuming that the additional iron loss is proportional to the circular degree of the magnetic flux vector loci, which is expressed as the short-axis-to-long-axis ratio c. Hence, the evaluation of iron loss can be written as:

$$P_{fe-rot} = P_{hys-alt} + P_{eddy-alt} + P_{add-rot} \tag{2.4}$$

$$P_{add-rot} = \gamma c(P_{hys-alt} + P_{eddy-alt}) \tag{2.5}$$

$$c = \frac{L_{short}}{L_{long}} \tag{2.6}$$

$P_{hys-alt}$ is the hysteresis loss under alternating field, $P_{eddy-alt}$ is the eddy current loss under alternating field, $P_{add-rot}$ is the additional iron loss caused by the rotational field, L_{short} and L_{long} are the short axis and long axis of the flux vector trajectory ellipse respectively, γ is a constant that varies with flux density and core material. Based on Ma's iron loss model, Jang-Ho Seo *et al* [79][80][81] amended the hysteresis loss coefficient K_h and eddy current loss coefficient K_e further; as these two coefficients are not constants, but rather vary with frequency and flux density in the machine iron core; K_h and K_e vary as functions of the induction level and frequency which can be represented as fifth-order curve fitting polynomials. By introducing the adaptive loss coefficient, the proposed method can estimate iron losses considering the harmonics and rotating magnetic field. Its accuracy has been verified by prototype machine measurement. Another core loss model considering rotational iron loss for permanent magnet machines is developed and presented in [82]. This iron loss estimation is carried out by FEM (finite element method) analysis, and based on the magnetic flux density variation locus for each harmonic in each element of the iron core. Its effectiveness is verified by a test on a high speed permanent magnet machine prototype, which showed good agreement between the estimation results and experimentally measured results. The effect of uneven eddy current distribution due to the high frequency on the machine iron core is researched, and then the eddy current loss coefficient in the iron loss equation is further modified in [83] to give:

$$K_c(f) = K_c \frac{3}{D\sqrt{f}} \frac{\sinh(D\sqrt{f}) - \sin(D\sqrt{f})}{\cosh(D\sqrt{f}) - \cos(D\sqrt{f})} \tag{2.7}$$

where $D = d\sqrt{\pi\mu\sigma}$, f is the frequency and μ is the iron core permeability. The iron loss for interior permanent magnet machines, considering the carrier harmonics from PWM inverter, are investigated and presented in [84] and [85].

2.2.2 Copper loss

Copper loss in machine stator windings is closely dependent on machine current frequency, as winding resistance can be further increased by the skin and proximity effects due to the high frequency alternating current. With the high frequency currents flowing in the windings, current density become unevenly distributed over the copper strand cross-section and current is more prone to flow around the surface of the copper strand. For several copper strands approaching each other with current flowing through them, one strand is not only effected by its own magnetic field, but also by the magnetic field generated by the adjacent strands, which may also lead to uneven current density distribution in the copper strand. Both the skin effect and proximity effect can decrease the actual crossing area that currents flow through and lead to an increase in machine winding resistance and power loss.

The eddy current copper loss in the stator slot can be analytically approximately as [86]:

$$P = \frac{\pi \mu_0^2 \omega^2 d^4 n^2 I^2 y^2 l}{128 \rho_c b^2 h^2} \tag{2.8}$$

where d is the wire diameter, l is the wire length, ρ_c is the copper resistivity, b and h are the stator slot parameters, y is the wire position and ω is the radian frequency of flux density. It can be seen that the winding eddy loss is not only related to the properties of the wire, but is also affected by the wire position and stator slot geometry. Considering machine copper loss with skin effect and proximity effects is more complicated, and is difficult to express as a simple analytical equation.

Therefore, FEM becomes an effective and widely accepted method for winding copper loss research, which includes skin and proximity effects in practical machine. Moreover, by FEM analysis, the actual peripheral magnetic flux surrounding the winding wires and the current density distribution inside the wire cross-section can be directly reflected. The relationship between stator slot dimensions and winding copper loss is investigated by FEM, in [86], where it is found that the winding copper loss increases with increasing stator slot height and shortening of the slot opening. The copper loss of a form-wounded HSPMM have been calculated and discussed with the influence of slot shape on proximity effect considered in [87]. A new

computationally efficient computation method for SPM machine additional copper losses due to rotor motion is proposed in [88]; it requires solving a set of time-frequency finite element analysis (TFFEA) simulations on a suitably modified machine model. The permanent magnets in the model are replaced by a grid of fictitious conductors carrying sinusoidal currents. This model can accurately reproduce rotor motion effects and requires much less time than the time-stepping finite element method. The influence of PWM on winding proximity loss in a permanent magnet brushless machine is further investigated in [89].

Several researchers have focused on optimizing machine design to reduce winding copper loss with both skin effect and proximity effect considered. It has been reported that the primary winding wire position that determines copper loss is located at the stator slot opening. Hence, in order to decrease winding eddy current loss, it is advisable to decrease each wire diameter to enable all the wires in the winding to be held further away from the stator slot opening. This method is also effective at decreasing machine copper loss as the winding wires are wound in parallel. An optimal number of parallel wires can also be found for machines at a specific operational frequency to achieve the least copper loss by parallel wire configuration; smoothing of the current waveform can also be achieved as the harmonic components are supressed [74] [86]. The study of proximity loss with circulating currents for a high speed permanent magnet machine has been reported in [90]. It is found that using ducting to move coils to the stator slot surface increases the proximity losses; whereas windings that use a wedge at the slot top to fix the coils deeper in the slot have reduced losses.

2.2.3 Rotor eddy current loss

While not contributing significantly to HSPMM overall power losses, rotor eddy current loss does play an important role in high speed permanent magnet machine research; Rotor eddy current losses not only decrease the machine efficiency, but they also may lead to over-heating of the rotor. Moreover, a high strength rotor retaining sleeve is always employed in surface-mounted HSPMMs to ensure mechanical integrity of the rotor operating at high speeds. The PM material performance is also quite sensitive to its working temperature. If a large amount of heat is induced by rotor eddy current losses and it cannot be dissipated effectively,

then, over heating may occur increasing the risk of PM demagnetization. Therefore, it is critical to estimate rotor eddy current loss to ensure that HSPMMs operate reliably.

The major sources of rotor eddy current losses are as follows:

1) Air gap permeance variation due to stator slots [91];

2) Space harmonics of the stator magnetomotive force (MMF) [92];

3) Time harmonic components in the armature current [93];

Rotor eddy current loss can be researched analytically for permanent magnet machines. In [94], Prof Z. Zhu proposed a systematic analytical methodology to predict machine eddy current loss in both the PM and retaining sleeve for surface-mounted permanent magnet machines. This method is based on a two-dimensional polar coordinate model that accounts for the effects of curvature, time, space MMF harmonics and the rotor eddy current reaction field. However, this method neglects the stator slot effect. Equivalent current sheets covering the stator slot openings are utilized to represent the stator armature-conductors to predict the time-varying armature reaction field in [95]. A Fourier series expression method for the equivalent current sheets is adopted to calculate the armature reaction field; rotor eddy current losses due to the harmonics are predicted by the vector magnetic potential in magnets; then the total magnet loss is calculated as the sum of losses due to each harmonic. Based on a sub-domain field model, a surface-mounted permanent magnet machine analytical model that predicts the magnet eddy current loss due to the slotting effects is developed. In [96], it is shown to be capable of providing both high accuracy and loss generation insights. A sub-domain model for analytically calculating the open-circuit, armature reaction, load eddy current and joule losses is also illustrated in [97], where the influences of slot, tooth-tip, tooth body shape and current angle on permanent magnet loss are further studied. H. Toda *et al* [98] mention that permanent magnet segmentation is effective in reducing the eddy current loss, while Wang *et al* [99] further pointed out that when more than two segments per pole are employed in permanent magnet machines, the loss in each segment may be significantly different.

Though providing an intuitive method for permanent magnet machine eddy current loss estimation, the analytical approach to rotor eddy current loss estimation is by necessity based on some assumptions and simplifications. Therefore, FEM becomes a desirable and popular method for eddy current loss calculation. FEM is compared with experiment measurement in [100], and a good agreement has been found. FEM is also adopted in eddy current loss analysis for surface mounted-machines with different PWM duty ratios and supply voltages. It is found that eddy current loss becomes more significant with decreasing PWM duty ratio, indicating that PWM carrier harmonics also affect the rotor eddy current loss [101]. FEM utilized for permanent magnet machine rotor eddy current loss research can also be found in [102]-[105]. In order to take the effects of skewed stator and chamfered PM shape into consideration, three-dimensional (3D) FEM is employed to investigate the rotor eddy current loss for a 2 kW surface-mounted machine [106], while 3D FEM is used with an interior PM machine to consider magnet eddy current in [107] and [108]. As the 3D finite element approach to permanent magnet machine analysis is widely considered as time-consuming, [109] proposes a novel method which combines 2-D and 3-D finite element analysis to provide a much more efficient rotor eddy current loss calculation. This method consists of: firstly estimating the differential permeability at the average flux density of the rotor core by 2-D nonlinear time-domain analysis; then 3D frequency-domain finite element analysis at each remarkable harmonic field is carried out with this permeability. Using this approach, the calculation time for rotor eddy current loss can be greatly reduced while achieving accuracy levels that are nearly the same as the conventional method.

Surface-mounted permanent magnet rotors are the primary and most commonly used rotor topology in HSPMMs, and hence a high strength rotor retaining sleeve becomes necessary for rotor mechanical integrity when rotating at high speed. It is placed around the permanent magnets outer surface to enhance rotor strength. The conventional material utilized for sleeves can be mainly characterised as either metal or non-metal. If the sleeve around the rotor is made of a material with high conductivity, due to the sleeve shielding effect, the eddy current loss in permanent magnets can be reduced with the rotor primary eddy current normally located on the sleeve. By employing the electromagnetic shielding effect, a high conductivity material (such as copper) shield inserted between the sleeve and magnet is effective

at reducing the eddy current loss in magnets of the high speed permanent machine as proposed by [110].W. Li *et al.* [111] further propose that plating a copper layer on the alloy sleeve outer surface can dramatically reduce the stator MMF harmonics that penetrate into the sleeve and magnets; hence, machine rotor eddy current losses can be reduced. Moreover, it is pointed out that the axial segmentation of the rotor sleeve can help reduce rotor sleeve losses [112]. An easy method for high speed permanent magnet machine rotor eddy current loss reduction is to introduce rotor metal retaining sleeve grooving. This is due to the reason that the eddy current paths can be obstructed by both circumferential and axial grooves on the metal rotor sleeve; in addition, circumferential grooving has been proven to be the most effective solution to reduce rotor eddy current loss, while having little negative influence on sleeve mechanical strength and rotor dynamics [113].

2.2.4 Air frictional loss

In conventional or low speed electrical machines, it is not always necessary to focus on machine air frictional loss, as this loss is not significant and can be neglected in machine overall power losses. However, as the speed of high speed machine rotors can reach and even exceed 10,000rpm, the air frictional loss over the rotor surface is much higher than in conventional machines and cannot be neglected.

Air frictional loss is due to the frictional effect between the rotor surface and air gap. It is dependent on the rotational speed and rotor surface roughness: as the rotor speed increases, the relative speed gap between the rotor surface and its ambient air increases; thus, the frictional loss rises. As the machine rotor can be considered a cylinder, the analytical expressions for a cylinder model can be utilized for high speed machine air frictional loss estimation. However, such analysis is normally based on some empirical parameters with assumptions and therefore may not be in accordance with the practical machine operating conditions.

Therefore, CFD (computational fluid dynamics) analysis becomes an effective and functional method for high speed machine rotor air frictional loss research, as it can offer much higher precision solutions. In [114], a 3-D fluid analysis is carried out on the rotor air frictional loss of a high speed permanent magnet machine, whose rotor is magnetically suspended and the machine rated operational speed is up to 60,000 rpm.

The validity of the 3-D fluid analysis for high speed machine air frictional loss estimation is demonstrated by its close fit to experimental test results.

2.3 Temperature estimation for high speed machines

Temperature field analysis has a fundamental role in high speed machine research, as machine performance, efficiency and reliability are closely dependent on machine temperature. For permanent magnet machines, the permanent magnet material is commonly sensitive to operational temperature, and irreversible demagnetization may occur if the permanent magnets are operated at too high a temperature for an extended period. Moreover, due to the more compact size than other machine types, heat dissipation is more difficult with HSPMs. Therefore, in-depth research on thermal aspects of HSPMMs is needed to ensure machines operate with a high-level of performance and reliability.

Thermal analysis methods for machine temperature rise can mainly be characterised as: LPTN, FEM and CFD [115]. These are now briefly introduced.

1. LPTN

In the LPTN (Lumped-parameter thermal-network) method, the machine heat transfer process is abstracted from a thermal point of view and can be described via equivalent circuit diagrams [116]. The key point of the LPTN method is transferring the machine temperature field issues into circuit diagrams. Machine thermal LPTN is performed by dividing the machine into several components and representing these components by isothermal points, which are located at the interfaces between machine components. LPTN is able to calculate the average temperature rise in each machine component, but is unable to predict the temperature distribution for the whole machine. P. Ponomarev *et al* [117] reports the example of the LPTN process performed for a 46 kW, directly-oil-cooled permanent magnet machine with a thermal resistances equivalent network. It should also be pointed out that though a LPTN can simplify the thermal solving procedure and reduce solving time, its calculation precision is mostly dependent on the evaluated surface heat transfer coefficients. Hence, the LPTN method for machine temperature analysis requires experienced designers to get reasonable temperature results.

2. FEM

FEM has already been widely used as the fundamental mathematical method for electromagnetic and mechanical analyses. FEM not only suits models which have complex curves or curved boundaries, but are also sophisticated in tackling multiple boundaries with formal discrete equation forms that are amenable to computer programming. The procedures for electrical machine FEM thermal analysis are: machine modelling, model meshing and boundary condition application, as well as adding heat sources. By FEM analysis, the temperature for each element of the model can be obtained; then the temperature field distribution for the whole machine can be obtained. FEM is normally considered as time consuming, hence in some cases, FEM analysis can be utilized to estimate the equivalent thermal conductivity, which is then further applied in a network based analysis. FEM is also regarded as a suitable method for dealing with complex geometry that is not feasible for evaluation by LPTN analysis [118].

3. CFD

CFD (Computational fluid dynamics) can be utilized for thermal field analysis of electrical machines. CFD is based on the solution of Reynolds-averaged Navier–Stokes equations (RANS) that cover impulse transfer, mass convention and turbulence energy transfer [119]. CFD analysis can be used to model a fluid field precisely with convective heat transfer. The fluid state and temperature distribution in an electrical machine can be obtained with high precision by CFD analysis. Due to its advantages in fluid field analysis, CFD has already become a popular tool in electrical machine thermal field research. A CFD model for a radial flux permanent magnet synchronous machine with interior permanent magnets has been developed in [120]: cooling flow is directly considered in CFD, while water jacket cooling is also performed in the model. Good agreement can be achieved between measured and simulation temperature results, which verifies the effectiveness of CFD modelling in describing machine thermal behaviour. CFD was also used for temperature distribution estimation of a radial flux PM machine with a hybrid cooling scheme in [121] with temperature results for magnets and windings verified by experimental tests. Reference [122] also adopts CFD as a numerical 3D fluid-solid coupling calculation tool to investigate the temperature field distribution for a

30 kW, 96,000 rpm, air cooled high speed permanent magnet generator. Meshing technologies and substantial computer resources are required for application of the CFD method in electrical machine temperature field analysis. Hence, CFD analysis is also considered as time-consuming, and not suitable for use at the initial machine design stage. Therefore, a time-saving CFD method linked with LPTN is proposed in [123] for machine temperature estimation. This method has been applied and verified by measurement test on a 75 kW, 36,000rpm high speed permanent magnet motor with an open-circuit air cooling system.

2.4 Mechanical design for high speed machines

Rotor mechanical design is a primary consideration for high speed machines, as the high speed rotation brings prominent mechanical challenges in rotor strength and dynamics. Therefore, mechanical requirements should be satisfied by the rotor structure and configuration to ensure HSPMMs operate with high reliability.

2.4.1 Shaft bearing system

A key technology for a high speed machine is its bearing system. The bearings used in high speed machines are either ball bearings, air bearings or magnetic bearings. Ball bearings are the most commonly found bearing type in conventional machines. Ball bearings have the advantages of minimized volume and low manufacturing cost; however, ball bearings may also bring some drawbacks such as high mechanical losses if directly utilized for high speed machines. Air bearings employ a thin film of pressurized air to support the load; hence, no heat is generated from frictional effects. Air bearings can also maintain a high motion precision, and have been used for high speed machine drive systems. Magnetic bearings use electromagnetic force for rotor suspension. Normally, magnetic bearings can be divided into several types, namely, active, passive and hybrid. Active magnetic bearings are the preferred solution for high speed machines due to their advantages, which include being contactless, having adjustable dynamic shaft performance and low maintenance costs.

2.4.2 Rotor strength analysis

In order to avoid rotor mechanical failure due to the very large centrifugal force from high speed operation, rotor strength should be taken into consideration in the high

speed machine mechanical design process. It is noticeable that for HSPMMs with PM surface-mounted rotors, a high energy density permanent magnet material is normally utilized for magnetic excitation, such as NdFeB or SmCo. These PM materials can be characterized as being mechanically relatively strong, capable of withstanding large compressive stress but quite weak in tension. Therefore, a rotor sleeve, which is usually made with a high mechanical strength material, should be adopted outside the PM surface to ensure rotor mechanical integrity in high speed operation. Permanent magnet configurations and sleeve design are the important issues in HSPMM rotor strength analysis. Though analytical equations can be found for rotor stress analysis (as the machine rotor is normally considered as a solid cylindrical shape), FEM is always utilized for rotor strength research: as this allows more complex considerations, such as the nonlinear properties of the materials.

2.4.3 Rotor dynamics

Accurate prediction of rotor natural frequencies is another necessary topic in high speed machine mechanical design. In order to avoid unpleasant machine operation states, such as excessive acoustic noise and mechanical catastrophic failure, machine operational frequency should avoid approaching the rotor natural frequencies. Rotor natural frequency is determined by the rotor material properties and dimensional parameters (such as rotor structure, diameter and length). Both the transfer matrix method and FEM can be applied for machine rotor dynamics research. Though less calculation is required using the transfer matrix method, FEM has the advantage of high precision with the help of modern computer calculation [115]. The rotor natural frequency of a 1 kW, 28,000rpm high speed permanent magnet synchronous machine is studied using FEM in [124], with the calculation results validated using impulse force response test measurements. Rotor dynamics analysis for the comparison of two high speed PM machines was also performed using FEM by Z. Kolondzovski *et al.* [125].

2.5 Conclusions

This chapter extensively reviews the types of electrical machine used in high speed applications. Induction machines, switched reluctance machines and permanent

magnet machines are the main candidates for high speed direct drive applications. In this thesis, permanent magnet machines are selected for high speed applications due to their high efficiency and high power density advantages. Power losses in high speed permanent magnet machines (HSPMMs) have their own characteristics which differ from those of PM machines operating at conventional speeds. Rotor air frictional loss can be significantly increased and the rotor eddy current loss needs to be carefully estimated, as these losses directly heat the rotor. Thermal analysis is necessary for HSPMM design, with LPTN, FEM and CFD methods identified as the main approaches used for temperature estimation in high speed machines. In order to ensure machines operate reliability and safely in high speed operation, rotor mechanical strength and critical speeds should also be calculated for HSPMMs.

Chapter 3
High speed permanent magnet machine design and parameter effects

HSPMM manufactures use advanced materials and reasonable design dimensions to ensure machines operate with satisfactory performance and reliability. It is acknowledged that all machine electromagnetic, thermal and mechanical requirements should be satisfied to obtain a desirable machine scheme. The multi-physical fields in HSPMM act in a coupled fashion and they are constrained by each other. In addition, HSPMM power loss density is also higher than other conventional speed machines at the same power rating. High speed machine structure is by design

more compact, hence, it is more difficult to obtain effective rotor cooling. As surface-mounted PM rotor structures are always employed for HSPMM and the PM material is mechanically vulnerable in tension, extra protection methods are necessary for rotor mechanical integrity in high speed operation. Therefore, a high mechanical strength rotor outer sleeve is employed around the PM outer-surface to support it against the large centrifugal force induced by high speed operation (as shown in Fig 3.1). The addition of the rotor outer sleeve also has a critical impact on machine electromagnetic and thermal behaviour accordingly as will be discussed in the following chapters of this dissertation.

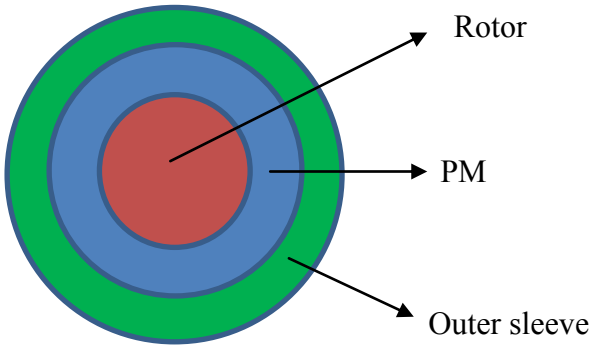

Fig. 3.1 high speed surface-mounted PMSM rotor

3.1 HSPMM design process

As introduced above, HSPMM performance is determined by the coupled machine multi-physical fields interaction, and the HSPMM design should ensure that the machine operates within a desirable performance envelope under mechanical and thermal constraints. Therefore, the desired HSPMM design scheme should yield a reasonable power loss density distribution, high rotor mechanical strength and stiffness, as well as an effective cooling system for the machine. Then the design process for a HSPMM can be derived as shown in Fig 3.2. It can be seen that HSPMM design is an iterative process between multi-fields until a reasonable machine scheme can be obtained.

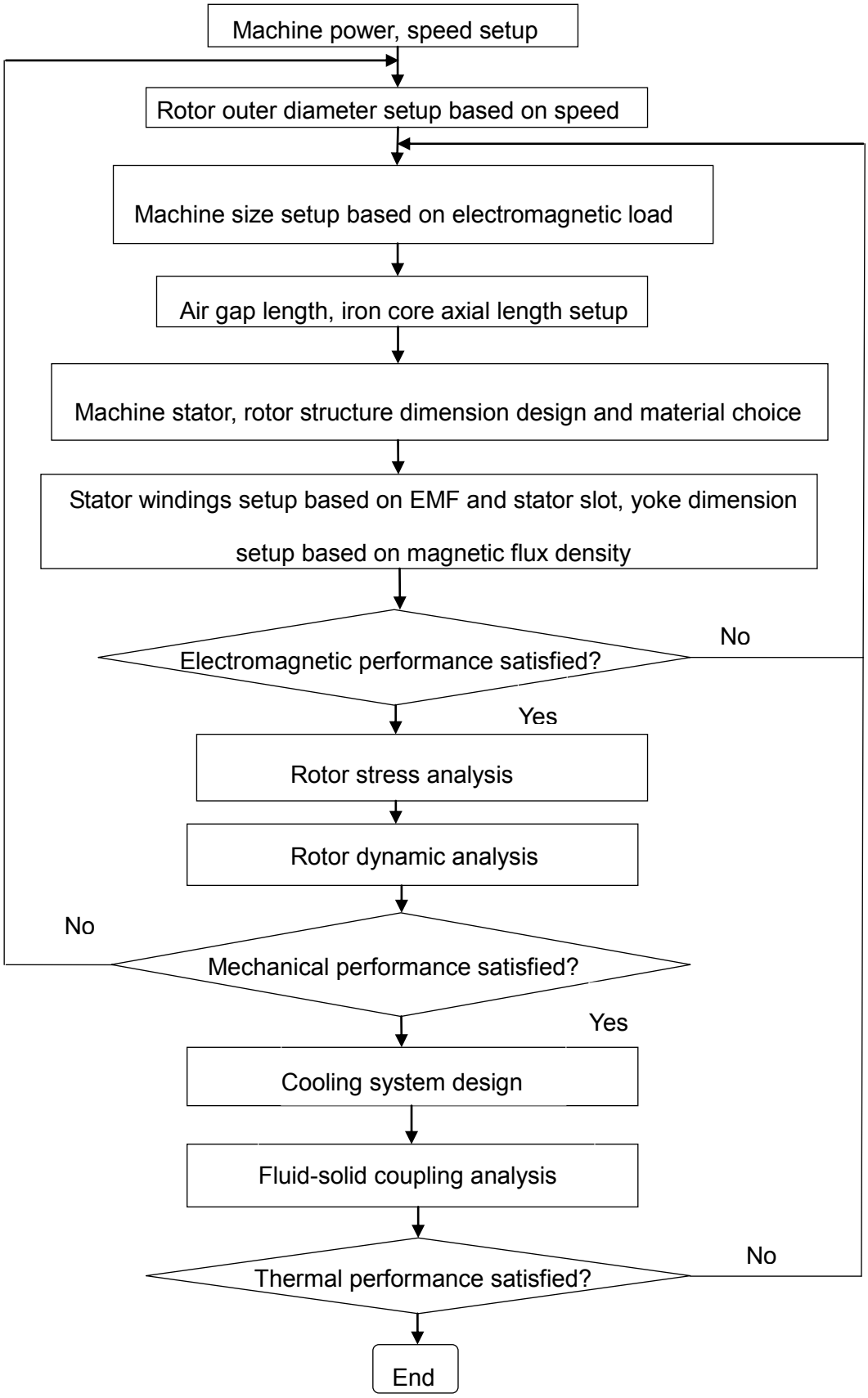

Fig. 3.2 high speed PM machine design process

3.2 HSPMM rotor material and parameters optimization

3.2.1 Rotor outer diameter

Due to the high speed rotation, the HSPMM rotor experiences a larger centrifugal force. Hence, it is required that each rotor component should have sufficient strength to bear the centrifugal force. The rotor outer diameter is a critical parameter in HSPMM electromagnetic design: as the machine stator outer diameter is always set based on the machine frame and the air gap length for HSPMM is normally set around 1-2.5 mm, the machine inner stator diameter can be also predicted initially. The rotor strain induced by the centrifugal force during rotation is:

$$\sigma = \frac{\rho D^2 \omega^2}{4} \tag{3.1}$$

where σ is rotor strain, ρ is material density, D is rotor outer diameter and ω is rotational speed. Rotor strain under high speed operation should satisfy the mechanical constraints:

$$\sigma \le \frac{[\sigma]}{S} \tag{3.2}$$

where $[\sigma]$ is the permitted material strain, and S is the safety factor which is normally set as a value between 1.5 and 2.0. Substituting (3-1) into (3-2), yield the rotor outer diameter constraint as:

$$D \le \frac{2}{\omega}\sqrt{\frac{[\sigma]}{S\rho}} \tag{3.3}$$

Table 3.1 Inconel 718 mechanical properties

Density	Yield Strength	Tensile Strength
8220 kg/m^3	1172 MPa	1407 Mpa

Table 3.1 shows the mechanical properties of Inconel 718, a material often used for rotor shaft construction. Using this material, the rotor maximum outer diameter as given by the equations above is presented in Fig.3.3:

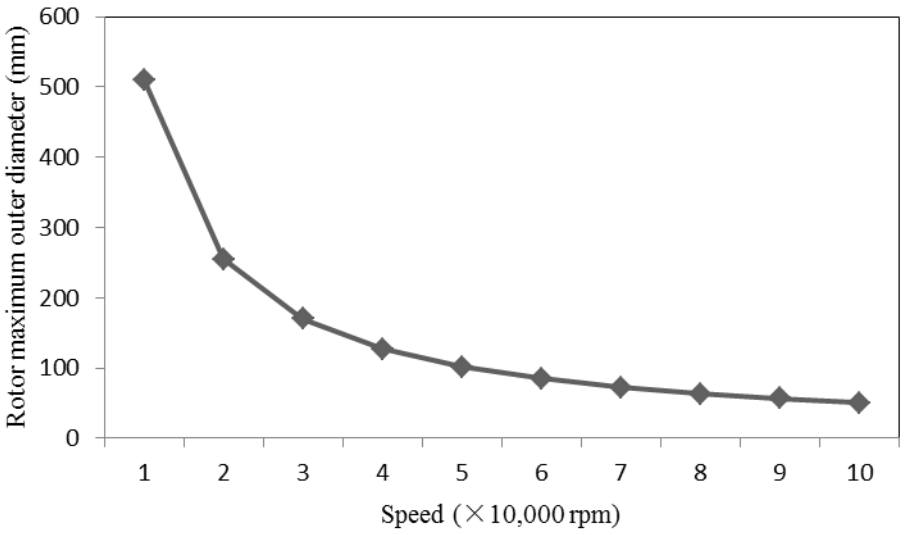

Fig. 3.3 Rotor maximum outer diameter at different operating speeds

3.2.2 Permanent magnet material choice for HSPMM

Permanent magnets can be used to replace the electrical equipment for magnetic excitation employed in conventional machines. Machine performance and operational stability are closely affiliated to PM material characteristics. Therefore, it is necessary to have a discussion on PM material for HSPMM and the characteristics required to achieve a desirable performance level.

Materials which can be magnetized and generate their own persistent magnetic field are called ferromagnetic. They include iron, nickel and some rare earth alloys. The ferromagnetic materials can be further divided into magnetically soft materials and magnetically hard materials: magnetically hard materials tend to remain magnetized after magnetization; conversely, magnetically soft materials tend not to maintain their magnetized state after magnetization. The typical hysteresis loop for a ferromagnetic material is shown in Fig.3.4 (a): the variation of flux density B lags behind the variation of magnetic field strength H. If the magnetic field strength increases from $-H_m$ to H_m, the flux density B increases through the locus from d-e-f-a; as the magnetic field strength decreases from H_m to $-H_m$, the B decreases through

the locus from a-b-c-d; flux density B is not zero when magnetic field strength H comes to zero. So in order to demagnetize a saturated magnet, a certain demagnetization magnetic field should be applied, and the threshold is based on the magnetic material coercivity (point C): The magnetically hard material has high coercivity, whereas the magnetically soft material has low coercivity.

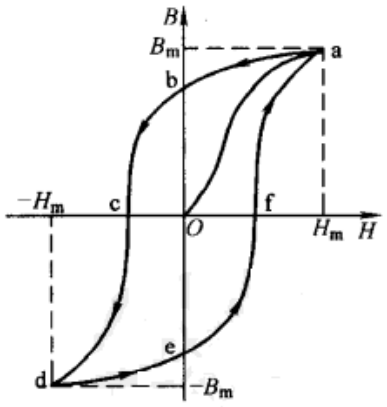

(a) Hysteresis loop for a ferromagnetic material

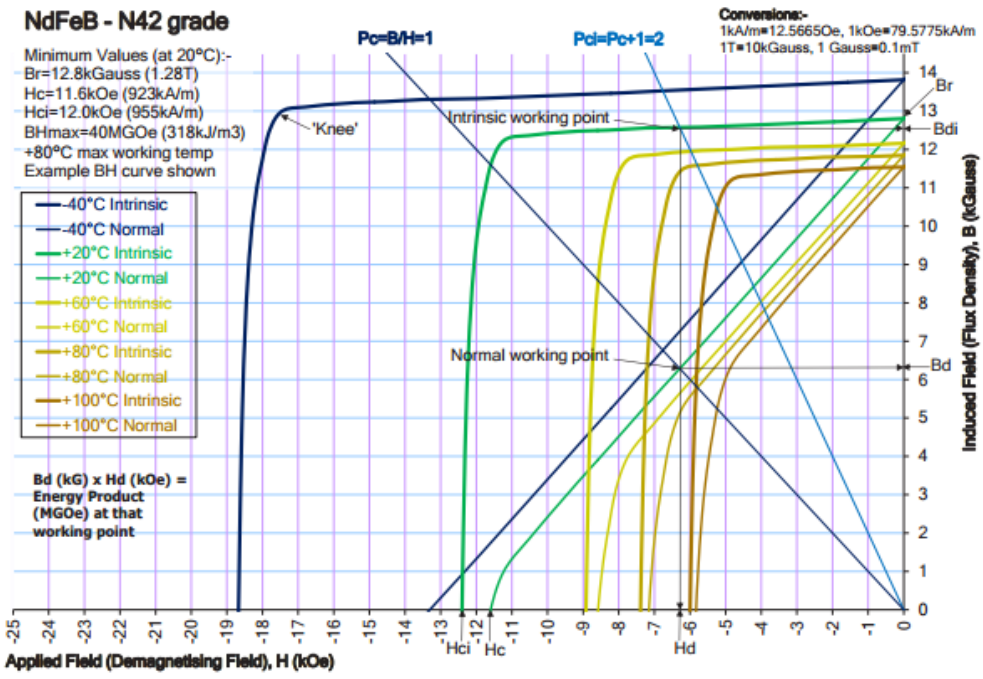

(b) Characteristic demagnetization curves for NdFeB permanent magnet (N42).

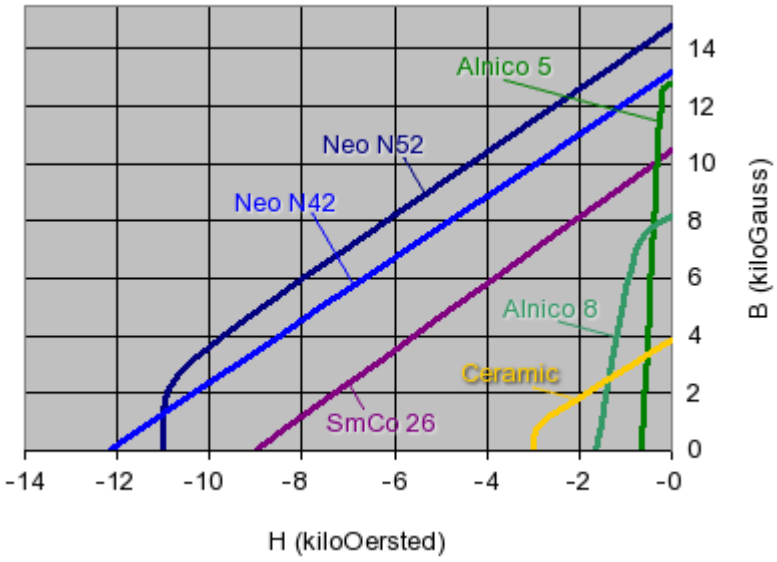

(c) Demagnetization curves for different permanent magnet materials at 20 °C.

Fig. 3.4 Materials B-H curves

Permanent magnets are made from magnetically hard materials which maintain a high coercivity and high remanence after magnetization. The typical permanent magnet materials utilized in electrical machines include ferrites and rare-earth material alloy composites such as NdFeB (chemical formula: $Nd_2Fe_{14}B$) and SmCo (chemical formula: $SmCo_5$). Fig. 3.4 (b) further presents the characteristic demagnetization curves for NdFeB PM (Grade: N42) at different temperatures (from https://www.eclipsemagnetics.com/media/wysiwyg/datasheets/magnet_materials_and_assemblies/ndfeb_neodymium_iron_boron-standard_ndfeb_range_datasheet_rev1.pdf). It is noted that the knee point on the B-H curve is an important threshold, as irreversible demagnetization will occur if PM working below the knee point.

Ferrite is a type of ceramic compound composed of iron oxide (such as Fe_2O_3) combined chemically with one or more additional metallic elements. The main types of ferrite magnet are $BaFe_{12}O_{19}$ and $SrFe_{12}O_{19}$. Ferrite has some degree of magnetic coercivity and low manufacturing cost, and is widely used in household products such as refrigerator magnets, micro-wave devices and magnetic recording. Rare earth magnets are a type of permanent magnet with high remanence and large corecivity made from alloys of rare earth elements. They produce much stronger magnetic fields than achievable with ferrite magnets. Nowadays, the rare-earth magnet materials normally used include SmCo and NdFeB: SmCo magnets have higher

Curie temperature, and are suitable for applications where high magnetic strength is desired at high temperatures; NdFeB magnets are able to offer higher magnetic field strength than SmCo magnets at a lower manufacturing cost. PMs can also be divided

Table 3.2 Property comparison for different PM materials

	Remanence (T)	Coercivity (kA/m)	BHmax (kJ/m^3)	Curie temperature (°C)	Maximum operation temperature (°C)	Density (g/cm^3)
Ferrite (sintered)	0.2-0.8	100-300	10-40	450-460	200	4.5-5.1
Ferrite (bonded)	0.15-0.17	110-135	4.0-5.5			2.6-3.7
SmCo (sintered)	0.8-1.1	600-2000	120-200	720	300	8.1-8.3
SmCo (bonded)	0.5-0.7	180-560	80-160			3.0-6.5
NdFeB (sintered)	1.0-1.4	750-2000	200-440	310-400	180	7.3-7.5
NdFeB (bonded)	0.6-0.7	600-1200	60-100			5.0-6.3

by manufacturing method, namely sintered and bonded. Sintered PMs are manufactured by having the raw material melted, cast into a mold and cooled to form ingots. The ingots are pulverized and milled to produce a powder, which is then sintered into dense blocks, heat-treated, cut to shape, surface treated and magnetized. Bonded NdFeB magnets are manufactured by first melt spinning a thin ribbon which contains randomly oriented NdFeB nano-scale grains. Then the ribbon is pulverized into particles, mixed with a polymer, and either compression- or injection-molded into bonded magnets. Sintered PMs are superior in their capability to generate larger magnetic flux density; while bonded PMs have the advantage of being more easily formed into mechanical intricate shapes with higher dimensional precision and more robust mechanical features. Demagnetization curves comparison for different permanent magnet materials are present in Fig. 3.4 (c) (from https://www.kjmagnetics.com/blog.asp?p=magnet-grade). A more detailed comparison of different PM material performances is also presented in Table 3.2.

It is noticeable that rare earth permanent magnet materials are vulnerable and fragile with regard to their tensile strength. Therefore, a high strength rotor retainer sleeve is always employed around the surface-mounted PM for high speed applications. PM materials are also sensitive to their ambient temperature, with their performance degrading if it becomes too high. This arises due to rotor power loss and the limited heat dissipation capability in HSPMMs. It is therefore critical to avoid HSPMM performance degradation by PM irreversible demagnetization due to overheating.

3.2.3 Rotor pole number choice

The number of pole pairs for HSPMM is normally chosen from 1 or 2 to reduce the machine power supply frequency. 2-pole high speed machines have the advantage of ensuring rotor dynamic balance and require lower power supply frequency, which benefits machine power loss reduction. However, 2-pole machine end-winding length is normally long, which may lead to lower rotor dynamics mechanically. In contrast, 4-pole machines have shorter shaft axial length. However, more PM material has to be assembled around a 4-pole rotor and the machine also requires a higher power supply frequency.

3.2.4 Rotor sleeve selection

PM materials can normally withstand large compressive forces; however, they are vulnerable to tensile forces. Therefore, a high mechanical strength rotor sleeve is utilized to protect the PM and maintain the tensile stress experienced by the PM to within an acceptable range. A rotor sleeve becomes a necessary component in HSPMMs as it effectively avoids PM damage induced by the large centrifugal force from high speed rotation. The dimension for the rotor sleeve is selected based on factors such as sleeve material, rotor structure and rotational speed. Conventional materials for high speed rotor sleeves can be constructed from a metal alloy or from non-metals (such as glass or carbon fiber). Metal alloy sleeves can prevent high order harmonic components penetrating into the PM, hence, reducing PM loss. However, notable eddy current loss will also be generated in the protective metal alloy sleeve due to its relatively high electrical conductivity. High strength non-metal materials have also been used for rotor sleeves in HSPMMs. Unlike metal alloy, the non-metal (such as carbon or glass) fibre rotor sleeve has low electrical conductivity, hence, the HSPMM rotor can benefit from eddy current loss reduction in the sleeve itself; however, the fibre sleeve is less effective at stopping the high order harmonic components penetrating into the PM. In addition, the fibre material also has poor thermal conductivity compared to a metal alloy, which is a disadvantage with regard

Table 3.3 Mechanical properties of several rotor bandage materials

	Glass fibre	Carbon fibre	Titanium alloy	Inconel718
ρ(g/cm3)	2.54	1.80	4.50	8.20
σ_{Lmax}(MPa)	3447	800	1000	1030
λ(W/(m·K))	1.0	0.9	7.2	11.4
ρ(Ωm)	4.0×10^{12}	3.0×10^{-5}	1.6×10^{-6}	1.25×10^{-6}

to the HSPMM rotor thermal heat dissipation capability. Table 3.3 provides a comparison of the mechanical properties of several commonly used rotor sleeve materials for HSPMMs.

3.3 HSPMM stator structure design

Stator structure is critical in electrical machine design as multiple machine performance metrics, such as torque performance and power losses, are closely affiliated to it. In order to investigate the stator structure effect on HSPMM performance, several machine schemes, which have different stator slot-pole fits, are designed and modelled in FEM (finite element method) software for comparison. The cross-sections for each slot-pole fit machine are shown in Fig.3.5, respectively; machine parameters for 2 pole machines (a, b, c) are also listed in Table 3.4. In addition, it should be noted that each 2 pole machine shares identical stator, rotor and

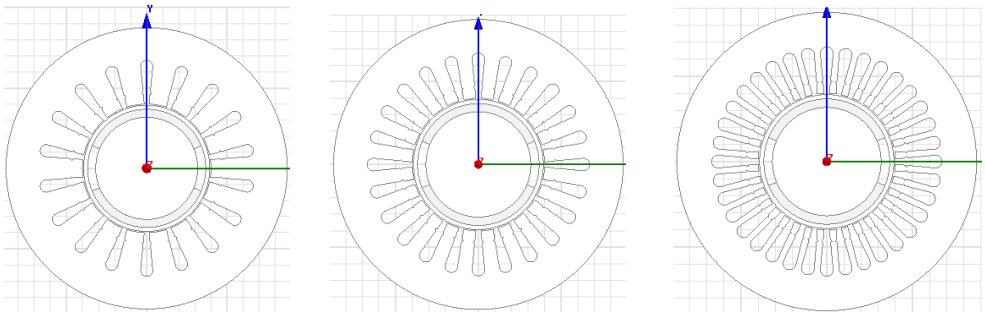

(a) 18 slots 2 pole (b) 24 slots 2 pole (c) 36 slots 2 pole

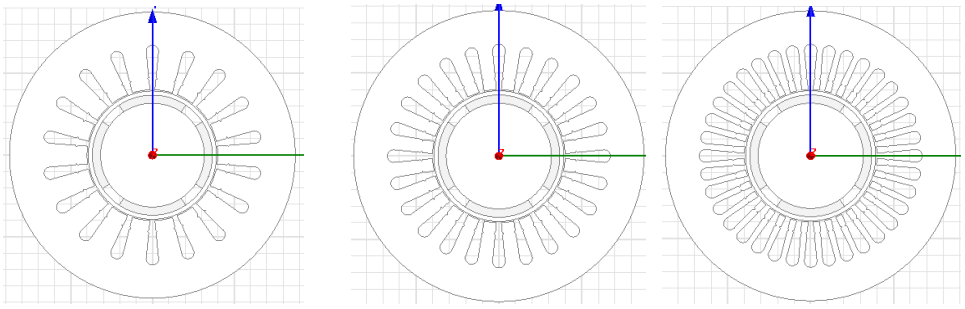

(d) 18slots 4 pole (e) 24slots 4 pole (f) 36 slots 4 pole

Fig.3.5. Cross-section for different stator slot-pole configurations

Table 3.4 Machine parameters for 2 pole machines

	(a)	(b)	(c)
Power(kW)	150	150	150
Speed(rpm)	17000	17000	17000
Pole numbers	2	2	2
Phase number	3	3	3
Slot number	18	24	36
Stator outer diameter (mm)	350	350	350
Stator inner diameter (mm)	160	160	160
Air gap length	1.5	1.5	1.5
Rotor out diameter (mm)	157	157	157
Sleeve thickness (mm)	5	5	5
Pole arc to pole pitch	0.75	0.75	0.75
PM pole thickness (mm)	10	10	10
Iron core length (mm)	140	140	140
Conductor number each slot	8	6	4

PM parameters with its corresponding 4 pole counterpart with the same stator slot numbers: hence, the 4 pole machine dimensions are not listed. Short-pitched windings are utilized for all machines. In this study, a high strength carbon fibre sleeve is wound around the rotor PM outer surface to protect the PM from damage and maintain rotor integrity in high speed operation. In this study, machine electromagnetic analysis is performed by Ansys Maxwell due to its rich calculation functions in application.

3.3.1 Cogging torque impacts by slot-pole configurations

Cogging torque, which impacts on the machine output performance, is focused on and valued in permanent magnet machine design research. Cogging torque is a torque that tends to make the rotor remain at certain positions and prevent the machine rotating smoothly, and is caused by the magnetic co-energy variation within permanent magnet machines. Cogging torque T_{cog} can be defined as:

$$T_{cog} = -\frac{\partial W}{\partial \alpha} \tag{3.4}$$

where W is the magnetic co-energy and α is the machine rotor position angle [126]. Several papers have proposed design methods to improve machine torque performance and suppress cogging torque ripple, such as different magnet width methods [127], skewing [128], optimization of the pole arc coefficient [129], fractional number of slots per pole [130] and so on.

For the HSPMM considered in this study, the cogging torque waveforms of different slot-pole configuration machines for the rotor at different mechanical positions (from 0 to 90 degree) are studied by FEM and presented in Fig.3.5. It can be concluded that machine cogging torque performance varies periodically, and the variation cycle is based on machine slot-pole fits. The cogging torque periodical variation number N at one stator slot pitch can be written as [126]:

$$N = \frac{2p}{GCD(z,2p)} \tag{3.5}$$

where p is the machine pole pair number, z is the stator slot number and *GCD (z, 2p)* represents the greatest common divisor of z and pole number $2p$. It can also be

observed from Fig 3.5 that the more periods of the cogging torque ripple that occur in one machine mechanical rotation period, the smaller the cogging torque that is obtained. This is referred to as the cogging torque ripple periodicity and its value is relevant to the harmonic components of the air gap magnetic flux density: the higher the periodicity of the harmonic components in air gap flux density, the smaller the corresponding harmonic component amplitudes; hence the cogging torque ripple amplitude becomes smaller accordingly. Therefore, it is desirable to choose a slot-pole configuration for HSPMMs that increases the cogging torque periodicity in one machine rotation cycle such that the cogging torque impact on output torque performance is decreased.

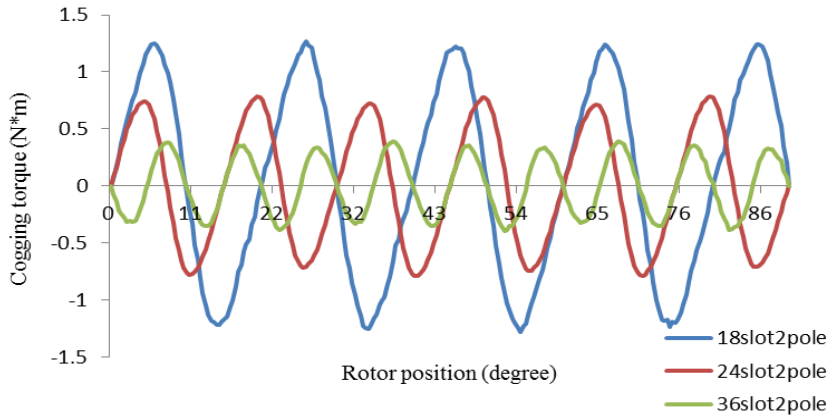

(a) 2 pole machine

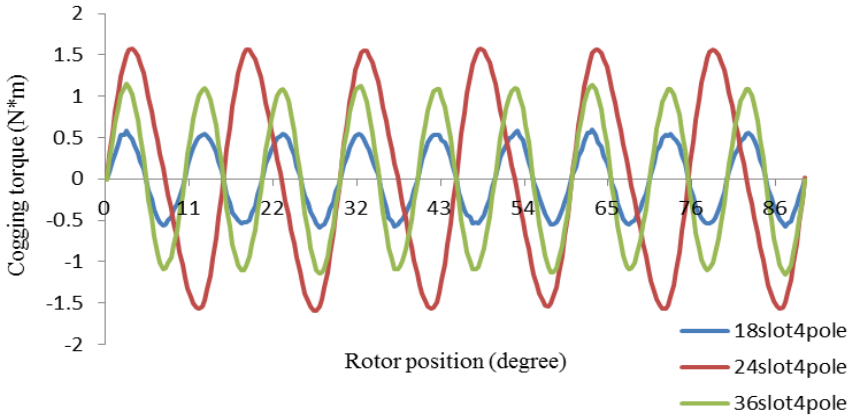

(b) 4 pole machine

Fig.3.5 Cogging torque for different slot-pole configurations

3.3.2 Back EMF analysis by stator structure

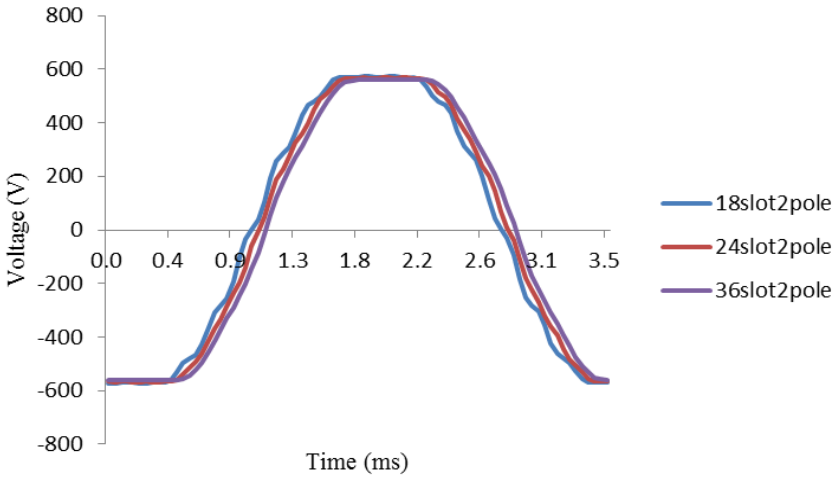

(a) 2 pole machine EMF

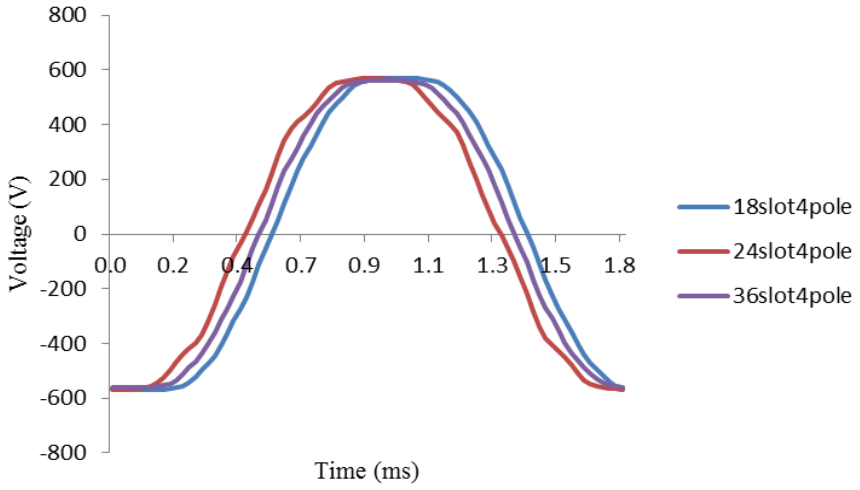

(b) 4 pole machine EMF

Fig. 3.6 Back EMF for different slot-pole configurations

Table 3.5 Slot-pole configuration fundamental component amplitude

Slot/pole	18/2	24/2	36/2	18/4	24/4	36/4
Amplitude (V)	630	629	625	622	612	612

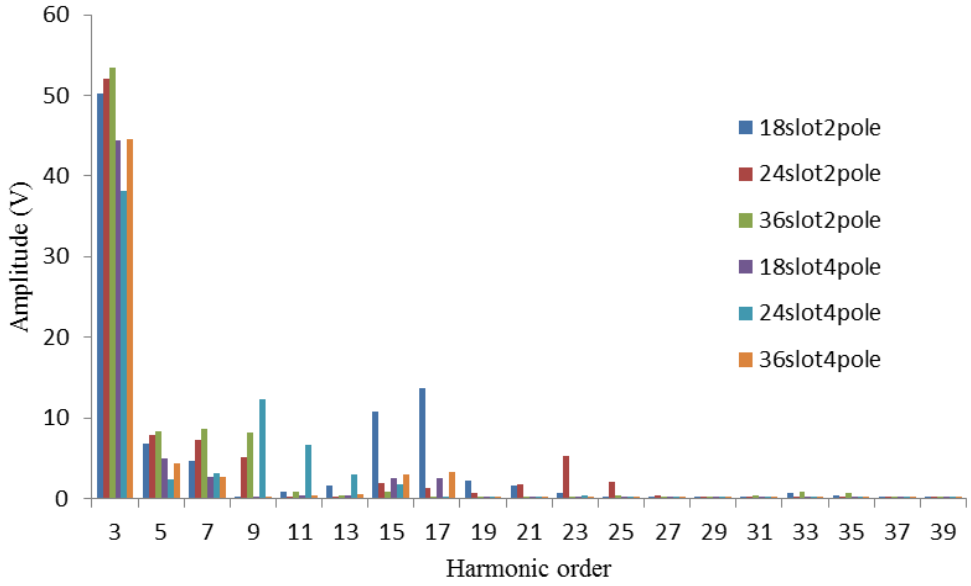

Fig.3.7 Harmonic components amplitudes

Synchronous machine output torque capability is reflected in its back EMF (Electromotive force), which proves to be an important machine performance indicator. EMF is generated by the rate of change in magnetic flux linage with respect to time, with a sinusoidal waveform desirable for permanent magnet machines under BLAC operation. Fig 3.6 presents phase EMF waveforms for different slot-pole fit machines at rated speed (17,000 rpm) in one electrical period, while their FFT analysis results are shown in Table.3.5 and Fig.3.7, respectively. The total number of phase coils in series connection for the HSPMMs are kept the same to investigate the effects of stator slot number on EMF. From Fig. 3.7, it can be seen that the fundamental voltage component amplitude decreases slightly as slot numbers increase, as the 18slot-2pole machine has displayed the largest fundamental amplitude of 630 V; The main harmonic orders for different slot-pole fit machines are the odd ones, while the largest amplitude harmonic components occurs at third order (this can be eliminated in line-voltages if the machine windings are Y connected). It is also noticeable that the teeth order related harmonic components are prominent in FFT results. Teeth related components are due to the spatial stator slotting effect. As the teeth harmonic order increases, the corresponding harmonic amplitude decreases. There are some design methods to suppress tooth harmonic components in PM machines, such as stator (or pole) skewing and application of a magnetic wedge in the stator slots.

3.3.3 Losses comparison with machine stator structure

Power loss is a critical factor in electrical machine performance; hence, it is desirable to decrease machine power losses: not only benefiting machine efficiency improvement, but also assisting in HSPMM temperature rise restriction. The main electromagnetic power losses for HSPMMs are considered as steel core iron loss and winding copper loss. In addition, as introduced in section 3.1.2 the PM material performance is sensitive to its operational temperature, so machine rotor eddy current loss is also carefully considered in HSPMM research. Iron loss and eddy current

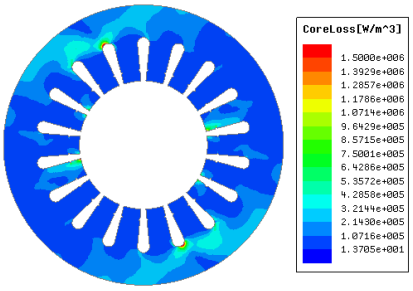

(a) 18slot-2pole

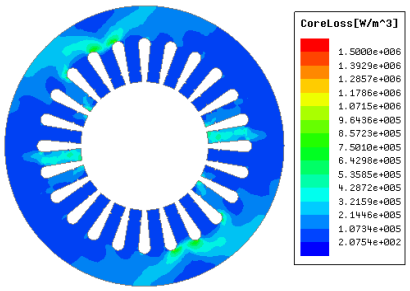

(b) 24 slot-2pole

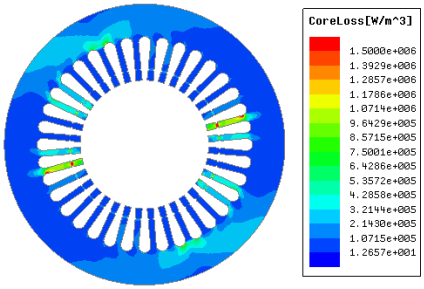

(c) 36slot-2pole

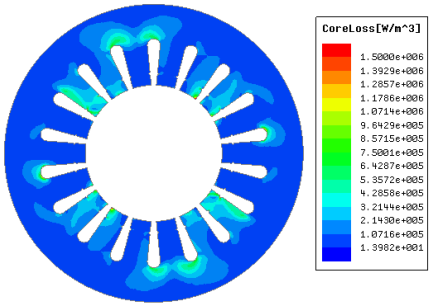

(d) 18slot-4pole

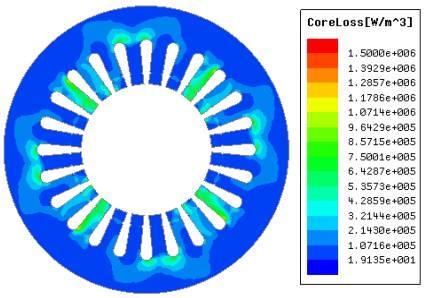

(e) 24 slot-4pole

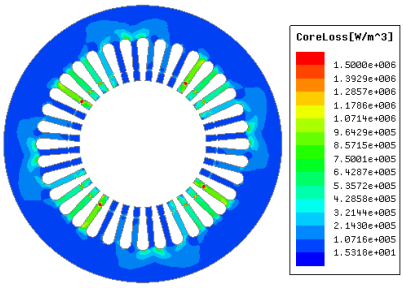

(f) 36slot-4pole

Fig. 3.8 core iron loss density distribution

loss for the above slot-pole fit HSPMMs at rated condition are calculated by 2-D FEM software, while the stator core iron loss density distribution and rotor eddy current loss density distribution for permanent magnet and rotor sleeve are presented in Fig.3.8 and Fig.3.9, respectively; Fig. 3.10 compares machine rotor eddy current loss and iron loss further. It is noted that all the machines are modelled with the same air gap length, stator slot opening width and power rating.

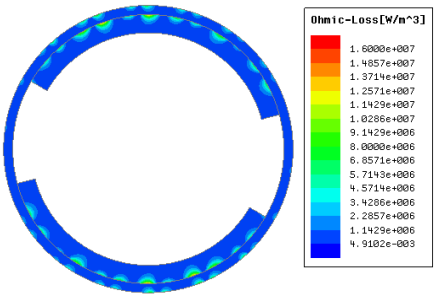

(a)18 slot-2pole

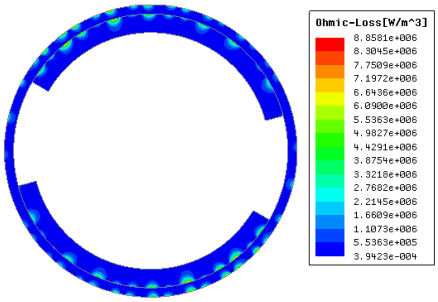

(b) 24 slot-2pole

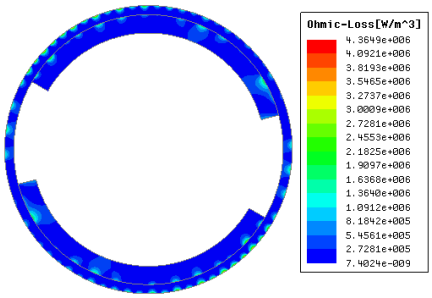

(c) 36 slot-2pole

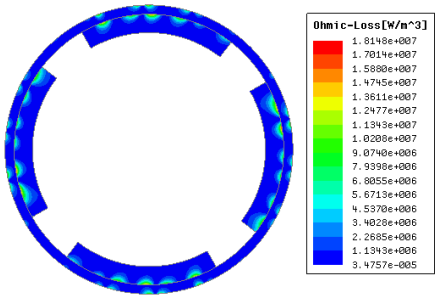

(c) 18slot-4pole

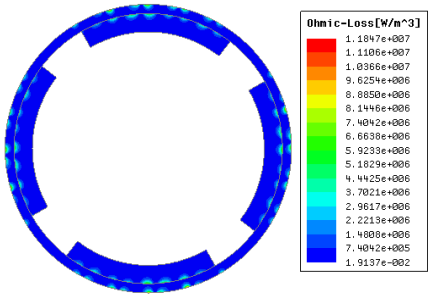

(d) 24slot-4pole

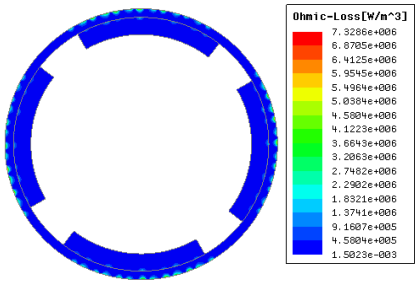

(f) 36slot-4pole

Fig. 3.9 Rotor eddy current loss density distribution

From Fig.3.9, it can be observed that the eddy current loss is not evenly distributed over rotor PM and sleeve cross-sections due to harmonics penetrating depth effects.

The maximum value of the Joule loss density is closely dependent on machine structure and varies dramatically with machine slot-pole configurations: for the 18 slot-4 pole HSPMM, its Joule loss density can reach 1.814×10^{7} W/m^3, while the maximum Joule loss density of a 36 slot-2 pole machine is only up to 4.365×10^{6} W/m^3.

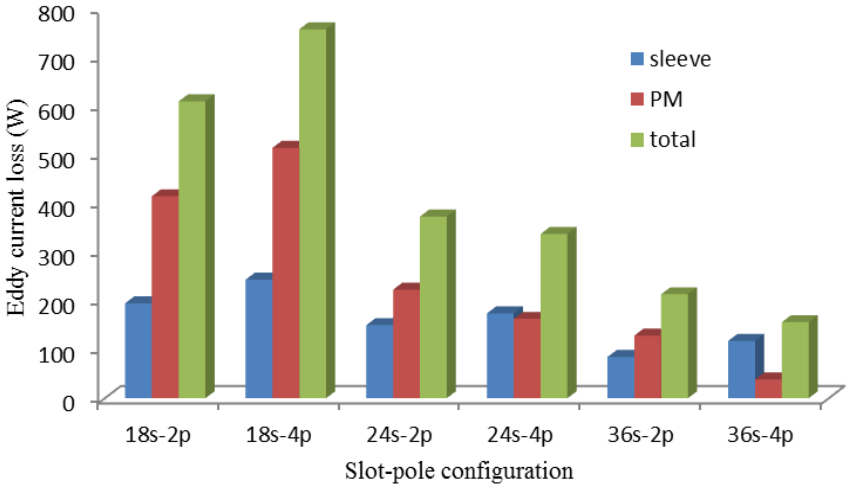

(a) Rotor eddy current loss

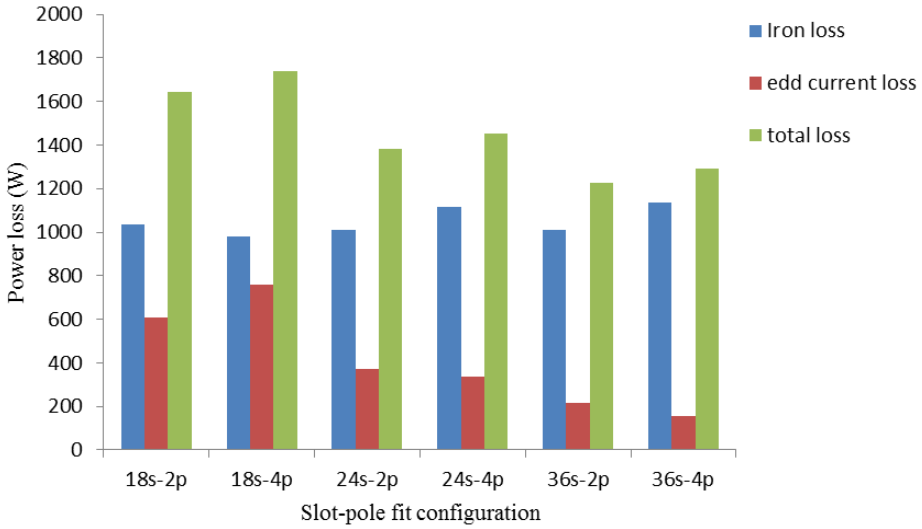

(b) Iron loss and eddy current loss

Fig. 3.10 Eddy current loss and iron loss for different slot-pole configurations

From Fig.3.10 (a), it is found that rotor eddy current loss is also dependent on machine structure: The 36 slot-4 pole fit PM machine has the lowest eddy current loss when compared with other slot-fit PM machines; while the 18 slot-4 pole fit machine has the highest rotor eddy current loss. With increasing stator slot number, machine total rotor eddy current loss decreases dramatically: the loss reduction effect is mainly due to PM loss minimization. Hence, it is advisable to choose a large stator slot number for HSPMMs for rotor eddy current loss reduction. In addition, it can also be observed that with the same stator slot number, machine rotor eddy current loss in the sleeve also increases slightly if a 4-pole rotor structure is chosen. High order harmonic components in the HSPMM air gap magnetic field have asynchronous speeds to the rotor, which induces rotor eddy current loss accordingly. Determined by stator structure, spatial high order harmonic components have different effects on the rotor sleeve and PMs: hence, machine slot-pole fit selection is critical to HSPMM rotor eddy current loss. It can be observed from Fig. 3.10 (b) that machine slot-pole does not have much influence on HSPMM iron loss, as all the machines have a similar iron loss level of around 1000 W. This is due to the fact that machine iron loss is mainly determined by machine iron core magnetic flux density and frequency.

3.3.4 Torque and torque ripple

Table 3.6 presents the torque and torque ripple radio comparisons for the machines with different stator structures. Torque ripple radio is defined as the radio of peak-to-peak torque value to average torque value as:

Table 3.6 Torque and Torque ripple ratio for machines with different stator structures

Slot/pole	18/2	24/2	36/2	18/4	24/4	36/4
T_{avg} (Nm)	113.1	113.0	110.9	112.6	109.2	110.7
K_T	7.6%	6.5%	5.6%	3.6%	4.3%	4.2%

$$K_T = \frac{T_{\max} - T_{\min}}{T_{avg}} \% \tag{3.6}$$

where T_{max} and T_{min} are the maximum and minimum values of the machine torque waveform, respectively; T_{avg} is the torque average value. Machine average output torque is not greatly impacted by stator/slot combinations. 18s/4P machine features the least torque ripple radio, while torque ripple radio is not severe for all the machines.

3.4 Impacts of pole arc to pole pitch ratio on machine performance

Pole arc to pole pitch ratio is defined as the ratio of the PM width angle to pole pitch angle [131]: it has a critical impact on machine performance, including the EMF waveform, cogging torque and output torque ripple. Reference [132] utilizes the optimal pole arc to pole pitch ratio setting to achieve machine minimum cogging torque performance for interior permanent magnet machines. For the 36 slot, 4 pole HSPMM in this study, no load air gap magnetic flux density waveforms under one pair poles are shown in Fig 3.11 (a) with pole arc to pole pitch ratios (from 0.6 to 1). Their spectrums are also presented in Fig. 3.11 (b) for comparison. It can be clearly observed that with increasing pole arc to pole pitch ratio, the fundamental component in the machine air gap magnetic flux density rises; the 3rd harmonic component accounts for relatively high amplitudes in the machine air gap flux density harmonics

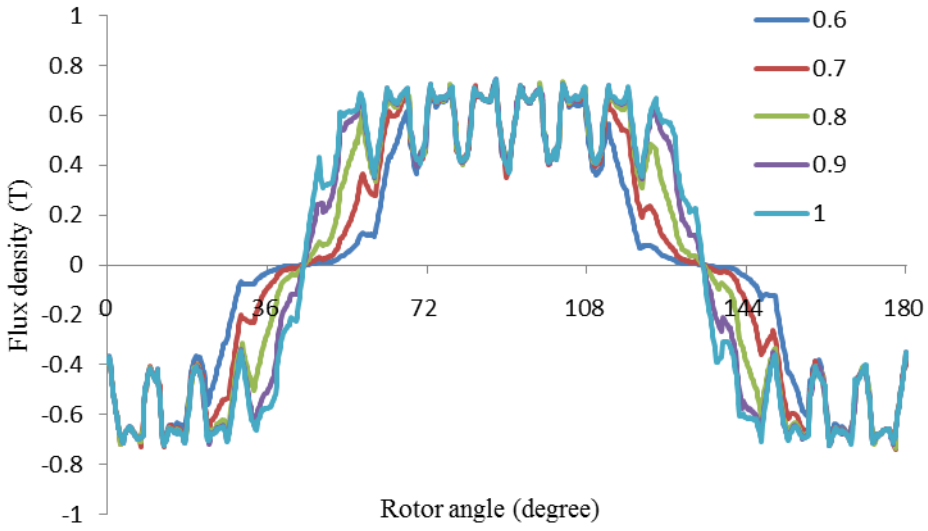

(a) Air gap magnetic flux density under different pole arc to pole pitch ratios

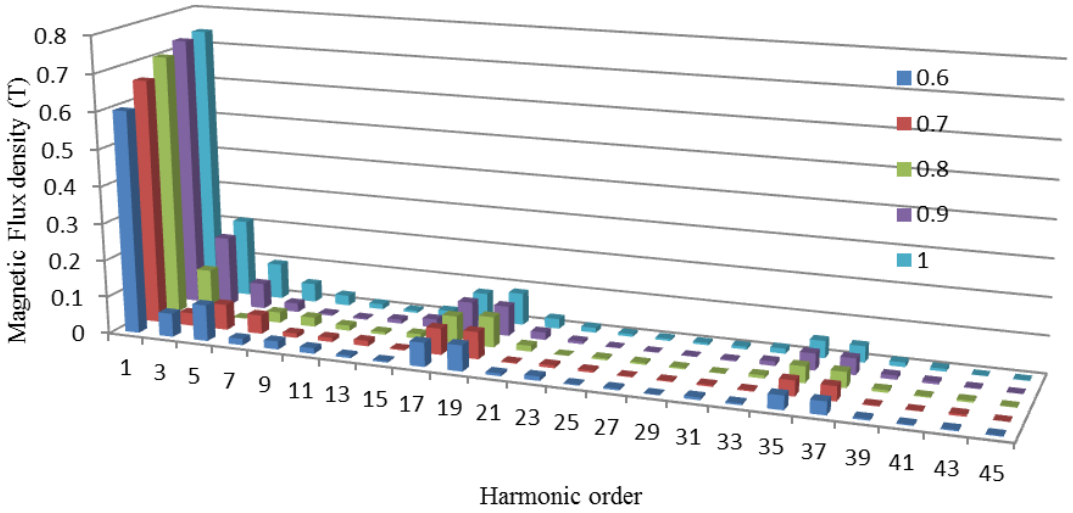

(b) Spectrum under different pole arc to pole pitch ratios

Fig. 3.11 No load air gap magnetic flux density with spectrums

spectrum. Moreover, the main harmonic components are due to the teeth related harmonics within the whole pole arc to pole pitch ratio range: these higher order harmonics are dependent on machine stator slot number and pole pair number.

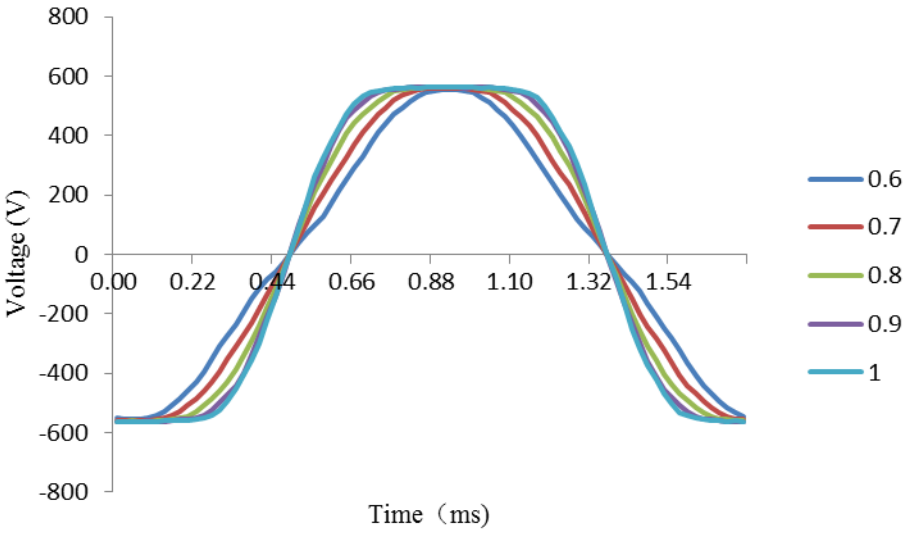

Fig. 3.12 No load phase EMF under different pole arc to pole pitch ratios

No load phase EMF waveforms for different machine pole arc to pole pitch ratios are displayed and compared as shown in Fig. 3.12. It can be observed that pole arc to

pole pitch also dramatically impacts machine EMF waveform width at the most top position in one electrical period. Hence, it can be deduced that harmonic components in the spectrum also differ with machine pole arc to pole pitch ratios. Table 3.7 compares the phase EMF fundamental component amplitude and its proportion in spectrum by FFT analysis with the HSPMM pole arc to pole pitch ratios:

Table 3.7 FFT analysis for no load phase EMF

	0.6	0.7	0.8	0.9	1
Fundamental Amplitude	536 V	590 V	630 V	654V	662 V
Fundamental Proportion	99.771%	99.936%	99.428%	98.806%	98.543%

It can be observed from the table that with the increase in pole arc to pole pitch ratio from 0.6 to 1, the fundamental amplitude of the phase EMF is also increased from 536V to 662V. However, the fundamental proportion in the spectrum does not follow a similar trend. Instead, this peaks when the machine pole arc to pole pitch ratio is chosen at 0.7, and drops of slightly as the ratio is increased from 0.7 to 1. The minimum proportion occurs when the pole arc to pole pitch ratio is set as 1. Therefore, although enlarging HSPMM pole arc to pole pitch ratio is beneficial to the increase in the EMF fundamental component, the amplitude of harmonic components also increase: hence, a compromise should be achieved between the fundamental amplitude and proportion in EMF for HSPMM design.

Fig. 3.13 illustrates the comparison of the HSPMM average output torque as a function of pole arc to pole pitch ratios when the machine is powered by the same power source. The average torque increases with the increase of pole arc to pole pitch ratio; but the torque rise trend is not significant for pole arc to pole pitch ratios above 0.8. In addition, as introduced above, overly large pole arc to pole pitch ratios

will also result in machine EMF waveform distortion and fundamental component proportion reduction in the spectrum. Table 3.8 further presents the machine torque ripple radio K_T with respect of pole arc pole ratio. It is found that the minimum torque ripple radio is obtained when the pole arc pole pitch radio is selected as 0.8. Hence, rotor pole arc to pole pitch ratio should be carefully chosen for HSPMMs.

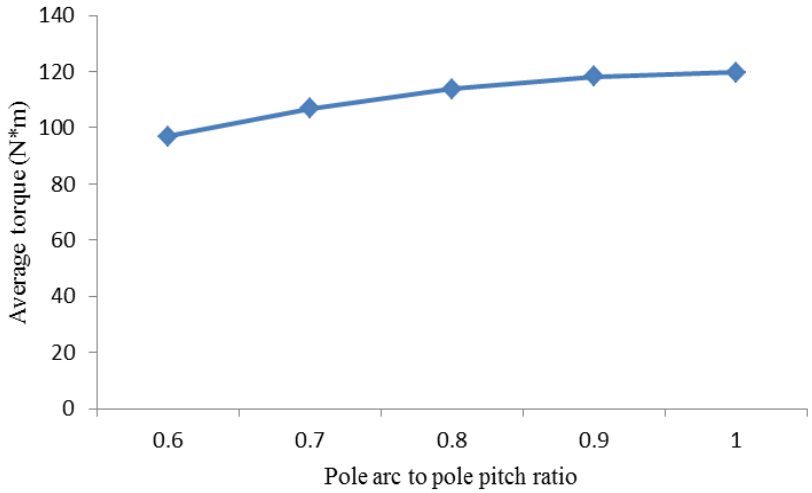

Fig. 3.13 Average torque under different pole arc to pole pitch ratios

Table 3.8 Torque ripple radio with respect of pole arc pole pitch radio

Pole arc to pole pitch radio	0.6	0.7	0.8	0.9	1.0
K_T	5.6%	3.7%	1.3%	4.7%	7.6%

3.5 Conclusions

In this chapter, machine design and the effect of parameters on HSPMM performance are discussed and illustrated. The detailed HSPMM design process is displayed at first; then the effect of rotor structure on machine performance is presented with several PM materials compared for HSPMM; then HSPMM structures with different slot-pole fits are modelled by FEM, while the effects on

machine electromagnetic performance metrics, such as cogging toque, back-EMF and power loss, are also displayed and compared. It is found that HSPMM rotor eddy current loss is dramatically influenced by stator structure selection, with a 36slot-4 pole machine structure presenting the least rotor eddy current loss. The influence of pole arc to pole pitch ratio on machine performance is also investigated, and it is concluded that an overly large pole arc to pole pitch ratio may also decrease the fundamental component proportion in the back EMF spectrum of the machine.

Chapter 4
Power loss analysis for high speed permanent magnet machines

As HSPMM electromagnetic frequency is much higher than conventional speed machines, HSPMM electromagnetic losses should be taken into account as losses act as machine heat sources; moreover, due to the frictional effect between the rotor surface and the air gap, mechanical losses can also be significant when machine is in high speed operation. Therefore, it is necessary to research HSPMM power losses: not only to assess machine efficiency, but also to estimate the machine temperature rise. In this chapter, HSPMM power losses, including iron loss, rotor eddy current loss and mechanical air frictional loss, are studied and discussed comprehensively.

4.1 HSPMM iron core loss research

Iron loss, which is due to magnetic field variation in the iron steel laminations, contributes a considerable proportion to the total HSPMM power losses. Based on the modern magnetic material physical model developed by Bertotti [72], iron loss P_{iron_loss} can be divided into hysteresis loss P_h, eddy current loss P_e and anomalous loss P_a, that is:

$$P_{iron\ loss}=P_h+P_e+P_a \tag{4.1}$$

Hysteresis loss, which is caused by the hysteresis phenomenon in the magnetic response of the iron steel, is modelled as:

$$P_h = K_h f B_m^{\alpha} \tag{4.2}$$

where K_h and α are the hysteresis loss coefficient and Steinmetz coefficient, respectively, f is the frequency and B_m is the flux density amplitude. Eddy current loss is induced by the eddy current flowing in the iron core where it is placed in an alternating magnetic field. The eddy current loss is given by:

$$P_e = K_e f^2 B_m^2 \tag{4.3}$$

where K_e is the eddy current loss coefficient. It can be seen that eddy current loss increases with the square of frequency. As the rotational speeds of HSPMMs are usually of the order of ten thousand rpm and their frequencies are much higher than conventional speed machines, eddy current loss represents a considerable proportion of the overall machine iron loss. Anomalous loss represents losses that are in addition to the hysteresis and eddy current losses, and are considered to be as a result of localized eddy current effects near moving domain walls. Anomalous loss is a power function of frequency and flux density:

$$P_a = K_a f^{1.5} B_m^{1.5} \tag{4.4}$$

where K_a is the anomalous loss coefficient. The iron loss coefficients in the Bertotti model can be obtained through iron loss measurements on iron steel. These will be introduced in the next section.

4.1.1 Iron core loss coefficients

To decrease high speed machine iron loss, thin (0.2mm) silicon steel electrical laminations (B20AT_1500) are utilized as the machine iron core laminations and oriented along the machine axial direction. The silicon steel material density is 7680 kg/m^3; its power loss characteristics are measured with a series of B-P (iron loss) curves against frequencies obtained as shown in Fig 4.1. It can be observed that iron losses increase dramatically with frequency.

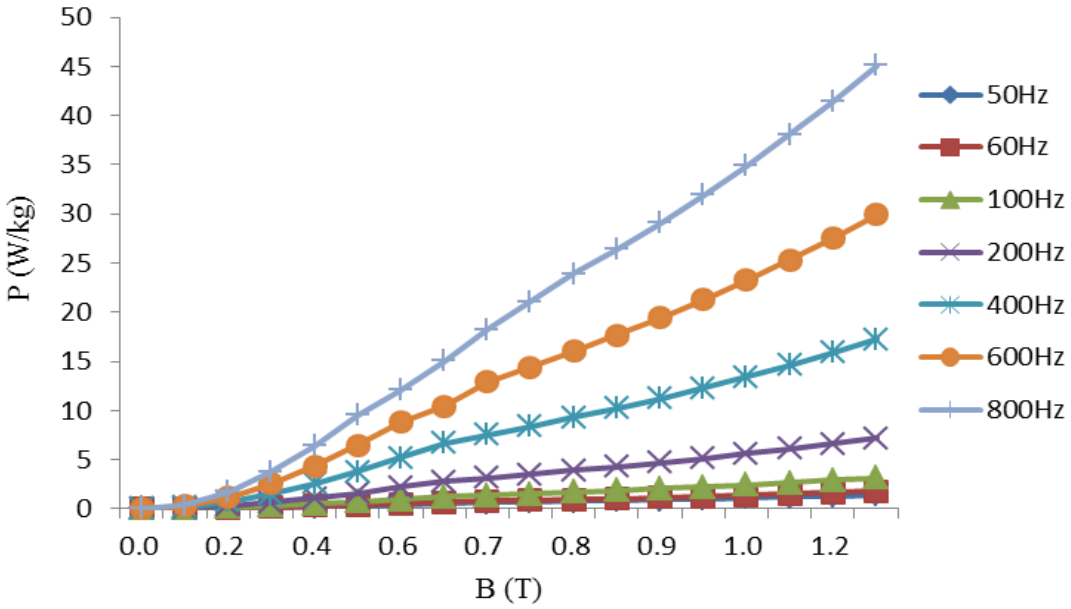

Fig 4.1 Measured core loss against frequencies

Table 4.1 HSPMM iron core loss coefficients

Coefficient	Value (w/kg)
K_h	0.023
K_e	3.38×10^{-5}
K_a	9.56×10^{-6}
α	1.98

From the B-P loss curves above, steel core loss coefficients (K_h, K_e and K_c) can be

obtained by minimizing the quadratic cost function:

$$err(K_h, K_e, K_a) = \sum_{i=1}^{m}\sum_{j=1}^{n}[P_{ij} - (K_h f_i B_{ij}^{\alpha} + K_c f_i^2 B_{ij}^2 + K_a f_i^{1.5} B_{ij}^{1.5})]^2 \quad (4.5)$$

where m is the number of power loss curves; n is the number of points for the i^{th} loss curve; *err* is the error between the actual measured iron loss and the model estimated. This curve fitting method yields the HSPMM iron core coefficients given in Table 4.1.

4.1.2 HSPMM iron core magnetic field analysis

A range of numerical methods can be utilized to solve electromagnetic fields problems, including the finite differential method (FDM), boundary element method (BEM) and finite element method (FEM). Of these FEM is the most popular method for electrical machines magnetic field analysis. FEM provides approximate solutions to boundary value problems with differential equations. FEM subdivides a large domain problem into a series of simpler and smaller parts (which are called finite elements) in the analysis; then equations that represent these divided finite elements are assembled into a larger matrix modelling the whole domain region; boundary conditions and initial values are also applied to approximate the numerical solution for the researched domain. FEM is widely acknowledged to be a suitable and effective calculation tool for solving complicated domain and boundary problems (such as the moving boundary that is commonly found in electrical machine research). In this study, a 36 slot, 4-pole, 17,000 rpm HSPMM is designed with its main parameters listed as shown in Table.4.2:

As illustrated by Bertotti's iron loss model, besides iron loss coefficients of the iron core, machine core flux density is also critical in iron loss estimation. In order to take the flux density diversity at different machine core regions into consideration, five characteristic points representing different stator tooth and yoke locations in one stator slot pitch are taken as shown in Fig 4.2. Their flux density waveforms for HSPMM at rated speed in one electrical period are obtained by time-stepping FEM. Core magnetic density is studied under cylindrical coordinate with radial component (as Br) and the tangential part (as Bt). The magnetic waveforms and magnetization locus for these points are presented in Fig 4.3:

Table 4.2 Parameters for high speed PM machine

Rated power	150 kW	Rated frequency	566.67 Hz
Winding rated current	142 A	Stator outer diameter	350 mm
Stator inner diameter	160 mm	Steel core stack length	140 mm
Air gap length	1.5 mm	Conductors per slot	4
Winding form	Double layer	Stator slot opening width	6 mm
Stator slotting depth	47 mm	Rotor sleeve outer diameter	157 mm
Rotor sleeve thickness	5 mm	Permanent magnet thickness	10 mm
Permanent magnet material	NdFeB	Pole arc pole pitch	0.75
Permanent magnet grade	N38UH	Permanent magnet remanence	1.15 T
Permanent magnet coercivity	875 kA/m	Permanent magnet conductivity	625000 S/m

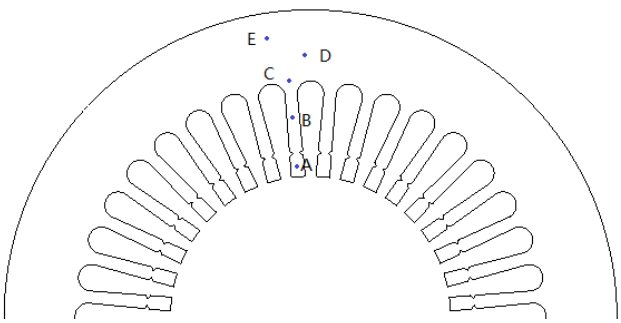

Fig 4.2 Stator iron core

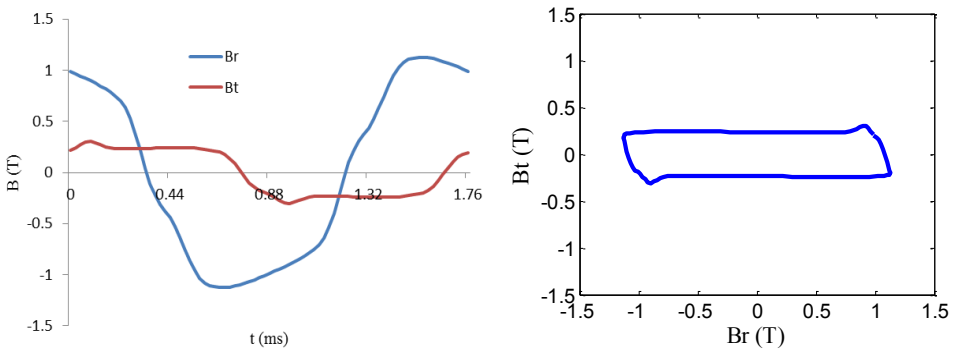

(a) Point A

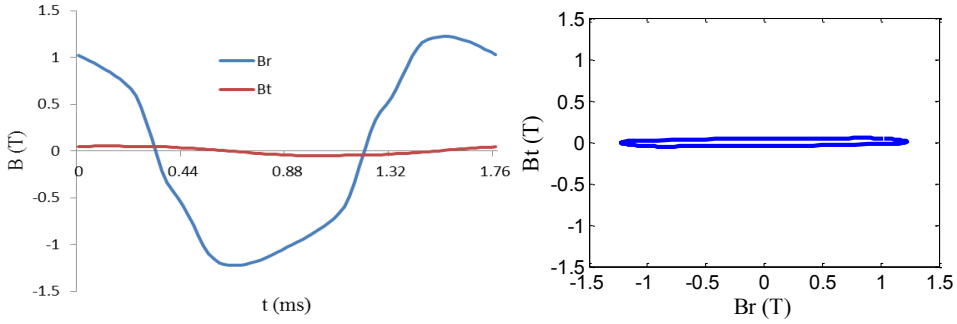

(b) point B

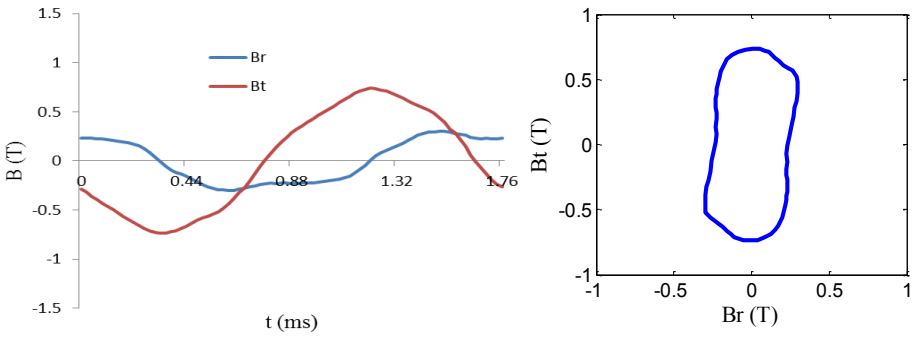

(c) point C

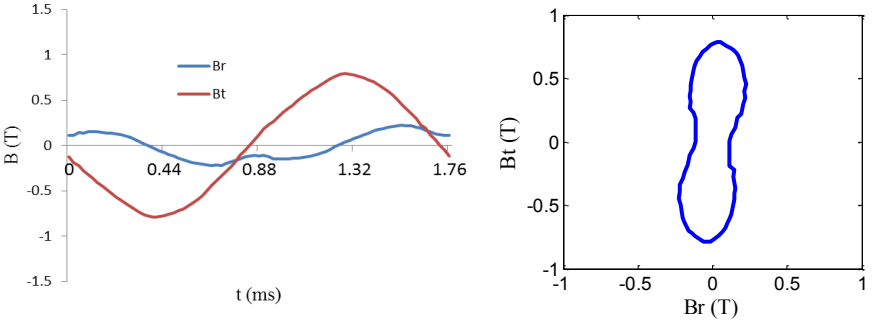

(d) point D

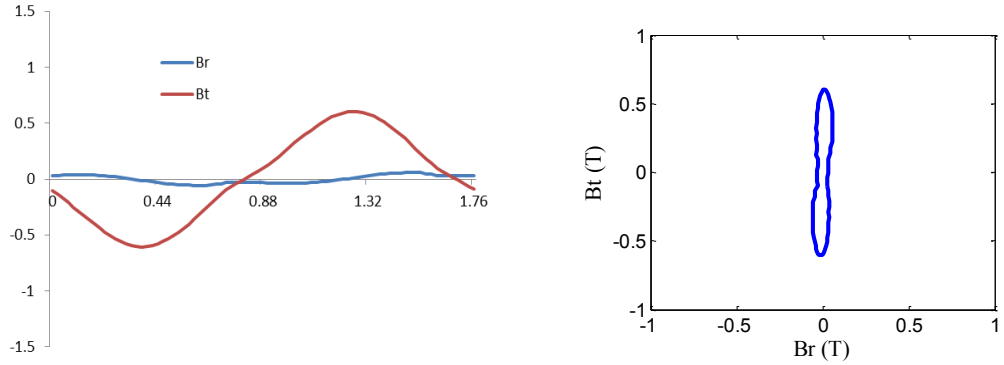

(e) point E

Fig 4.3. Stator magnetization property at different stator points

It can be seen that the magnetization characteristic in the steel core is complicated, as it varies dramatically with different core locations: the magnetization in the middle of the stator tooth (point B) can be approximately deemed as alternating magnetization, while for the other points in the stator core, especially at the tooth root position (point C), the rotational magnetic fields has considerable effect on the magnetization locus. Therefore, the type of magnetization in the stator is complicated: it is neither a pure alternating magnetization nor a pure rotational magnetication, hence, it can be considered to be an elliptical magnetization. If the ellipse short axis is zero, it becomes alternating magnetization; if the ellipse short axis is equal to the long axis, it becomes rotational magnetization. So both the alternating magnetic field effect and the rotational magnetic field effect should be taken into consideration for precise evaluation of HSPMM iron loss. Due to the spatial symmetry of the machine structure and temporal periodicity of the rotational magnetic field, the points with integral stator tooth pitches have the same radial and tangential magnetic density waveforms with a temporal difference. Hence, machine iron loss estimation for the whole machine can be performed based on the analysis of the flux density variation of one stator slot pitch.

4.1.3 Improved iron loss model for HSPMM

In the Bertotti iron loss model, machine iron loss is considered based only on the alternating magnetization of the core, which is dependent on the frequency and magnetic flux density amplitude in the steel core without the actual flux density waveform considered. However, the magnetic flux density in the HSPMM core is not

an ideal sinusoidal waveform with harmonics included. The FFT analysis results for Br and Bt for point C are displayed as shown in Fig 4.4. The high frequency harmonics in the core flux density also increase the iron loss in HSPMMs. To consider the effect of magnetic flux density harmonics, the flux density of each point in the machine stator core is decomposed into fundamental and a series of high order harmonic components, and the machine total iron loss is obtained by summing up the core losses due to each harmonic. To consider the magnetization effects on the stator core, for the k^{th} order magnetic harmonic ellipse locus, it is decomposed into two vertical alternating magnetic fields - the one with long axis flux density B_{kmax} and the one with short axis flux density B_{kmin}. In other words, the ellipse magnetic field of the point in the stator core is represented by two vertical alternating magnetic fields. The improved method for HSPMM iron loss estimation with more precision, therefore, proceeds as following:

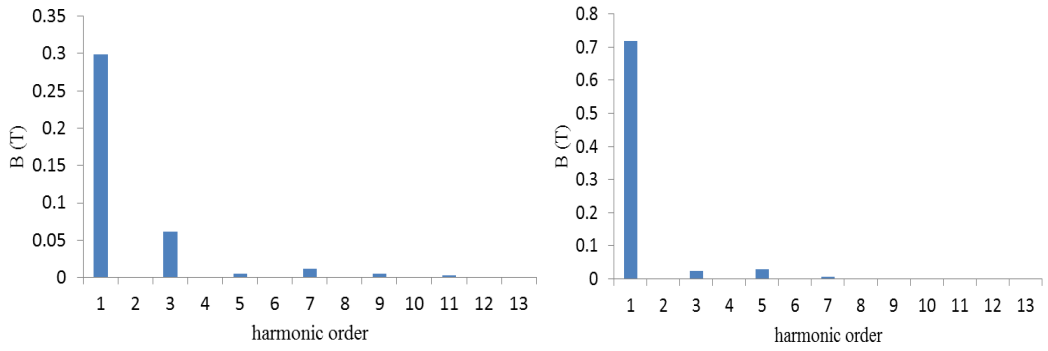

(a) Br (b) Bt

Fig. 4.4 FFT analysis results for point C

The hysteresis loss density is computed as:

$$P_h = \sum_{i=1}^{N} k_h kf (B_{k\max}^{\alpha} + B_{k\min}^{\alpha}) \tag{4.6}$$

The eddy current loss density is computed as:

$$P_e = \sum_{k=1}^{N} k_e (kf)^2 (B_{k\max}^2 + B_{k\min}^2) \tag{4.7}$$

and the anomalous loss density is estimated as:

$$P_a = \frac{1}{T}\int_0^T k_a \left(\left| \frac{dB_r(t)}{dt} \right|^2 + \left| \frac{dB_t(t)}{dt} \right|^2 \right)^{\frac{3}{4}} dt \tag{4.8}$$

where B_{kmax} and B_{kmin} are the major and minor axes of the k^{th} order harmonic elliptical magnetic field locus; and $B_r(t)$ and $B_t(t)$ are the radial and tangential components of the magnetic field, respectively.

Based on the HSPMM 2D FEM analysis results, the flux density waveform for each element of the machine core can be obtained. For the i^{th} element on the core, the iron loss density for element i (P_{iron_i}) can be calculated as:

$$P_{iron\_i}=P_{h\_i}+P_{e\_i}+P_{a\_i} \tag{4.9}$$

where P_{h_i}, P_{e_i} and P_{a_i} are the hysteresis loss, eddy current loss and anomalous loss of element i. Therefore, machine total iron loss can be calculated as:

$$P_{iron} = \sum_{i=1}^{N} p_{iron\_i} \rho \Delta_i l \tag{4.10}$$

where N is the total number of elements in the steel core, ρ is steel core mass density, Δ_i is the area of element i, and l is the machine steel core lamination stack length. Combining the FEM results and the analytical method for machine iron loss estimation, both alternating and rotational magnetic field effects can be considered in iron loss estimation to achieve high precision.

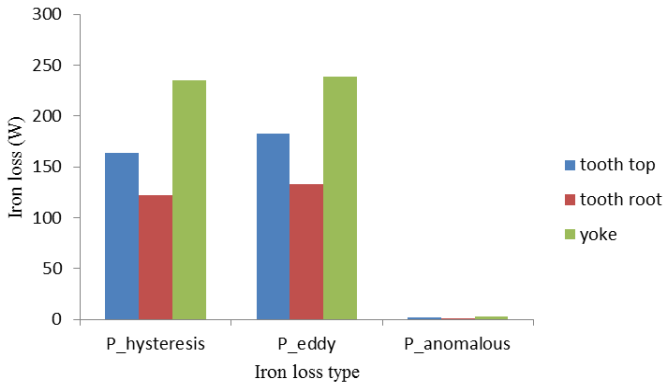

Fig4.5 Breakdown of iron loss components for different stator core locations

The iron loss components for different stator core locations on the HSPMM at rated

speed are shown in Fig.4.5. It can be seen that the majority of iron loss components are due to the hysteresis loss and eddy current loss components.

The iron losses due to the magnetic harmonic components are compared in Table. 4.3. It can be observed that the majority of machine iron loss is due to the fundamental magnetic field: however, the iron loss due to the high order magnetic field harmonic components is also a considerable proportion (9.7%) of the machine total iron loss. The high order magnetic harmonic component that contributes most to the machine iron loss is the 3rd magnetic harmonic in the iron core.

Table 4.3 Iron loss due to each harmonic

Harmonic order	1	3	5	7	9	11	13
Iron loss (W)	971.27	64.05	8.66	16.48	11.47	2.92	0.45

Table 4.4 Iron loss for the high speed PM machine at different operating speeds

Speed (rpm)		8000	11000	14000	17000	20000
Frequency(Hz)		266.67	366.67	466.67	566.67	666.67
P_h (W)	Meth1	228.92	314.76	400.60	486.45	572.29
	Meth2	245.25	337.09	429.12	521.36	613.14
P_e(W)	Meth1	100.72	190.43	308.47	454.83	629.52
	Meth2	123.62	231.79	375.17	554.61	767.71
P_a(W)	Meth1	1.27	2.02	3.33	4.79	6.39
	Meth2	1.82	2.93	4.20	5.63	7.18
P_{iron}(W)	Meth1	330.89	507.21	712.40	946.07	1208.20
	Meth2	370.69	571.81	808.49	1081.59	1388.04

With both conventional (based on Bertotti iron loss model) and improved iron loss calculation methods (referred to as Meth 1 and Meth 2, respectively) applied to HSPMM, iron losses are estimated by the two methods for the machine operating at different speeds. The calculation results are shown and compared in Table 4.4.

It can be observed that the improved iron loss calculation considering both rotational magnetic field and harmonic effects is 135 W (35 W for hysteresis loss and 100W for eddy current loss) higher than that by conventional method for machine at the rated speed (17,000 rpm). For machine operation at a low speed, the major component in iron loss is hysteresis loss; as machine speed increases, the eddy current loss rises dramatically and becomes the largest proportion of total iron loss. Eddy current loss is more sensitive to machine speed as it is proportional to the square of the iron core magnetic field frequency. Compared to the conventional iron loss estimation method using equations (4.2) to (4.4), the improved method improves the iron loss estimation precision by considering the actual flux density in machine iron core.

4.2 Air gap magnetic field analysis

High order harmonics result in air gap magnetic flux density waveform distortion, which further leads to the eddy current induced in the rotor conductive component. Therefore, it is necessary to consider the air gap magnetic field distribution for HSPMMs. In order to have a deep understanding of machine air flux density distribution, analytical modelling is studied in this section.

(a) No load air gap magnetic field

The no load air gap magnetic field is a critical factor that decides permanent magnet (PM) machine output performance, and it is always desirable to obtain its exact flux density distribution for BLAC machines. The no load air gap flux density can normally be obtained by analytical method and FEM. The analytical method can predict the flux density waveform accurately and quickly, which shows its advantage in initial electrical machine design phase; while FEM is also available to accurately calculate the air gap flux density distribution. However, FEM requires machine modeling, meshing and other pre-processing procedures which are considered time consuming.

In this dissertation, the HSPMM is firstly analyzed using a slotless geometry model, with the air gap flux density $B_g(r,\theta)$ analysis for a slotless PM machine calculated using the method developed in [133] [134]. The relationship between the magnetic flux density $\vec{B}$ and the magnetic field intensity $\vec{H}$ for the machine air gap and rotor sleeve region is given by:

$$\vec{B}_1 = \mu_0 \vec{H}_1 \tag{4.11}$$

while in the permanent magnet region, it is expressed as:

$$\vec{B}_2 = \mu_0 \mu_r \vec{H}_2 + \mu_0 \vec{M} \tag{4.12}$$

where μ_0 and μ_r are the permeability of free space and the relative permeability of the permanent magnet, and $\vec{M}$ is the magnetization vector, which can be defined in polar coordinates as:

$$\vec{M} = M_r \vec{r} + M_\theta \vec{\theta} \tag{4.13}$$

where M_r and M_θ are the magnetization vector in radial and tangential directions respectively, which can be expanded as Fourier series:

$$M_r = \sum_{n=1,3,5\cdots}^{\infty} M_{rn} \cos(np\theta) \tag{4.14}$$

$$M_\theta = \sum_{n=1,3,5\cdots}^{\infty} M_{\theta n} \sin(np\theta) \tag{4.15}$$

p is the number of pole pairs and θ is the angular displacement from the magnet pole centre axis. As the PMs in HSPMM are radially magnetized with respect to the centre of the machine geometry, hence, the Fourier coefficients are derived as:

$$M_{rn} = \frac{4B_r}{\mu_0 n\pi} \sin(0.5n\pi\alpha_m) \tag{4.16}$$

$$M_{\theta n} = 0 \tag{4.17}$$

where B_r is the PM remanent flux density and α_m is the pole arc to pole pitch factor. The scalar magnetic potential in the air gap and sleeve region (φ_A) is governed by Laplace's equation, which can be expressed in polar cylindrical coordinates as:

$$\frac{\partial^2 \varphi_A}{\partial r^2} + \frac{1}{r}\frac{\partial \varphi_A}{\partial r} + \frac{1}{r^2}\frac{\partial^2 \varphi_A}{\partial \theta^2} = 0 \tag{4.18}$$

while the scalar magnetic potential in the permanent magnet (φ_M) is governed by Poisson's equation which can be expressed as:

$$\frac{\partial^2 \varphi_M}{\partial r^2} + \frac{1}{r}\frac{\partial \varphi_A}{\partial r} + \frac{1}{r^2}\frac{\partial^2 \varphi_M}{\partial \theta^2} = \frac{1}{\mu_r} div \vec{M} = \frac{1}{\mu_r} \sum_{n=1,3,5....}^{\infty} \frac{1}{r} M_n \cos(np\theta) \tag{4.19}$$

where

$$M_n = M_{rn} + npM_{\theta n} \tag{4.20}$$

The radial and tangential components of the magnetic field intensity H_r and H_θ can be expressed through the scalar magnetic potential as:

$$H_r = -\frac{\partial \varphi}{\partial r} \tag{4.21}$$

$$H_\theta = -\frac{1}{r}\frac{\partial \varphi}{\partial \theta} \tag{4.22}$$

The general solution for the Laplace equation and Possion equation is obtained by the variable separation method, which is represented with an infinite series as follows:

$$\varphi_A(r,\theta) = \sum_{n=1,3,5....}^{\infty} (A_n r^{np} + B_n r^{-np}) * \cos(np\theta) \tag{4.23}$$

in the air gap, while

$$\varphi_M(r,\theta) = \sum_{n=1,3,5....}^{\infty} (C_n r^{np} + D_n r^{-np}) * \cos(np\theta) + \sum_{n=1,3,5....}^{\infty} \frac{M_n r}{\mu_r \left[1-(np)^2\right]} \cos(np\theta) \tag{4.24}$$

$$(np \neq 1)$$

$$\varphi_M(r,\theta) = (C_{n1}r + D_{n1}r^{-1})\cos(\theta) + \frac{0.5M_1}{\mu_r} r\ln r\cos(\theta) \quad (np=1) \tag{4.25}$$

in the magnets. Here, A_n, B_n, C_n, D_n, C_{n1}, D_{n1} are determined by the application of boundary conditions. Then the magnetic flux density in the radial and tangential components in the air gap region can be expressed as:

$$B_r = \sum_{n=1,3,5....}^{\infty} K(n) f_1(r)\cos(np\theta) \tag{4.26}$$

$$B_\theta = \sum_{n=1,3,5....}^{\infty} K(n) f_2(r)\sin(np\theta) \tag{4.27}$$

For np=1,

$$K(n) = \frac{\mu_0 M_n}{2\mu_r} \frac{Q_n(\frac{R_m}{R_s})^2 - Q_n(\frac{R_r}{R_s})^2 + (\frac{R_r}{R_s})^2 \ln(\frac{R_m}{R_r})^2}{\frac{\mu_r+1}{\mu_r}\left[1-(\frac{R_r}{R_s})^2\right] - \frac{\mu_r-1}{\mu_r}\left[(\frac{R_m}{R_s})^2 - (\frac{R_r}{R_m})^2\right]} \tag{4.28}$$

$$f_1(r) = 1 + (\frac{R_s}{r})^2 \tag{4.29}$$

$$f_2(r) = -1 + (\frac{R_s}{r})^2 \tag{4.30}$$

while for $np \neq 1$, K(n), $f_1(r)$ and $f_2(r)$ are based on the machine structure. The increase of the internal rotor machine whose parameters satisfy the constraints $R_s > R_m > R_r$, (R_s, R_m and R_r are the stator bore radius, magnet outer radius and rotor core outer diameter), then

$$K(n) = \frac{\mu_0 M_n}{\mu_r} \frac{np}{(np)^2-1} \frac{(Q_n-1) + 2(\frac{R_r}{R_m})^{np+1} - (Q_n+1)(\frac{R_r}{R_m})^{2np}}{\frac{\mu_r+1}{\mu_r}\left[1-(\frac{R_r}{R_s})^{2np}\right] - \frac{\mu_r-1}{\mu_r}\left[(\frac{R_m}{R_s})^{2np} - (\frac{R_r}{R_m})^{2np}\right]} \tag{4.31}$$

$$f_1(r) = (\frac{r}{R_s})^{np-1}(\frac{R_m}{R_s})^{np+1} + (\frac{R_m}{r})^{np+1} \tag{4.32}$$

$$f_2(r) = -(\frac{r}{R_s})^{np-1}(\frac{R_m}{R_s})^{np+1} + (\frac{R_m}{r})^{np+1} \tag{4.33}$$

The parameter Q_n is based on the magnets magnetization formats: it is equal to np if the machine magnets are magnetized in the radial direction.

Based on air gap magnetic field modeling, the HSPMM air gap flux density distribution, without considering the effects of stator slotting, can be analytically predicted. Machine radial and tangential air gap flux densities for one mechanical angular period are shown in Fig.4.6:

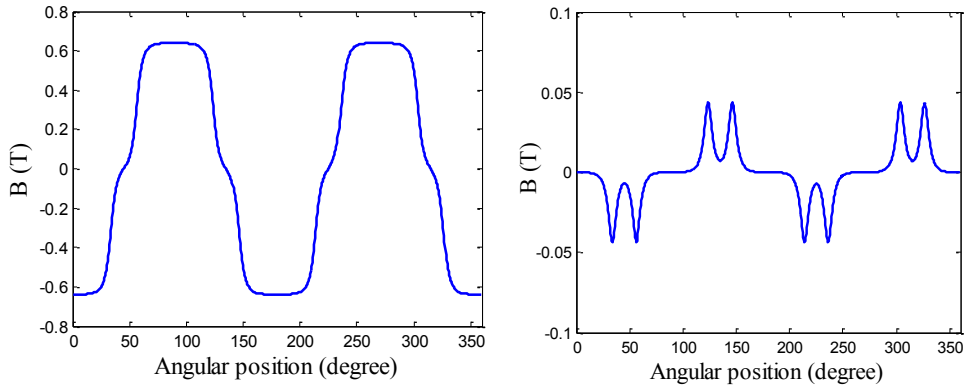

(a) Radial component (b) Tangential

Fig. 4.6 Air gap flux density

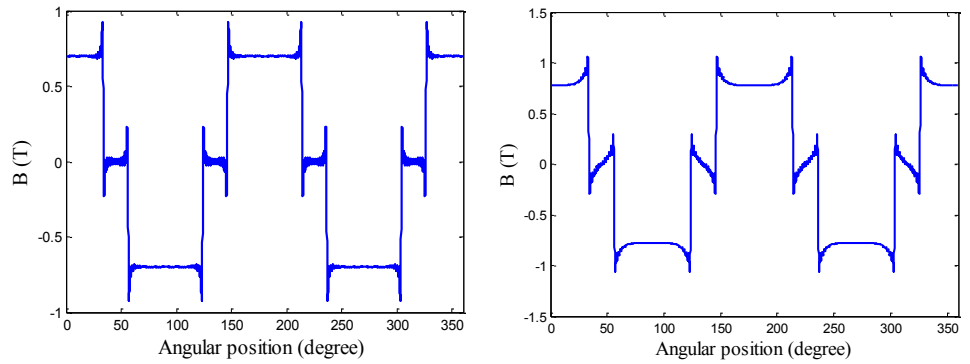

(a) PM top (72mm) (b) PM bottom (65mm)

Fig. 4.7 Permanent magnet flux density

The flux density in the machine magnet region with the slotting effect neglected is presented in [134]. The radial flux density distributions of the top and bottom machine magnet regions are shown in Fig.4.7. It is found that the harmonics contributing to the flux density of the air gap and magnet region are all odd order ones.

Machine stator slotting causes air gap permeance variation, and its effect on permeance can be represented by introducing an air gap permeance distribution function $\Lambda(r,\theta)$. Therefore, the air gap flux density distribution in a slotless permanent magnet machine can be modified to cater for the practical slotted permanent magnet machine by multiplying it by the air gap permeance distribution function. The $\Lambda(r,\theta)$ distribution in the rotor reference frame can be calculated by the conformal mapping method, which transforms the complex stator slotted geometry model into the slotless one. It is defined as:

$$\Lambda(r,\theta) = \Lambda_0(r) + \sum_{n=1}^{\infty} \Lambda_n(r)\cos(nQ_s(\theta - \omega_r t)) \tag{4.34}$$

where Q_s is the permanent magnet machine stator slot number, and ω_r is the rotor angular speed. The permeance function coefficients $\Lambda_0(r)$ and $\Lambda_n(r)$ can be obtained as [135]:

$$\Lambda_0(r) = \frac{1}{k_c}(1 - 1.6\beta\frac{b_0}{t}) \tag{4.35}$$

$$\Lambda_n(r) = -\beta(r)\frac{4}{n\pi}[0.5 + \frac{(n\frac{b_0}{t})^2}{0.78125 - 2(n\frac{b_0}{t})^2}]\sin(1.6n\pi\frac{b_0}{t}) \tag{4.36}$$

where b_0 is the slot opening width, t is the tooth pitch and k_c is the Carter coefficient for effective air gap length defined as:

$$k_c = \frac{t}{t - \gamma g'} \tag{4.37}$$

where $t=\frac{2\pi R_s}{Q_s}$, $g'=g+\frac{h_m}{\mu_r}$, g is the original air gap length, h_m is the magnet thickness,

$$\gamma=\frac{4}{\pi}(\frac{b_0}{2g'}\tan^{-1}(\frac{b_0}{2g'})-\ln\sqrt{1+(\frac{b_0}{2g'})^2}) \tag{4.38}$$

and

$$\beta(r)=0.5*(1-\frac{1}{\sqrt{1+(\frac{b_0}{2g'})^2(1+x^2)}}) \tag{4.39}$$

The coefficient x can be obtained by solving equation:

$$y\frac{\pi}{b_0}=\frac{1}{2}\ln(\frac{\sqrt{a^2+x^2}+x}{\sqrt{a^2-x^2}-x})+\frac{2g'}{b_0}\tan^{-1}\frac{2g'}{b_0}\frac{x}{\sqrt{a^2+x^2}} \tag{4.40}$$

in which $a^2=1+(\frac{2g'}{b_0})^2$, and $y=r-R_s+g'$ for an internal rotor machine.

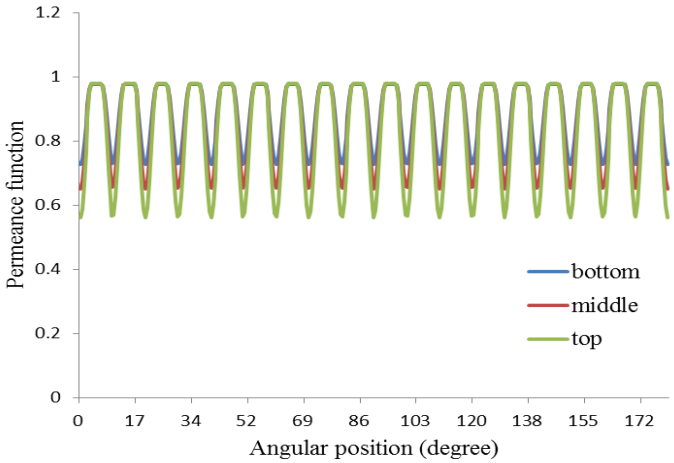

Fig.4.8 Permeance function

For the researched 36 slot 4 pole HSPMM, the permeance functions for the air gap region (bottom side near the rotor, middle of the air gap and top side near the stator, respectively) for one mechanical pole pair period are displayed in Fig. 4.8. Then the stator slotted permanent magnet machine radial flux density distribution $B_r(r,\theta)$ can be obtained using the permeance function as:

$$B_r(r,\theta) = B_{r\_slotless}(r,\theta) * \Lambda(r,\theta - w_r t) \tag{4.41}$$

where $B_{r\_slotless}$ is the air gap flux density distribution for the slotless machine. The HSPMM air gap flux density distribution and FFT analysis results for the machine air gap (just above the rotor sleeve) for one pole pair are calculated by both the analytical and FEM approaches, respectively. The results are shown in Fig. 4.9: good agreement is achieved between the analytical and FEM results. It is noticeable that for the machine expressed in rotor reference frame, the slot permeance function varies with rotor position; hence, the slotting effect causes harmonics which rotate asynchronously to the rotor; accordingly, eddy current is induced in the machine rotor.

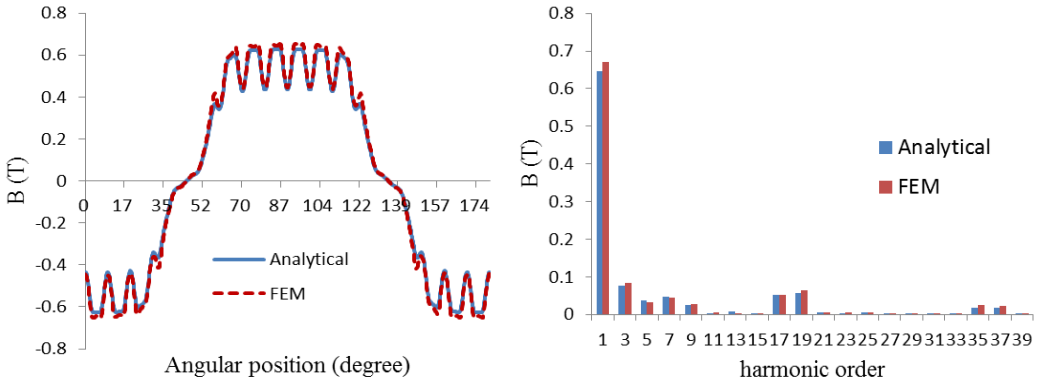

(a) Waveform (b) FFT analysis

Fig. 4.9 Air gap flux density FFT analysis

(b) Air gap magnetic flux density due to the armature

Reference [136] illustrates the analytical model for the machine armature reaction field based on the assumption that machine stator ampere-conductors are represented by equivalent current sheets with infinitesimal thickness distributed over the slot openings. The equivalent current sheets, which represent overlapping windings, can be derived by Fourier series expression as follows:

$$J = \sum_{v=-\infty}^{+\infty} \sum_{u=1}^{\infty} J_{uv} \sin(up\omega_r t \pm v\alpha + \theta_u) \tag{4.42}$$

$$J_{uv} = \frac{3NI_u}{\pi R_s} K_{slv} K_{pv} K_{dv} \tag{4.43}$$

where u is the order of the time harmonic in the current waveform, and v is the space harmonic order which is expressed as:

$$v = p(6c - \{\pm u\}) \qquad \text{c=0, } \pm 1, \pm 2 \ldots\ldots \tag{4.44}$$

α is the rotor position, ω_r is the rotor speed, θ_u is the corresponding phase current angle; N is the winding turns in series per phase and I_u is the u^{th} order current harmonic amplitude. K_{slv}, K_{pv} and K_{dv} are the slot opening factor, winding pitch factor and winding distribution factor, respectively. They are as defined as:

$$K_{slv} = \frac{\sin(0.5v\theta_s\pi)}{0.5v\theta_s\pi} \qquad \theta_s = \frac{b_s}{2\pi R_s} \tag{4.45}$$

$$K_{pv} = \sin(\frac{\pi Y_p}{2\tau}) \qquad \tau = \frac{Q}{2p} \tag{4.46}$$

$$K_{dv} = \frac{\sin(0.5vq\alpha_1)}{q\sin(0.5v\alpha_1)} \qquad \alpha_1 = \frac{2\pi}{Q} \tag{4.47}$$

where b_s is the slot opening width; Y_p is the winding coil pitch; q is the slot number per pole per phase and Q is the slot number. By Laplace's equation in polar coordinates, as given (4.13), the radial flux density due to the armature can be derived as:

$$B_{r\_arm} = \pm\mu_0 \sum_{v=-\infty}^{v=\infty}\sum_{u=1}^{\infty} \frac{J_{uv} R_s^{1-v}}{\left[(\frac{R_r}{R_s})^{2v} - 1\right]} [r^{v-1} + R_r^{2v} r^{-v-1}] \cos(up\omega_r t \pm v\theta_r \pm v\omega_r t + \theta_u) \tag{4.48}$$

Fig 4.10 shows the HSPMM air gap flux density (just above the rotor sleeve) due to the armature reaction and the corresponding FFT analysis results. The flux density fundamental induced by the armature is lower than the fundamental by the PM, in order to avoid PM demagnetization. The fundamental rotates at the machine synchronous speed; hence, it is stationary with respect to the rotor side. The high order harmonics are the 6n-1 or 6n+1 components (n=1, 2,…); these rotate at 6n

times the synchronous speed from the perspective of the rotor, which induces rotor eddy current losses.

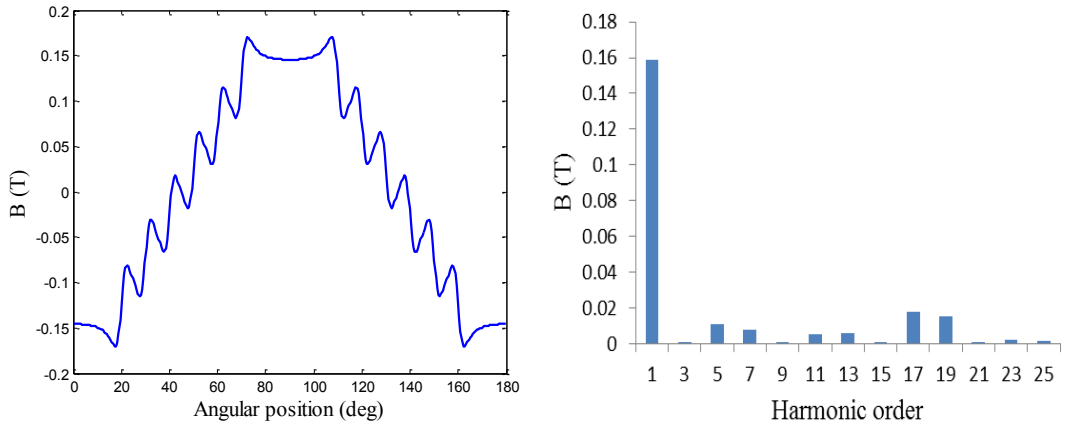

(a) Flux density waveform (b) FFT

Fig. 4.10. Flux density waveform with FFT analysis

4.3 Rotor eddy current loss estimation method

For conventional speed machines, rotor eddy current losses are not significant and can be neglected; however, in HSPMM they increase dramatically with machine frequency, as both the frequency and amplitude of the high order harmonic components on the rotor are obviously enhanced. This machine rotor eddy current loss is a consequence of: the stator slotting effect as this gives rise to variation in the air gap permeance, which increases the spatial harmonic components in the air gap; the stator winding spatial un-sinusoidal distribution also contributes to rotor eddy current loss due to high order components. In addition, electrical machines are commonly powered by inverters, hence, the stator winding current is not an ideal sinusoidal waveform and hence a source of high order temporal harmonics. Rotor eddy current losses directly heat the rotor and may lead to the rotor overheating and damaging the permanent magnets in the machine.

In polar coordinates, the HSPMM rotor eddy current density for PMs or the rotor sleeve can be estimated as:

$$J_z(r,\theta,t) = -\frac{1}{\rho}\frac{\partial A_z(r,\theta,t)}{\partial t} + C(t) \tag{4.49}$$

where ρ is the electrical resistivity; A_z is the magnetic potential; $C(t)$ is a time-dependent function that imposes a zero net current through the magnet and sleeve cross section. If the induced eddy current effects on the magnetic field are neglected, the Laplace equation is satisfied as:

$$\nabla^2 A = 0 \tag{4.50}$$

Then the eddy current loss for the PMs can be obtained as:

$$P_{eddy} = 2p\frac{\omega_r}{2\pi}\int_0^{l_a}\int_0^{\frac{2\pi}{\omega_r}}\int_{-\frac{\alpha_p}{2}}^{\frac{\alpha_p}{2}}\int_{R_r}^{R_m}\rho J_z^2 r dr d\theta_r dt dl \tag{4.51}$$

where p is the pole pair number; l_a is the rotor stack axial length, ω_r is the rotor speed, α_p is the magnet radian angle, R_r and R_m are the PM inner radius and outer radius, respectively. Sleeve eddy current loss can also be obtained using the same method. In this study, 2D time stepping FEM is utilized for HSPMM eddy current loss research, thus the rotor eddy current loss in one electrical period can be calculated as [137]:

$$P_{eddy} = \frac{1}{T_e}\int_{Te}\sum_{i=1}^{k} J_{ele}^2 \Delta_e \sigma^{-1} l_a dt \tag{4.52}$$

where T_e is the cycle time; J_{ele} is the current density in each element; Δ_e is the corresponding element area and σ is the conductivity of the eddy current region.

4.3.1 Effects of rotor sleeve conductivity and thickness

The rotor sleeve is used to protect the surface-mounted PMs against the large centrifugal force of high speed operation; its characteristics also have a significant effect on machine electromagnetic performance. The commonly used rotor sleeve materials can be classified as either metal or non-metal ones. A metal sleeve has high electrical conductivity and results in large machine eddy current losses. However, the metal sleeve also has high thermal conductivity which assists with rotor heat dissipation. For non-metal sleeves, both electrical and thermal conductivity are lower; hence eddy current losses in the sleeve are lower, but the capacity for thermal dissipation is also lower. Based on equation (4.52), it can be concluded that machine rotor eddy current loss depends on material conductivity, eddy current density, the

region where the eddy current is distributed and the rotor length. Rotor sleeve conductivity variation impacts not only the sleeve eddy current density amplitude, but also its distribution over the whole rotor region. Fig 4.11 compares the rotor eddy current density distribution for three sleeve materials: carbon fiber (conductivity: 2.2×10^4 S/m), Ti alloy (5.05×10^5 S/m) and copper (5.98×10^7 S/m) for HSPMM at rated speed with rated load:

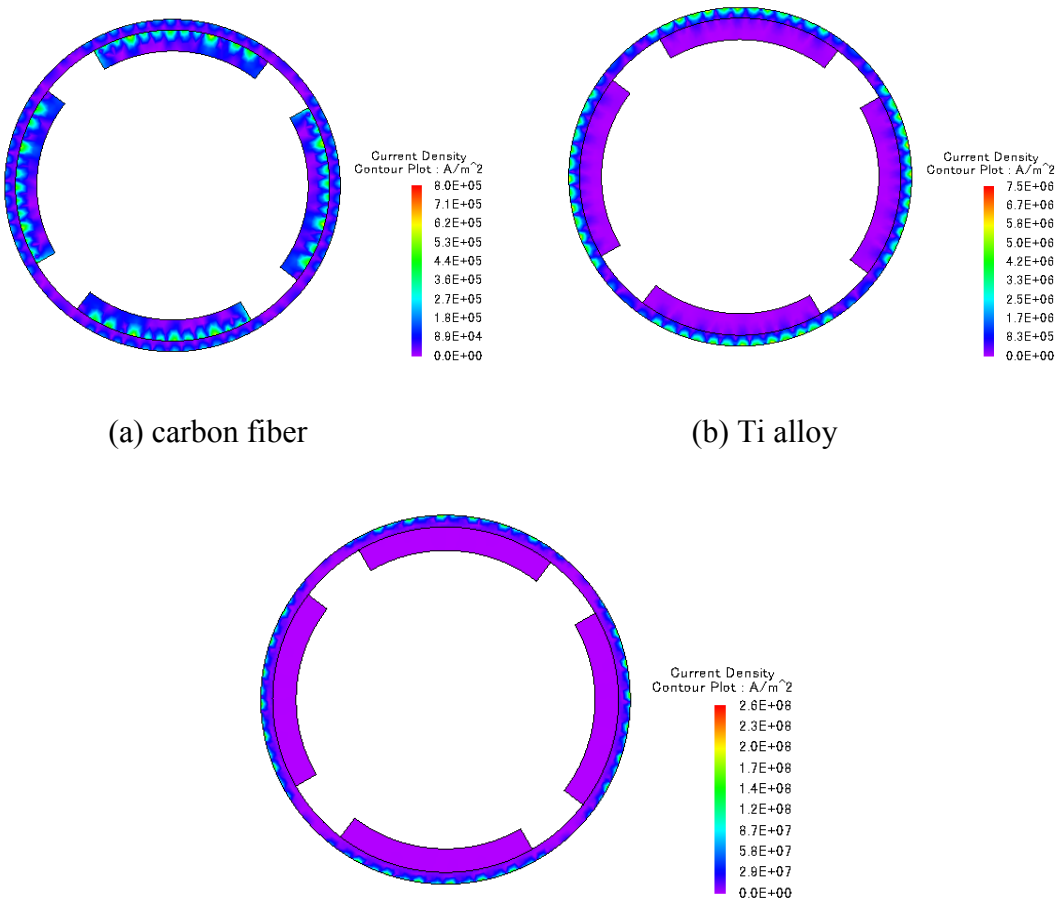

(a) carbon fiber (b) Ti alloy

(c) copper

Fig. 4.11 Eddy current density distribution under different sleeve materials.

As can be seen, the eddy current density is distributed on both the rotor sleeve and PMs when carbon fiber is used as the rotor sleeve; this is due to the fact that PM conductivity (625000 S/m) is higher than carbon fiber, and hence the sleeve cannot effectively shield the PMs from air gap flux harmonics; consequently, the largest current density of the whole rotor occurs in the PM region (max 7.63×10^5 A/m^2 in the PMs, max 3.26×10^5 A/m^2 in the sleeve); when the sleeve material conductivity increases (Ti alloy), the eddy current density is mainly distributed over the sleeve,

and the eddy current density in the PMs is effectively reduced; with the copper sleeve, the eddy current is mostly distributed on the sleeve surface, and the eddy current loss in the PMs is nearly zero. However, the eddy current density amplitude in the copper sleeve (2.47×10^8 A/m^2) is much higher than in its carbon fiber counterpart. This can be explained by the penetration depth h, which is defined as the depth that the electromagnetic intensity field extends inside the material. This reduces to 1/e of its original value at the material surface. The penetration depth h is given by:

$$h = \sqrt{\frac{2}{\omega\sigma\mu}} \tag{4.53}$$

where ω is the harmonic magnetic field angular frequency, σ is electrical conduction conductivity and μ is permeability. Penetration depth declines as material conductivity increases. Hence, for a high electrical conductivity (copper) sleeve, the penetration depth is small and the eddy current is only distributed over the copper sleeve surface. This shields the PMs from air gap harmonic magnetic field effects. For a low conductivity (carbon fiber) sleeve, the penetration depth is much larger and magnetic harmonic fields can penetrate into the PMs through the sleeve, hence the eddy current density is distributed throughout the rotor.

Table 4.5 shows eddy current loss against sleeve conductivity for a HSPMM operating at rated conditions. The eddy current loss in PMs declines with increasing sleeve conductivity, and it drops to nearly zero when the sleeve conductivity reaches 8×10^6 S/m. As for the rotor sleeve, when the sleeve conductivity increases from 5×10^3 S/m to 5×10^4 S/m, the sleeve eddy current loss grows 10 times from 27.5 W to 271.8 W, hence the eddy current loss rise is mainly due to increase in the sleeve conductivity; when the conductivity ranges from 5×10^5 S/m to 5×10^6 S/m, the sleeve eddy current loss only increases by a factor of 4.5, as the penetration depth reduces with increased sleeve conductivity and hence the eddy current cannot penetrate the whole sleeve. When the sleeve conductivity reaches 1×10^7 S/m, the sleeve eddy current loss exhibits a declining trend with sleeve conductivity. Under these conditions the rotor eddy current distribution region is limited on the sleeve surface, and the eddy current distribution area becomes the main factor impacting rotor eddy current loss.

Table 4.5 Eddy current loss against sleeve conductivity

Conductivity (S/m)	5×10^{3}	1×10^{4}	5×10^{4}	1×10^{5}	5×10^{5}	1×10^{6}
Sleeve (W)	27.5	54.9	271.8	537.3	2455.4	4408.1
PM (W)	31.1	31.0	30.1	29.2	23.5	17.9
Conductivity (S/m)	3×10^{6}	5×10^{6}	8×10^{6}	1×10^{7}	5×10^{7}	8×10^{7}
Sleeve (W)	9019.2	11036.2	12282.5	12621.0	11121.3	9969.3
PM (W)	6.3	2.5	0.8	0.4	0.2	0.4

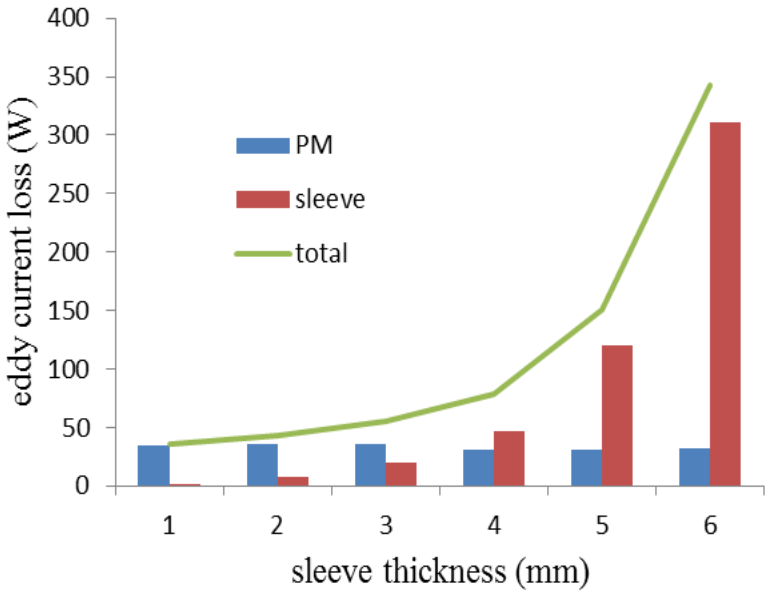

Fig 4.12 Eddy current loss with sleeve thickness.

Fig 4.12 presents the rotor eddy current loss variation with sleeve thickness for a HSPMM operating at rated conditions. In this study, carbon fiber is utilized as the rotor sleeve material, with the distance between the PM outer surface and the stator bore surface held a constant as the sleeve thickness varies. Machine air gap length is reduced with sleeve thickness increasing. It can be seen that PM eddy current loss decreases slightly as the sleeve thickness increases. Furthermore, it represents the major proportion of the total rotor eddy current loss if sleeve thickness does not exceeding 3mm. The PM eddy current loss varies slightly with sleeve thickness due

to the carbon fiber sleeve shielding effect. The sleeve eddy current loss rises dramatically with sleeve thickness as increasing sleeve thickness results in a larger rotor diameter and a smaller air gap length; This gives rise to sleeve eddy current loss, as well as the rotor total eddy current loss obviously. Therefore, the rotor sleeve has considerable influence on rotor eddy current loss, and it is advisable to reduce sleeve thickness in surface-mounted HSPMMs to decrease rotor eddy current loss, to the extent that mechanical design considerations permit.

4.3.2 PM loss reduction by composite rotor structure

As introduced in the previous section, high conductivity materials can shield the PMs and decrease PM eddy current loss. Therefore, a composite rotor structure with copper shielding placed between the rotor sleeve and the PMs, as shown in Fig 4.13, is studied with two types of sleeve material (stainless steel and carbon fiber) for a HSPMM operating at rated speed with rated load. The eddy current density distributions for the composite rotor structure are shown in Fig 4.14, while Table 4.6 presents the rotor eddy current loss for a range of copper shielding thicknesses.

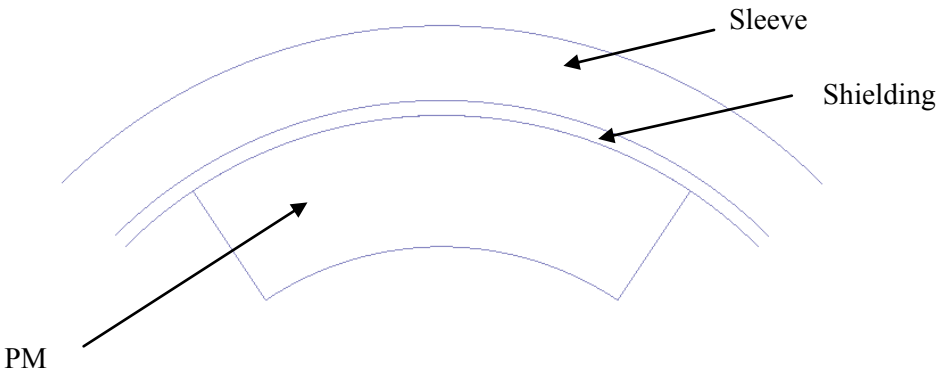

Fig. 4.13. Composite rotor structure

It can be concluded from Fig 4.14, that adding copper shielding clearly impacts the eddy current distribution on the rotor. From Table 4.6, it is learned that for the carbon fiber sleeve, eddy current loss in both the PM and the sleeve is effectively reduced by increasing the copper shielding thickness. This is because the eddy current density declines in both sleeve and PMs with the added copper shielding as shown in Fig 4.14 (a). However, the eddy current in the copper shielding itself becomes much higher due to its high conductivity, which gives rise to rotor overall eddy current loss. Indeed the copper shielding eddy current loss becomes the major component of the overall rotor eddy current loss. Hence, with the carbon fiber sleeve

the total rotor eddy current loss is higher than without copper shielding. In the case of the rotor with stainless steel sleeve, the added copper shielding in the composite rotor structure also has the advantage of decreasing the eddy current loss in both the PMs and sleeve. In addition, the machine rotor eddy current loss is mainly due to the stainless steel sleeve. Though it gives rise to copper shielding eddy current loss, machine overall rotor eddy current loss shows a declining trend with increasing copper shield thickness. So the effect from the added shielding on machine overall rotor eddy current loss is dependent on machine sleeve material utilized.

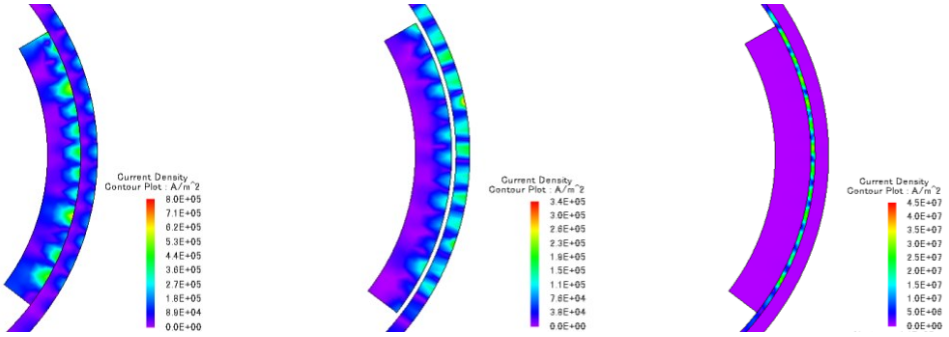

no copper shielding composite structure

(a) carbon fiber sleeve

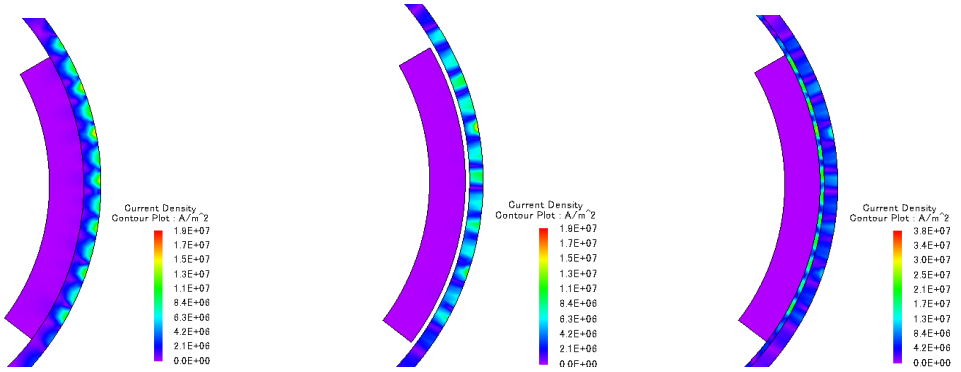

no copper shielding composite structure

(b) stainless steel sleeve

Fig 4.14 Eddy current distribution for (a) carbon fiber sleeve; (b) stainless sleeve composite rotor structures, with and without copper shielding.

Table 4.6 Eddy current loss for various composite rotor structures

Shielding thickness (mm)	Sleeve (W)		PM (W)		Shield (W)		Total (W)	
	Carbon fiber	Stainless steel	Carbon fiber	Stainless steel	Carbon fiber	Stainless steel	Carbon fiber	Stainless steel
0	120.2	5379.2	30.7	16.5	0	0	151.0	5395.7
0.1	115.7	5263.5	17.7	9.2	166.6	83.9	300.0	5356.5
0.2	113.3	5198.8	11.1	5.9	223.4	118.3	347.8	5323.0
0.3	111.5	5146.6	7.2	4.0	243.2	133.4	361.9	5284.0
0.4	109.9	5102.1	4.8	2.7	249.3	140.7	364.0	5245.5
0.5	108.6	5062.3	3.3	1.9	253.3	146.2	365.2	5210.5
0.6	107.3	5024.3	2.4	1.5	256.8	151.1	366.6	5176.8
0.8	105.0	4958.4	1.4	0.91	278.9	167.6	385.3	5126.9
1.0	100.8	4826.8	1.4	0.9	348.4	208.2	450.7	5035.9
1.2	95.8	4673.8	2.0	1.2	475.1	278.1	572.9	4953.1

4.3.3 Effects of air gap length

The air gap length between the stator and rotor is a critical design parameter for machine output performance, as the mechanical and electrical energy conversion is progressed through the machine air gap region. Permanent magnet machine rotor eddy current losses are also closely dependent on the air gap length, as the magnetic field harmonic components and permeance can be greatly influenced by the size of the air gap. In this study, carbon fibre is chosen as the HSPMM rotor sleeve material, and the effects of air gap length on HSPMM eddy current losses are investigated by FEM. In addition, machine rotor PM thickness is also adjusted to maintain the same output torque as the original machine during air gap length variation. Fig 4.15 shows the relationship between machine air gap length and PM thickness under these

conditions. As can be seen the PM thickness has to be increased as the air gap length is increased to meet the torque specification. The air gap length variation directly effects the magnetic flux density harmonics of the HSPMM rotor. Fig. 4.16 compares the magnetic flux density waveforms on the surfaces of the rotor sleeve and PM for HSPMM at no load for several air gap lengths. It can be observed that fluctuations (or ripples) in the flux density waveforms in both the sleeve and PM are alleviated as the air gap length is increased. Therefore, enlarging air gap length is beneficial to reducing the ripple in the machine rotor magnetic flux density waveform.

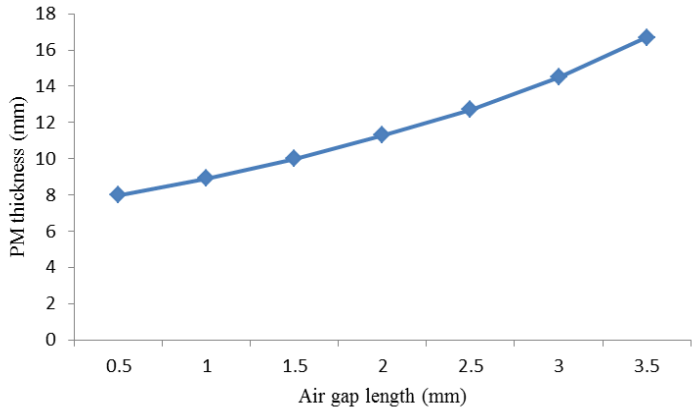

Fig 4.15 PM thickness with air gap length

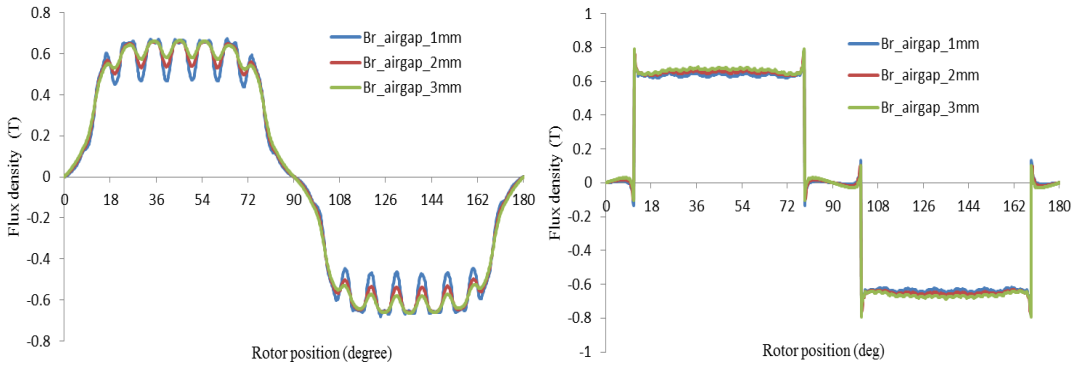

(a) Sleeve surface (a) PM surface

Fig.4.16 Flux density on the sleeve and PM surface with air gap length.

Fig. 4.17 displays the rotor sleeve and PM eddy current losses as a function of air gap length for a HSPMM operating at rated speed with no load and rated load, respectively. This highlights that air gap length has a significant impact on machine rotor eddy current loss, with rotor eddy current losses dramatically decreasing, as the

air gap increases, especially those losses occurring in the carbon fibre sleeve. Therefore, it can be concluded that although PM thickness has to be increased to maintain machine output torque, enlarging machine air gap length is an effective method of reducing rotor eddy current loss in HSPMMs. This is primarily due to rotor magnetic flux density harmonic component amplitudes declining with increasing air gap length. More PM material is required in HSPMMs to maintain machine output torque performance when larger air gaps are used. This also increases machine manufacture cost, hence a balance has to be struck.

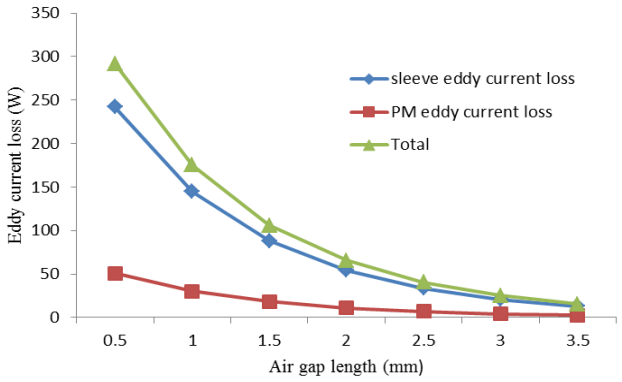

(a) No load

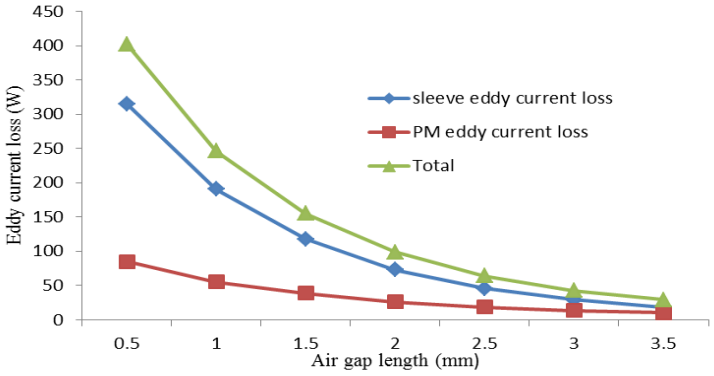

(b) Rated load

Fig.4.17 Eddy current loss as a function of air gap length.

4.3.4 Effects of stator slot opening width

The stator slot structure changes the electrical machine air gap permeance distribution, causes distortion in the air gap flux density waveform and induces rotor harmonic components; then the harmonics due to the stator slots lead to rotor eddy current losses. Fig. 4.18 displays flux density waveforms on the rotor sleeve surface

and PM surface for one pole pair for several stator slot opening widths. It can be observed that the stator slot opening width has an obvious influence on magnetic density waveforms: the flux density waveform is nearly flat when the slot opening is 1 mm, while ripples in the waveforms become severe (especially on the sleeve side) when the stator slot opening width is increased to 9 mm.

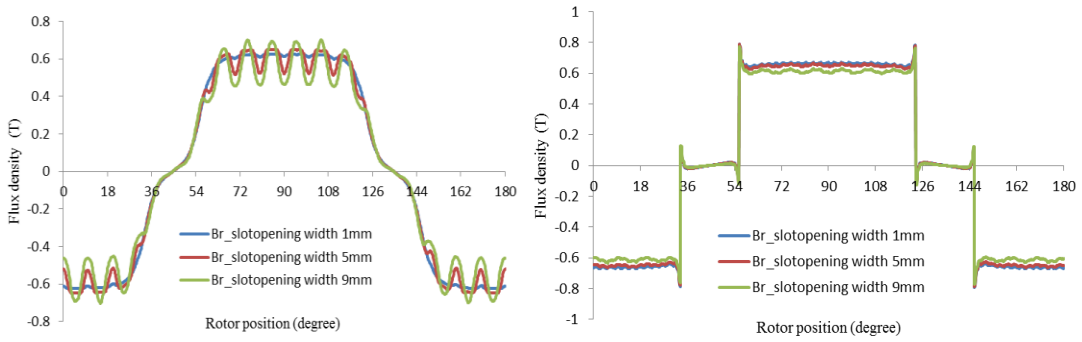

(a) sleeve (b) PM

Fig.4.18 Flux density on the sleeve and PM surface under different slot opening width

Fig. 4.19 displays rotor eddy current loss as a function of the stator slot opening width for a HSPMM operating at no load and rated load, respectively. It can be concluded that as the slot opening width increases, rotor total eddy current loss becomes more significant, especially when the slot opening width exceeds 3 mm. In addition, eddy current loss in the sleeve exhibits a dramatic raising trend and contributes most of the machine's rotor eddy current loss. The rising trend in PM eddy current loss is much less due to the magnetic shielding effects of the rotor sleeve.

Therefore, it is beneficial to reduce HSPMM stator slot opening width in order to minimize rotor eddy current losses. However, very small stator slot opening widths may create difficulties for winding assembly during machine manufacture. Although slotless structures have also been employed in permanent magnet machines, it is still not an applicable design scheme for large power HSPMMs due to its poorer electromagnetic performance, higher leakage flux and significant torque reduction effect compared to open-slot or semi-closed slot machines.

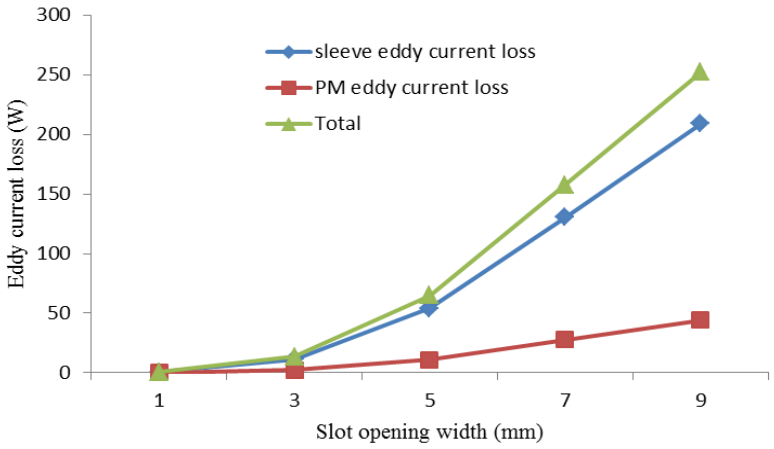

(a) No load

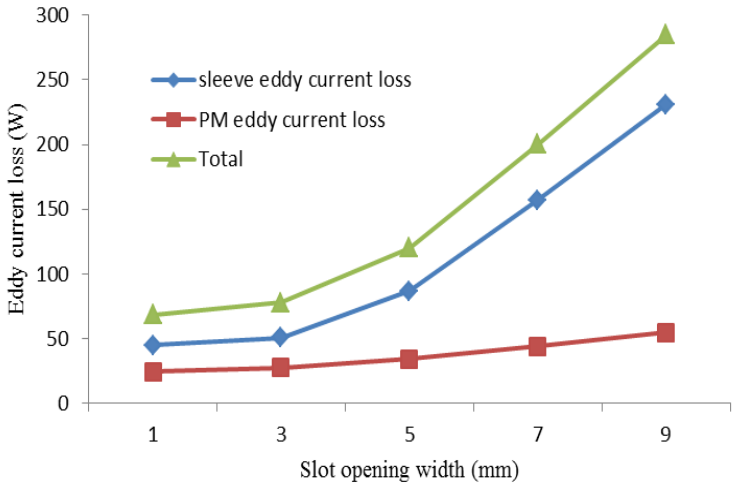

(b) Rated load

Fig 4.19. Eddy current loss with slot opening width

4.3.5 PM bevelling for rotor eddy current loss reduction

Rectangular-edged PM bevelling can be employed as a method to change the magnetic field of the machine, providing a further means of influencing HSPMM rotor eddy current loss. PM bevelling angle α is defined as shown in Fig 4.20.

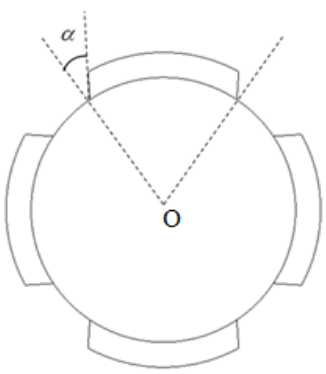

Fig 4.20. Rotor bevelling angle.

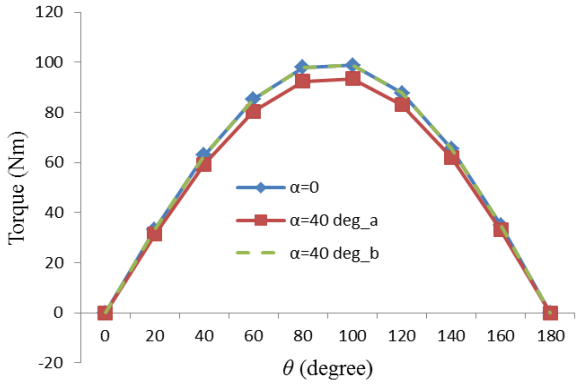

Fig 4.21. Power angle - torque characteristic for α=0, α=40 deg.

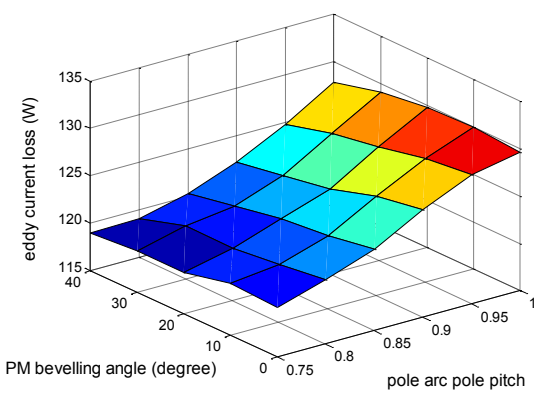

(a) Sleeve

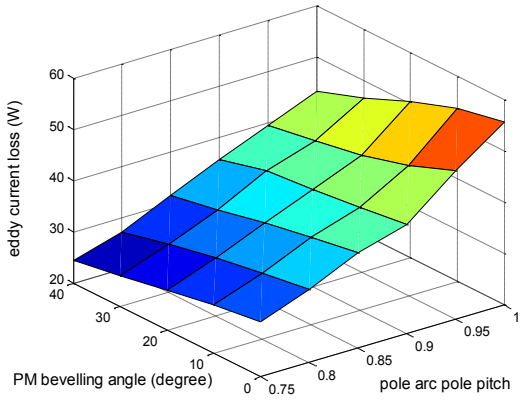

(b) PM

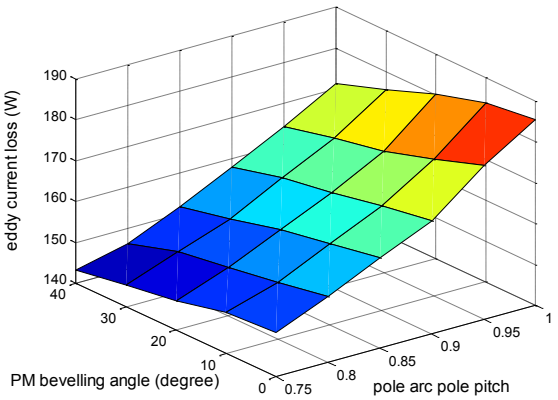

(c) Total

Fig. 4.22. Eddy current loss as a function of PM bevelling angle and pole arc pole pitch.

To consider the effect of PM bevelling on HSPMM output torque performance, the

current power angle (θ)-torque characteristic curve for a machine with rectangular-edged PM (i.e. α =0) is shown in Fig 4.21, while the same curve for a machine with 40^o PM bevelling angle (labelled as α=40 deg_a in the plot) is also presented. The volume of PM used by the rotor declines by 10% with a 40^o PM bevelling angle; while the machine maximum torque only drops by 5.4%. Hence, the contribution to machine output torque by the bevelled PM edge region is less than the other PM region. To maintain the same machine output torque, PM thickness has to be slightly adjusted to compensate for the impact of PM bevelling in Fig. 4.21, while the machine air gap length, sleeve outer diameter and sleeve thickness are all maintained at the same values. As illustrated in Fig 4.21 (plot α=40 deg_b) thickness compensation for bevelled PMs can effectively maintain machine output performance. It is also noted that for the HSPMM in this study, machine output torque cannot be maintained by increasing PM thickness if the bevelling angle α exceeding 40 deg.

Fig.4.22 presents the eddy current loss in both the PM and sleeve of a HSPMM as a function of pole arc pole pitch ratios and PM bevelling angles for a machine operating at rated load. It can be observed that rotor eddy current losses are reduced by the rotor PM bevelling method while maintaining the same output torque as a machine without PM bevelling across the full PM pole arc pole pitch range. Total rotor eddy current losses dropped nearly 20% from 185.4W to 171.3W for the machine with 40^o PM bevelling angle when the rotor pole arc pole pitch ratio is 1.0 (PM thickness is increased 0.21mm to maintain the same output torque). The main reduction in overall rotor eddy current loss is provided by PM: when the machine bevelling angle varies from 0^o to 40^o, PM eddy current losses decrease by 6.4 W for a rotor with 0.75-pole arc pole pitch, and 12.4 W for a rotor with 1.0- pole arc pole pitch configuration.

4.4 HSPMM rotor air frictional loss research

Due to the frictional effect between the machine air fluid and rotor surface, air frictional loss is a considerable proportion of the total machine losses. In addition, HSPMMs are constructed with a forced air cooling system. The forced cooling air also aggravates air molecule friction due to the effect of air viscosity. Conventionally, an electrical machine rotor is modelled as a cylinder with its air frictional loss

calculated as:

$$P_{af} = kC_f \pi \rho \omega^3 r^4 l \tag{4.54}$$

where k is the rotor surface roughness factor, ρ is the air gap density (kg/m^3), ω is the rotor angular speed (rad/s), and r and l are rotor radius and axial length, respectively. Then

$$C_f = \frac{0.0152}{\mathrm{Re}_\delta^{0.24}}[1 + (\frac{8}{7})^2 (\frac{\mathrm{Re}_a}{\mathrm{Re}_\delta})^2]^{0.38} \tag{4.55}$$

where

$$\mathrm{Re}_\delta = \frac{\rho \omega r \delta}{\mu_{air}} \tag{4.56}$$

$$\mathrm{Re}_a = \frac{\rho v_a 2\delta}{\mu_{air}} \tag{4.57}$$

δ is the air gap radial length, v_a is the cooling air speed and μ_{air} is the air motion viscosity.

HSPMM air frictional loss is relevant to several parameters relating to the machine air cooling structure: these parameters are determined based on the actual air fluid velocity distribution and spread factor in the machine air gap, which are difficult to calculate analytically. Therefore, a 3D fluid field model is built to predict HSPMM air frictional loss. The model can consider practical machine air gap structure and the complicated fluid distribution when the rotor is rotating at high speed. The slots of the designed HSPMM stator core are deeply grooved to create the space for the machine cooling air path. In the fluid field model, the machine air gap fluid should satisfy fluid viscosity theory, energy and momentum conservation theory. The K-ε equation model is adopted for turbulent flow calculation in fluid analysis. It satisfies fluid turbulence expressions, which are defined as:

$$\rho \frac{\partial k}{\partial t} + \rho \frac{\partial \mu_i k}{\partial t} = \frac{\partial}{\partial x_j}[(\mu + \frac{\mu_t}{\sigma_k}) \frac{\partial k}{\partial x_j}] + T_k - \rho \varepsilon \tag{4.58}$$

$$\rho\frac{\partial\varepsilon}{\partial t}+\rho\frac{\partial u_i\varepsilon}{\partial x_i}=\frac{\partial}{\partial x_j}[(\mu+\frac{\mu_t}{\sigma_\varepsilon})\frac{\partial\varepsilon}{\partial x_j}]+\frac{\varepsilon(C_{\varepsilon 1}T_k-C_{\varepsilon 2}\rho\varepsilon)}{k} \tag{4.59}$$

where k is the turbulence work energy, ε is the turbulence consuming ratio, T_k is the turbulence work energy generation due to the viscosity force; μ_t is the turbulence viscosity factor, and σ_k, σ_ε, $C_{\varepsilon 1}$ and $C_{\varepsilon 2}$ are constants, respectively.

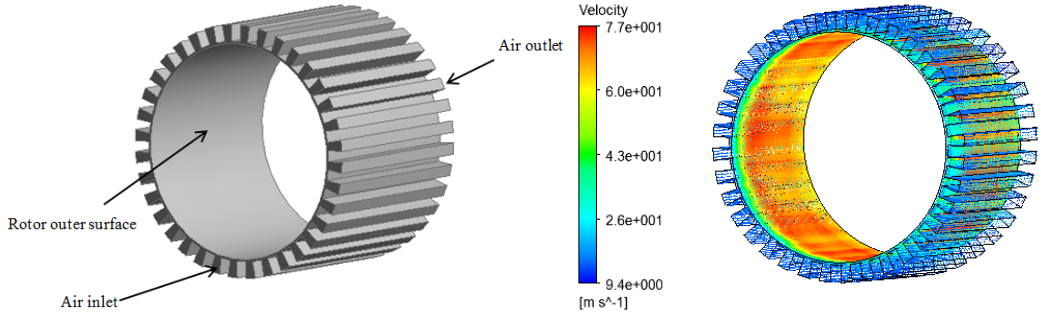

(a) windage loss model (b) velocity vector distribution

Fig. 4.23. Machine windage loss model and air fluid vector distribution.

The air frictional loss model is developed for HSPMM as shown in Fig 4.23 (a), with forced cooling air flowing into the machine from inlet to outlet. The rotor outer surface is defined as a rotational wall in the model to take the rotor motion effect into consideration. The air density is 1.29 kg/m^3, while the rotor surface roughness is 0.01 in the model. Then the machine air frictional loss can be calculated by the energy change between the model inlet side and outlet side based on the energy conservation principle. Fig 4.23 (b) displays the air fluid vector distribution result in the machine air gap when the machine rotor is at rated speed and the forced cooling air speed is 15 m/s. It can be seen that the air velocity near the rotor surface is higher than in the grooves due to the impact of rotor motion.

Fig. 4.24 (a) presents HSPMM air frictional loss as a function of rotor speed and surface roughness. It can be observed that machine air frictional loss increases dramatically with rotor speed: when the machine speed rises from 8000 rpm to 23000 rpm (nearly 3 times speed increasing), machine air frictional loss increases by a factor of almost 20 times. Machine air frictional loss also increases with the roughness of the rotor surface. Hence, it is beneficial to have a smooth rotor surface in a HSPMM to reduce air frictional loss. Fig. 4.24 (b) displays the HSPMM air

frictional loss with forced cooling air speed when the rotor is at rated speed. This shows that air frictional loss also increases with the forced cooling air speed. Thus, while the forced cooling air can remove the heat generated by the machine; it also gives rise to machine air frictional loss. As such forced cooling air speed for HSPMMs has to be selected balancing these two competing factors.

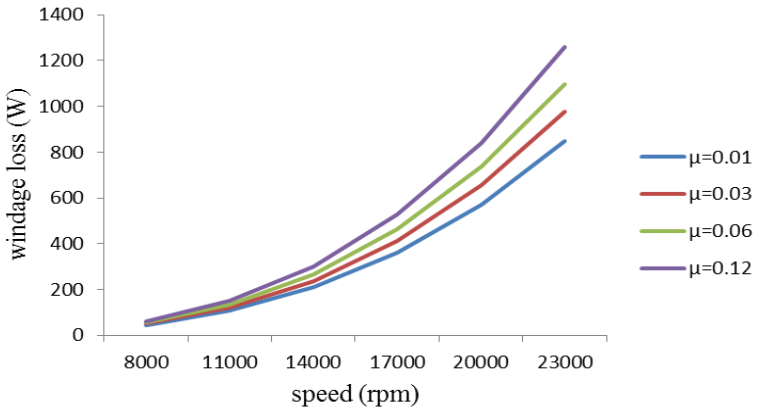

(a) Windage loss with different roughness as a function of speed of rotation.

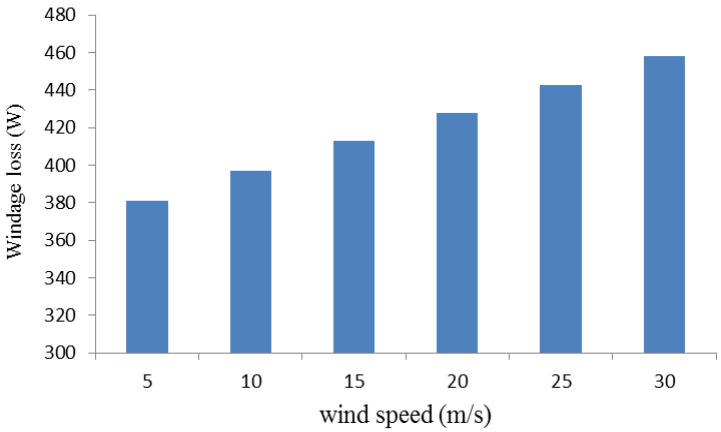

(b) Windage loss with different cooling air speeds.

Fig. 4.24 HSPMM windage loss calculation.

4.5 Conclusions

(1) HSPMM iron loss estimation is studied and researched in this chapter. The nature of magnetization in machine core regions is investigated using FEM, revealing that magnetization loci are different at different core locations; then machine iron loss is

calculated with an improved iron loss calculation method; the improved method is based on the machine core flux density waveform, which can take both rotational magnetic field and harmonic effects into consideration providing more precision.

(2) HSPMM air gap magnetic field distribution is calculated analytically, while the effectiveness of a machine FEM model has been verified by comparison.

(3) HSPMM rotor eddy current loss has been comprehensively studied. The impact of sleeve characteristics on rotor eddy current loss has been researched. It is found that as sleeve conductivity increases, rotor eddy current loss shows an initial rising trend and then a decline as rotor eddy current loss depends on both its amplitude and its distribution. A composite rotor structure is studied with different rotor sleeve materials for PM power loss minimization, while stator slotting length and air gap length are also studied to identify ways of decreasing machine rotor eddy current loss. PM beveling is proposed and is shown to perform effectively for rotor eddy current reduction while maintaining machine output torque.

(4) HSPMM air frictional loss is studied by fluid analysis: Air frictional loss is shown to dramatically increase with rotor speed and to a lesser extent with cooling air speed. It is therefore beneficial to utilize a smooth rotor surface and to choose a reasonable forced air cooling speed.

Chapter 5
High speed permanent magnet machine temperature calculation and thermal analysis

Electrical machine power losses act as heat sources that give rise to the machine operational temperature; in addition, the temperature distribution in electrical machines is normally uneven, as heat generation and thermal dissipation in the machine are complicated processes. Controlling temperature rise is critical to ensure reliable machine operation and to prevent overheating problems from arising, especially in HSPMMs. This is due to the fact that power loss density is higher in HSPMM than in conventional speed machines for the same power rating. Moreover, it is acknowledged that PM material characteristics are highly dependent on their

operating temperature. The limited thermal dissipation area of HSPMM rotors also causes difficulty with regard to effective machine cooling. Hence, rotor PMs may get irreversibly demagnetized due to rotor over-heating, which seriously and permanently degrades machine performance. Therefore, it is advisable to design an effective machine cooling system to improve HSPMM heat dissipation capability. Based on thermal transfer theory and fluid mechanics theory, machine heat transfer phenomenon are investigated comprehensively in this chapter. A HSPMM fluid-thermal coupling calculation model is developed with reasonable boundary conditions applied; then the HSPMM temperature distribution is obtained based on the power losses researched in the previous chapters.

5.1 HSPMM thermal calculation methods

Temperature calculation is an important research topic in electrical machine engineering, especially for machines with high power density such as high speed machines. Determining the temperature field in electrical machines is also a complicated topic, which depends on thermodynamics, fluid mechanics and machine manufacturing technology. The routine thermal circuit method can be applied for machine temperature calculations, as this method simplifies the electrical machine components into thermal resistivity to yield an equivalent thermal circuit with heat sources; then machine thermal variation is calculated based on the thermal circuit, which can be analysed using standard electrical circuit techniques. The advantage of the routine thermal circuit method comes from its ease of application in engineering, allowing electrical machine temperature results to be obtained rapidly. As for practical electrical machines, the structure and shape of their components makes determining thermal resistance a complex task; Moreover, the thermal resistivity of machine components is difficult to predict precisely and requires several experiential assumptions. Hence, the machine temperature calculation cannot be very accurate when using the routine thermal circuit method. In recent years, the based fluid-solid coupling calculation method (Computational Fluid Dynamics (CFD)) has been utilized to solve the electrical machine temperature field problem. The CFD fluid-solid coupling calculation is based on FEM analysis, which is suitable for domains with complex shapes and boundaries. As introduced previously, the properties of machine component materials are closely dependent on their operating temperature, this is especially true for the PMs, hence machine electromagnetic performance is

impacted by temperature. On the other hand, machine electromagnetic performance, such as power losses, also has a direct impact on the machine temperature field. Therefore, an iterative process needs to be adopted for machine electro-thermal-fluid coupling analysis to accurately capture the temperature effects on machine electromagnetic performance. Thus, the machine thermal calculation method can be summarised as follows:

1. Firstly, the losses of the different components of the machine at initial temperature T_k are obtained through electromagnetic analysis, these losses are then used in the machine CFD fluid-thermal analysis as heat sources;

2. Using the updated heat sources, a new calculated temperature T_{k+1} is obtained and the electromagnetic properties of the materials of the machine components updated to reflect the new working temperature T_{k+1} for the next round of electromagnetic analysis;

3. The electromagnetic and thermal-fluid analyses are repeated iteratively until the maximum temperature difference between T_{k+1} and T_k is less than a pre-set requirement.

5.1.1 Fluid field fundamental theory

Determining the electrical machine temperature is an important consideration with regard to machine power losses and thermal dissipation. Machine heat exchange is achieved through heat transfer and heat convection. Normally, the fluid flow state can be defined as either laminar or turbulent within a tubular flow model. The fluid state can be determined from its Reynolds number R_e, which is defined as:

$$R_e = \rho \frac{v_{fl} d}{\mu} \tag{5.1}$$

where ρ is the fluid density, v_{fl} is the fluid flow speed, d is the fluid flow tube diameter and μ is the fluid viscosity. If the flow Reynolds number is below 2300, then the flow can be regarded as laminar; while if the flow Reynolds number is above 2300, then the flow is regarded as a turbulent one. For the fluid field in a HSPMM, the machine rotor is rotating at high speed and the machine cooling air fluid flow is a turbulent one. Before setting up the equations for the machine thermal-

fluid calculation model, it is necessary to set out some assumptions as follows:

(1) The cooling air is regarded as an incompressible turbulent fluid, because the speed of the cooling air flow in the machine cooling system is less than the speed of sound;

(2) The cooling air in the ventilation path flows constantly and is not impacted by gravity or buoyancy.

The forced cooling air fluid in the machine should satisfy the principles of mass conservation, momentum conservation and energy conversion, respectively. Based on thermal transfer theory, the three-dimensional steady temperature field model for the machine region in Cartesian coordinates can be expressed as a boundary value problem [138]:

$$\begin{cases} \dfrac{\partial}{\partial x}K_x(\dfrac{\partial T}{\partial x})+\dfrac{\partial}{\partial y}K_y(\dfrac{\partial T}{\partial y})+\dfrac{\partial}{\partial z}K_z(\dfrac{\partial T}{\partial z})=-q \\ T(x,y,z)\big|_{S_1}=T_1 \\ h(T-T_f)\big|_{S_2}=-K_n\dfrac{\partial T}{\partial n} \end{cases} \tag{5.2}$$

where T is the temperature; K_x , K_y and K_z are the thermal transfer coefficients in the x, y, z direction, respectively and q is the thermal source density; T_1 is the given temperature on boundary S_1; n is the vertical vector component on the boundary; h is the thermal convective coefficient and T_f is the air fluid temperature.

5.1.2 Fluid-thermal coupling model for HSPMM

High speed operation of electrical machines increases electromagnetic and mechanical power losses, and these losses act as machine heat sources causing the machine temperature to rise. The researched HSPMM uses a composite air and water cooling system for machine thermal dissipation. Cooling air is pumped into the machine at one end, passes through the air ducts inside the stator slots axially extracting heat, then flows out through the other end. In addition, circumferential grooves are also ducted around the machine frame and provide a water cooling path for the machine. In this study, CFD is utilized to research on machine thermal performance. Fig. 5.1 displays the HSPMM model including its cooling system.

Based on the symmetrical structure of the machine, one stator slot pitch proportion (1/36) of the HSPMM in the circumferential direction is modelled using CFD to estimate the machine temperature distribution. It is a three-dimensional (3D) fluid-temperature coupling calculation model as shown in Fig. 5.2:

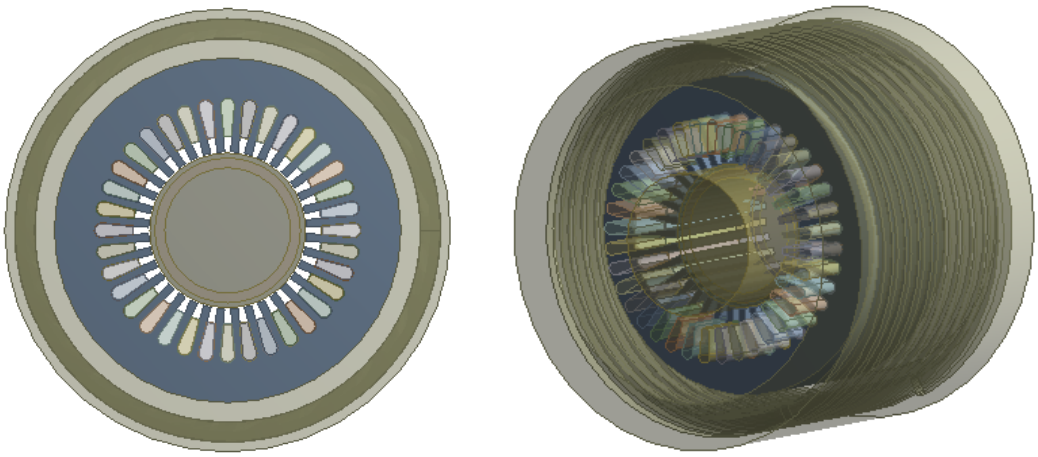

Fig. 5.1 High speed PM machine model showing details of the cooling structures.

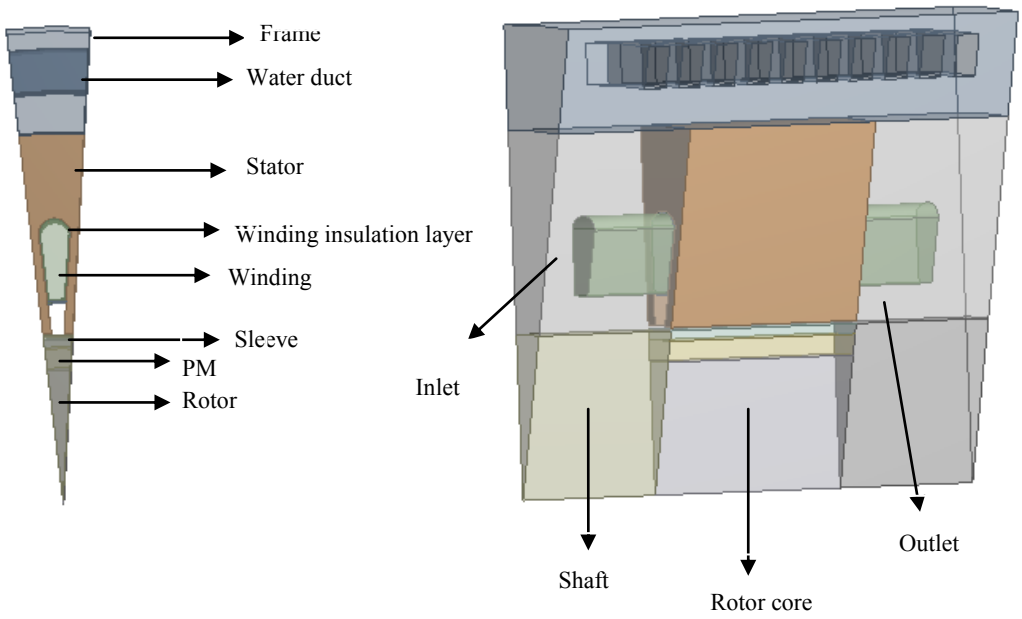

Fig. 5.2 Domain model for a high speed PM machine.

The fluid flow and thermal transfer in a HSPMM is a complex phenomenon; hence, conjugate heat transfer is utilized in machine thermal analysis, with forced cooling air flow, fluid region convection heat transfer and solid region conduction heat transfer all considered at the same time [139]. The air cooling system thermal

dynamics is calculated based on the fluid-solid coupling method. Considering the machine structure characteristics, the following assumptions and boundary conditions are adopted:

(1) The forced cooling air enters axially into the machine model through the inlet, hence, the inlet velocity conditions are applied to the model inlet, that is the air fluid speed and temperature are specified at the inlet.

(2) The forced cooling air exits the machine model through the outlet, with the pressure outlet boundary condition applied on the outlet side. The outlet pressure is set as standard atmospheric pressure.

(3) One stator slot pitch (1/36) of the HSPMM is modelled with rotational periodic conditions applied on both symmetry planes of the machine model.

(4) The contact surface of the rotor and air is set as a moving wall condition with rotational speed to consider the effect of rotor motion.

(5) The machine stator, winding, sleeve, and PMs are set as heat loads with power loss densities applied, accordingly.

(6) The thermal dissipation for the cooling water duct is set as forced convection, while the thermal conductivity coefficient and ambient environment temperature applied in each water duct region are set identically.

(7) The energy equation in the cooling air fluid region is set as the standard K-ε model for turbulence.

(8) The viscous dissipation term is included in the energy equation to consider the air drag force when the machine is rotating at high speed.

5.1.3 Equivalent insulation layer characteristics in the stator slots

The stator slots contain wires, insulation paper, insulation paint on the wires and gaps between the wires. In order to simplify temperature analysis, some assumptions are made [140]: Based on the principle of total mass constant, heat and thermal resistance, all copper wires are equivalent to a simple thermal conductive copper bar placed inside the stator slot; insulation paper, insulation paint on the wires, slot

wedge and the air gap between the copper wires are combined into an equivalent insulation layer, which is closely and evenly distributed around the winding bar as shown in Fig.5.3. The equivalent insulation layer properties, including density ρ, thermal conductivity coefficient C and specific heat capacity λ, can be obtained using equations (5.3) to (5.5) [140]:

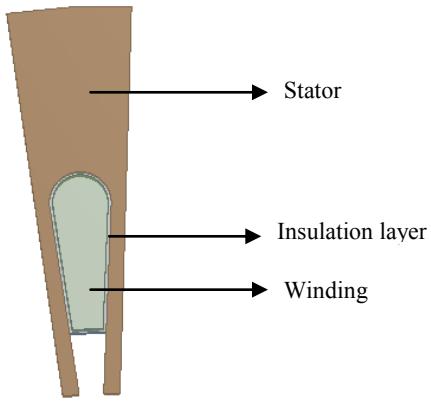

Fig. 5.3 Equivalent insulation layer in stator slot.

$$\rho = \frac{\sum_{i=1}^{N} \rho_i v_i}{\sum_{i=1}^{N} v_i} \tag{5.3}$$

$$C = \frac{\sum_{i=1}^{N} C_i \rho_i v_i}{\sum_{i=1}^{N} \rho_i v_i} \tag{5.4}$$

$$\lambda = \frac{\sum_{i=1}^{N} \delta_i}{\sum_{i=1}^{N} \frac{\delta_i}{\lambda_i}} \tag{5.5}$$

where ρ_i, v_i, C_i, δ_i and λ_i are the density, volume, specific heat capacity, equivalent thickness and equivalent thermal conductivity coefficient of each insulation material, respectively. The resulting machine equivalent insulation layer properties are presented in Table 5.1.

Table 5.1 Equivalent insulation layer property

Density (kg/m^3)	Specific thermal conductivity (W/(m·K))	Thermal conductivity coefficient (J/(kg·K))
386	1238	0.086

5.1.4 Cooling water path thermal coefficient

A circumferential groove is ducted around the machine frame as a water cooling path, with cooling water entering into the machine frame from the entrance on one side of the machine and leaving through the water cooling path exit on the other side. As the temperature difference between the entrance and exit of the water path is small, the thermal transfer method is applied assuming forced convection giving:

$$\dot{Q} = \alpha A(T_a - T_b) \tag{5.6}$$

where $\dot{Q}$ is the heat transferred per unit time; α is the heat transfer coefficient; A is the object area; T_a and T_b are the temperatures on the object surface and the fluid, respectively. The thermal convection transfer coefficient of the cooling water and frame α can be obtained as:

$$\alpha = \frac{N_u \lambda}{d} \tag{5.7}$$

where λ is the fluid thermal conductivity coefficient; d is the characteristic diameter; N_u is the Nusselt number, which is defined as the ratio of the heat transferred across the boundary between adjacent layers. The Nusselt number can be evaluated based on empirical correlations for a wide variety of geometries. For free convection, it is a function of the Rayleigh number R_a and Prandtl number P_r written as:

$$N_u = f(R_a, P_r) \tag{5.8}$$

while for forced convection, it is a function of the Reynold number R_e and Prandtl number P_r written as:

$$N_u = f(R_e, P_r) \tag{5.9}$$

5.1.5 Temperature field for HSPMM

Based on the above analysis, a HSPMM thermal model with both forced air and water cooling can be established in CFD, with the electromagnetic power losses obtained in each machine component transformed into power loss densities and applied to the corresponding component as heat sources in the model. An iterative calculation procedure is used to consider the impact of machine power losses on temperature. Fig 5.4 presents the stream line and vector distribution of the machine forced cooling air system. It can be seen that the fluid motion in the air cooling system is quite complicated and that the fluid velocity in the air domain varies in the fluid region: Due to the high speed rotation of the machine, the air fluid near the machine rotor has circumferential components; hence, the cooling air is deemed to be a turbulent flow. Moreover, the air fluid velocity near the machine rotor surface is also much higher than that in other air fluid regions.

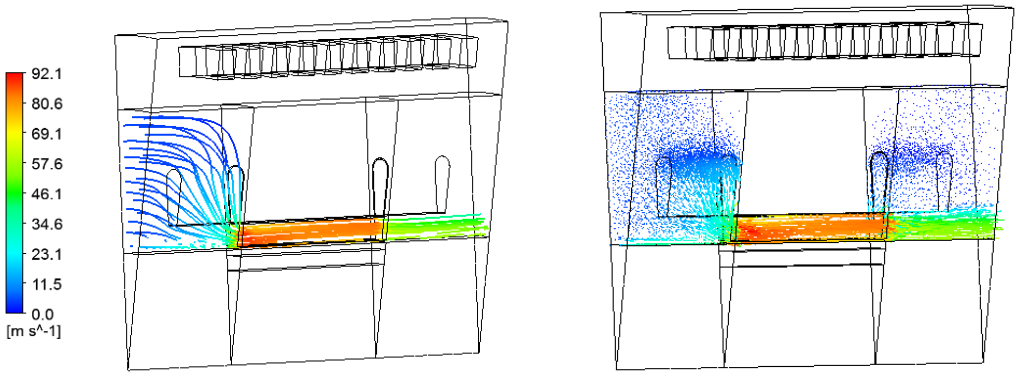

(a) Stream line (b) Stream vector

Fig. 5.4 Fluid distribution.

Fig 5.5 presents the temperature distribution results for a HSPMM rotating at a speed of 11000 rpm and 17000 rpm (rated speed), respectively; Fig 5.6 further displays the PM temperature distribution for the machine at rated speed. It can be seen that the temperature distribution is uneven over the PM. The PM has a maximum temperature of 381.2K at a spot in the middle of the PM region for machine; the maximum temperature increases significantly with increasing machine speed, which is due to larger electromagnetic power losses and mechanical air frictional loss, as illustrated

in the previous chapter. The maximum temperature spot for the whole HSPMM occurs in the middle of carbon fibre sleeve due to its low thermal conductivity property. The machine rotor temperature declines from the middle to both shaft ends when axial forced air cooling is utilized. The HSPMM winding temperature is also found to be unevenly distributed axially in the temperature field calculation results: the air fluid temperature at the machine cooling air entrance side is lower, which is beneficial to thermal dissipation for the machine winding end near it. As the axial air temperature rises at the fluid exit side, its cooling effect on the machine winding is weakened; hence, the winding temperature near the cooling air system exit side is higher leading to the observed temperature difference in the winding axial direction.

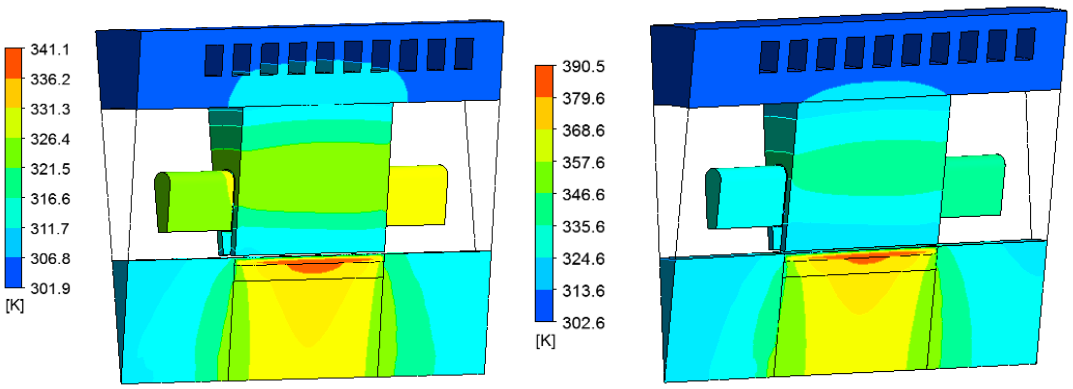

(a) 11000 rpm (b) 17000 rpm

Fig. 5.5 HSPMM temperature distribution

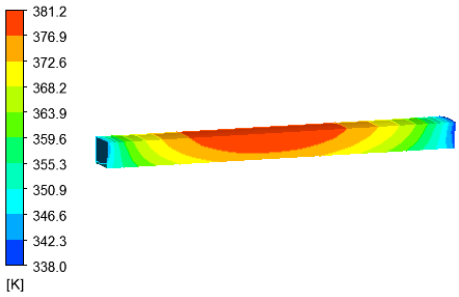

Fig. 5.6 PM temperature distribution

5.2 Factors impacting HSPMM temperature

(a) Effects of forced cooling air velocity

The axial forced cooling air system plays an important role in HSPMM temperature performance, therefore it is important to gain an understanding of the effects of the velocity of the air flow. Fig. 5.7 shows the relationship between the maximum temperature of the HSPMM components and airflow axial velocities for a machine operating at rated speed.

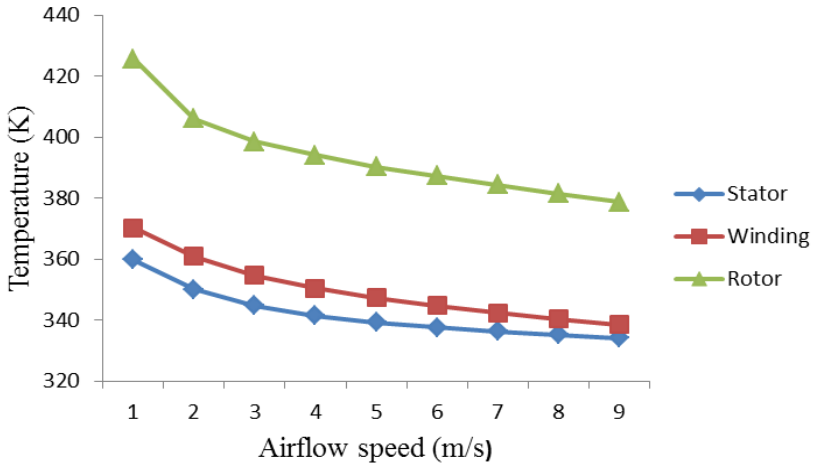

Fig. 5.7 Machine components maximum temperature and airflow velocity.

It can be seen that the temperature in all HSPMM components reduces significantly when the forced air flow velocity increases within the low cooling airflow speed range (1-2m/s). For higher speeds, the temperature continues to drop but at a much lower rate. This is due to the fact that air frictional losses also increase with the airflow velocity as illustrated in the previous chapter. Hence, it can be concluded that increasing the axial forced cooling airflow speed is beneficial; but its cooling effect becomes limited at high airflow speeds due to the extra air frictional loss induced by the airflow itself.

(b) Effects of rotor eddy current loss

HSPMM temperature rise due to rotor eddy current losses requires particular attention, as rotor losses directly heat the rotor impacting the working temperature of the PMs. Fig. 5.8 presents the relationship between machine rotor PM eddy current loss and the maximum machine component temperature for a HSPMM working at rated speed. It can be observed that machine rotor maximum temperature rises linearly with PM eddy current loss; while there is little impact on the maximum temperatures of the machine stator and winding components. This is a consequence

of the low thermal conductivity of the air flow. When the PM eddy current loss varies from 5W to 45W, the rotor maximum temperature increases by around 20K: it equals to a temperature rise ratio of 0.5K/W. Therefore, rotor eddy current loss has a critical impact on HSPMM rotor temperature rise, even though rotor eddy current loss is only a relatively small proportion of overall machine power losses.

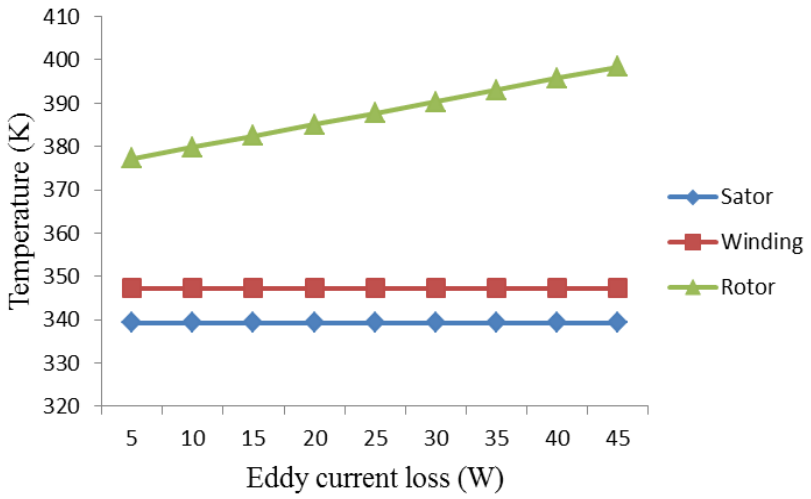

Fig. 5.8 Maximum temperature of machine components as a function of rotor PM eddy current losses.

(c) Effects of sleeve thermal conductivity

A high mechanical strength rotor retaining sleeve is normally used around the surface-mounted permanent magnet rotor to maintain mechanical integrity when the HSPMM is in high speed operation. The sleeve physical properties can also influence machine performance due to their impact on both the electromagnetic and temperature fields. Fig. 5.9 displays the relationship between rotor sleeve thermal conductivity and the maximum temperature of PMSM components for a HSPMM operating at rated speed. When the sleeve thermal conductivity varies from 0.3 W/ (m*K) to 1 W/ (m*K), the rotor maximum temperature drops from 403.2K to 362.8K. It can be concluded that the rotor temperature is greatly impacted by the thermal conductivity of the sleeve material, while the stator and winding temperature are not impacted. Therefore, the rotor sleeve material should be carefully chosen to take account of both electromagnetic and mechanical constraints, while having high thermal conductivity in order to reduce HSPMM rotor operational temperature.

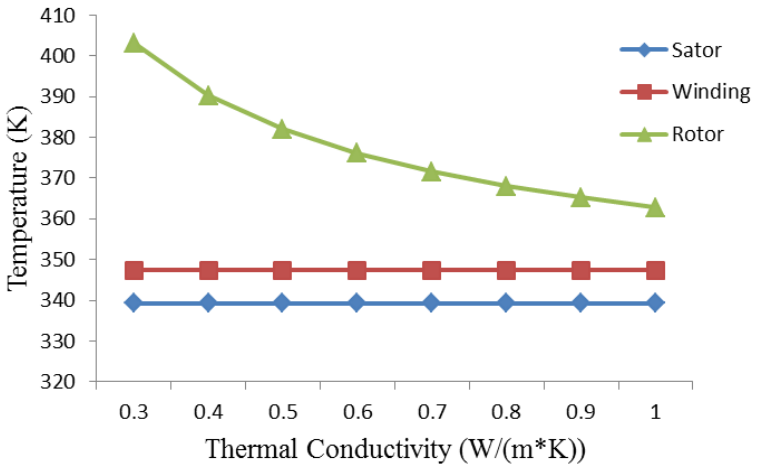

Fig. 5.9 Maximum temperature of machine components as a function of rotor sleeve thermal conductivity

5.3 Experimental tests on a HSPMM

To verify the effectiveness of the HSPMM thermal calculation results, machine temperature experimental tests have been conducted on a prototype HSPMM. The rated power of the prototype machine is 150 kW, and the rated speed is 17,000 rpm. The author participate the design of the machine, while the machine prototype is manufactured and experimentally tested in Chongqing Dema Electrical Machine Research and Development Co. Ltd, China. The laboratory facilities are also located in the same company. Fig. 5.10 (a) and (b) present the photos of the HSPMM prototype stator iron core and rotor, respectively. Machine parameters are listed in Table 5.2.

(a) Stator iron core (b) Rotor

Fig. 5.10 HSPMM prototype

Experimental measurement of the HSPMM is based on a drag test platform as shown

in Fig 5.11. The prototype operates in motor mode at rated speed, and it is powered by a converter that is connected to the grid. The HSPMM drags the rotation of an asynchronous generator, which feeds its output power back to grid through a second converter. Fig. 5.11 (a) shows the converters in the test platform and Fig. 5.11 (b) shows the overall HSPMM experimental drag test setup. The HSPMM prototype is located on the left side in the figure and the dragged asynchronous generator is on the right.

Table 5.2 Design parameters of HSPMM prototype

Rated speed	17,000 rpm	Pole number	4
Stator outer diameter	350 mm	Stator inner diameter	160 mm
Iron core length	140 mm	Stator slot number	36
Conductor number per slot	4	Coil pitch	8
Air gap length	1.5 mm	Sleeve outer diameter	157 mm
PM outer diameter	147 mm	PM thickness	10 mm
PM type	N38UH	Pole arc pole pitch	0.75

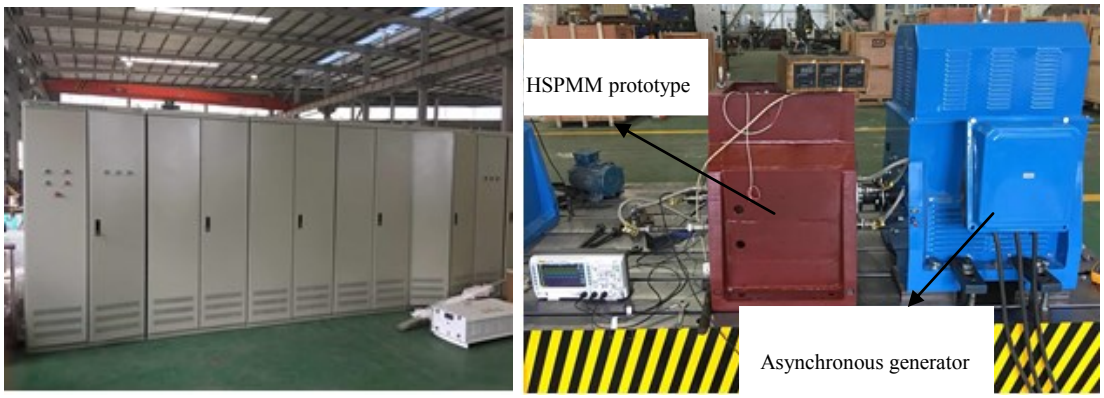

(a) Converters. (b) Experimental drag test setup (left: HSPMM prototype right: asynchronous generator).

Fig. 5.11 HSPMM experimental test.

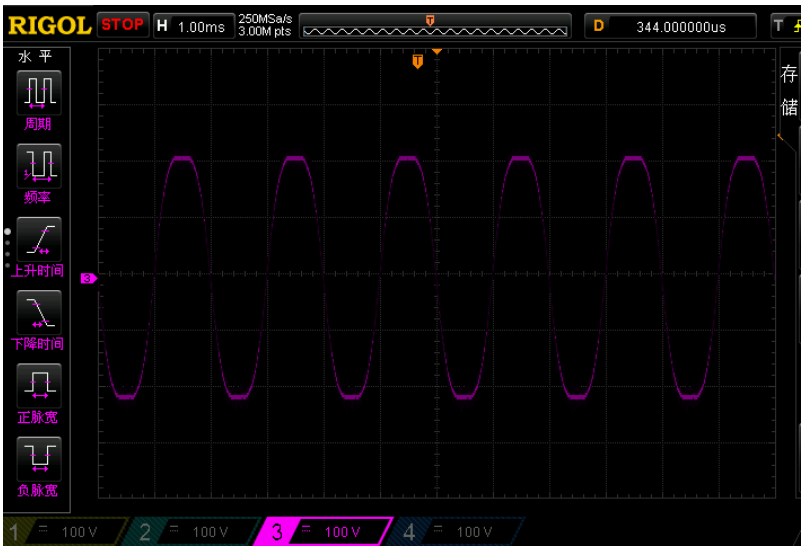

(a) measurement

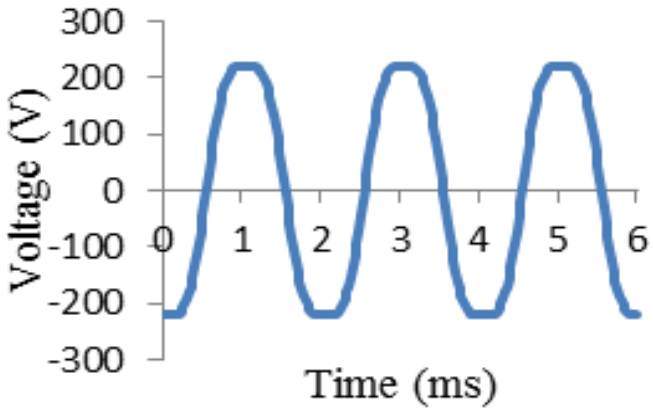

(b) FEM

Fig. 5.12. EMF waveforms for HSPMM at 15,000 rpm

Fig. 5.12 (a) presents the HSPMM EMF waveforms measured from the machine at 15,000 rpm, while (b) presents the result predicted by FEM. The measurement results are obtained by oscilloscope Rigol TBS 2000. Fig. 5.13 shows the comparison between FEM and measurements for the HSPMM operating at different speeds. Good agreement can be observed between the two results. Fig. 5.13 further presents the measured power loss results for the HSPMM at different speeds with no load. The prototype machine power losses are measured on DM510000498 electrical machine test platform. The no load loss is significantly increased with machine speeds.

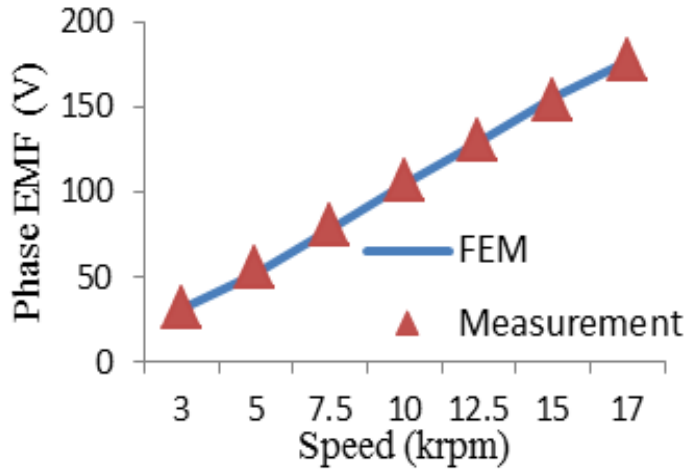

Fig. 5.13 EMF for HSPMM at different speeds.

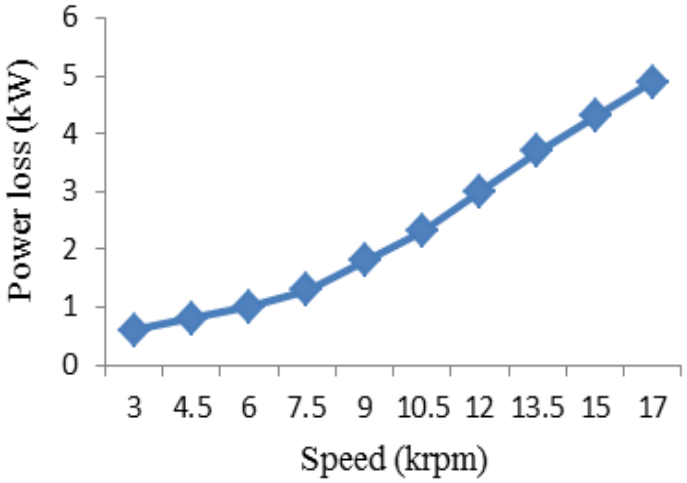

Fig. 5.14. Power loss measurement results for HSPMM at no load.

Temperature detectors (thermal resisters) are installed on the HSPMM prototype stator iron core and windings and infrared temperature detectors are used for temperature measurement at the machine rotor shaft ends. Table 5.3 shows the HSPMM temperature results predicted by CFD and measurement, while Fig. 5.16 presents the HSPMM experimental measurement results for the prototype operating in motor mode at rated condition. It can be found that the machine temperatures stabilise after around 60 mins. HSPMM experimental test results agree well with the results predicted by the CFD analysis. Therefore, the effectiveness of the machine CFD thermal modelling and the power losses estimation results for HSPMMs are verified by the experimental test. The potential reason for the difference between CFD and measurement is due to the simplification of the machine model when

compared with the actual machine.

Table 5.3 CFD predicted HSPMM temperature results

	Cooling air inlet			Cooling air outlet		
	stator	winding	shaft end	stator	winding	shaft end
T (°C) by CFD	47.6	61.5	41.9	56.2	67.9	56.2
T (°C) by measurement	49.1	59.5	39.5	54.5	69.1	53.9
error	3.1%	3.4%	6.1%	3.1%	1.7%	4.3%

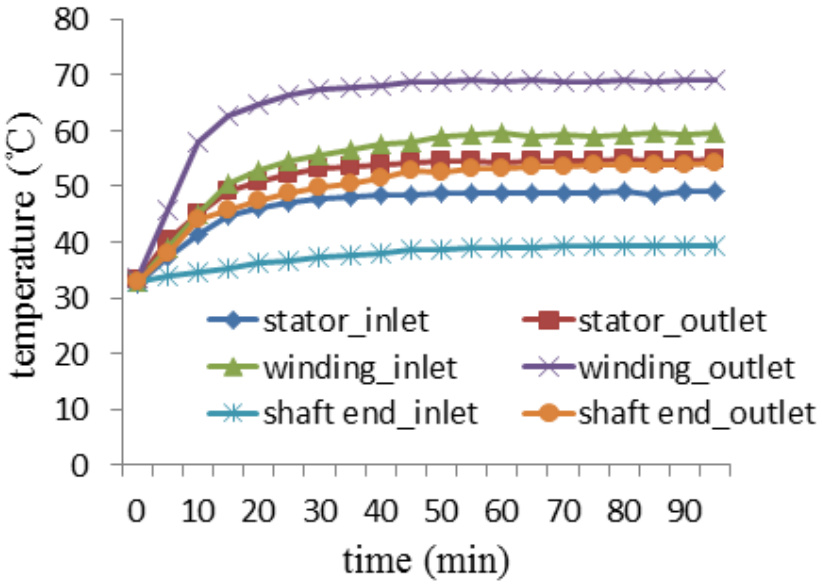

Fig. 5.16 HSPMM temperature measurement results.

5.4 Conclusions

In this chapter, the HSPMM temperature field is studied using a fluid-thermal CFD model of the heating effect of machine power losses, while factors that influence machine thermal performance are also studied. Machine thermal modelling is

established with applied boundary conditions detailed. The HSPMM temperature results predicted by CFD are also verified by experimental testing on a prototype machine. From the analysis conducted, it is found that:

(1) The maximum temperature region is located in the middle of the machine rotor.

(2) The potential for forced air flow machine cooling is constrained due to air frictional loss with air flow velocity.

(3) The machine rotor maximum temperature increases linearly with rotor eddy current loss, but stator and winding temperatures are not significantly affected due to the low thermal conductivity of air.

(4) Selecting a high thermal conductivity sleeve is helpful for reducing rotor operating temperature for machines designed for high speed applications.

(5) Experimental testing on a HSPMM prototype show good agreement between the analysis results and the measurement results.

Chapter 6
Mechanical design of high speed permanent magnet machines

6.1 Introduction

In high speed applications, rotor mechanical issues are critical topics in HSPMM machine design. A key consideration in high speed machine design is rotor strength analysis. A surface-mounted PM rotor structure is adopted for the machine investigated in this study with the rare earth alloy NdFeB used as the PM material. For HSPMMs, the PMs are regarded as the most mechanically vulnerable rotor component [141] due to the fact that the PMs have high compressive strength but low tensile stress strength. Therefore, a high mechanical strength rotor sleeve is placed outside the PM surface to avoid PM mechanical damage caused by the centrifugal force on the rotor in high speed operation. The rotor material, structure

and mechanical fit between rotor components have a dramatic influence on rotor mechanical performance. In this chapter, HSPMM rotor strength is comprehensively studied for different rotor configurations. Rotor operating conditions are also considered. Another issue for high speed rotor design is its dynamic analysis. Accurate prediction of rotor natural frequencies is clearly critical in high speed machine design, as machine rotor operational speed must be kept away from these critical speeds. Otherwise, there is a risk of rotor vibration leading to excessive acoustic noise or even catastrophic mechanical failure. Here, FEM is used to validate the rotor dynamic performance at the rotor operating speed.

6.2 Mechanical strength analysis for a high speed rotor with sleeve

Rotor strength assessment is normally analytically performed based on thick-walled cylinder elasticity theory, which is described in detail in [142]. The permanent magnet machine rotor model is shown in Fig. 6.1. The rotor is represented as a compound structure of three concentric cylinders which correspond to the sleeve, magnet and rotor core, respectively. In order to have a deep understanding of the model in Fig 6.1, analytical modelling is studied in this section.

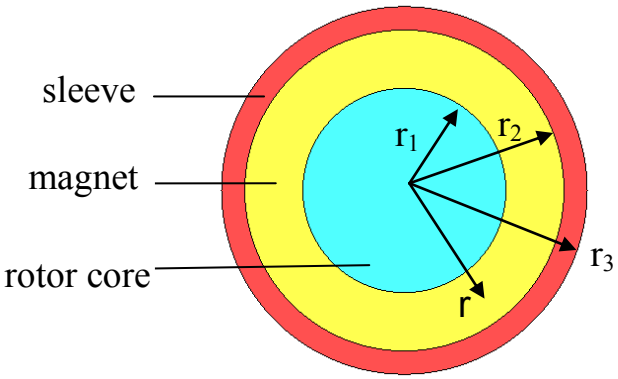

Fig. 6.1 Rotor model.

If rotor axial strain is not considered, the kinetic equation for the rotor sleeve can be specified as:

$$\frac{d\sigma_r}{dr}+\frac{\sigma_r-\sigma_\theta}{r}+\rho\omega^2 r=0 \tag{6.1}$$

where σ_r and σ_θ denote the stress in the radial and tangential direction; ρ, ω and r are the material density, rotor speed in rad/sec and radius, respectively. Then, the sleeve

stress and displacement can be obtained as:

$$\sigma_r = A + \frac{B}{r^2} - \frac{3+\mu}{8}\rho\omega^2 r^2 \tag{6.2}$$

$$\sigma_\theta = A - \frac{B}{r^2} - \frac{1+3\mu}{8}\rho\omega^2 r^2 \tag{6.3}$$

$$u_r = \frac{r}{E}[(1-\mu)A - (1+\mu)\frac{B}{r^2} - \frac{1-\mu^2}{8}\rho\omega^2 r^2] \tag{6.4}$$

where u_r is the radial displacement, E and μ are the elasticity Young's modulus and Poisson's ratio, respectively, A and B are boundary coefficients which are dependent on the rotor operating conditions. The rotor sleeve and PM are always assembled and secured by an interference fit to maintain an assembled pressure P_0 on the PMs, while δ_0 is the fit shrink range.

For the rotor under static conditions, the assembled pressure P_0, and the PM stress in the radial and tangential directions can be obtained as follows: (the subscript m and e represent magnet and sleeve, respectively):

$$P_0 = \frac{\delta_0}{r_2\left[\frac{1}{E_m}(\frac{r_2^2+r_1^2}{r_2^2-r_1^2} - \mu_m) + \frac{1}{E_e}(\frac{r_3^2+r_2^2}{r_3^2-r_2^2} + \mu_s)\right]} \tag{6.5}$$

$$\sigma_{mr} = P_0 \frac{r_2^2}{r_2^2 - r_1^2}(1 - \frac{r_1^2}{r^2}) \tag{6.6}$$

$$\sigma_{m\theta} = P_0 \frac{r_2^2}{r_2^2 - r_1^2}(1 + \frac{r_1^2}{r^2}) \tag{6.7}$$

Then the equivalent stress can be obtained as:

$$\sigma_{equ} = \sqrt{\frac{1}{2}\left[(\sigma_{mr} - \sigma_{m\theta})^2 + \sigma_{mr}^2 + \sigma_{m\theta}^2\right]} \tag{6.8}$$

For the rotor running at high speed, the sleeve and PM will deform radially due to the centrifugal force experienced. Hence, the shrink range may also change accordingly.

The PM radial displacement u'_{mr} and sleeve radial displacement u'_{sr} are given as [143]:

$$u'_{mr} = A_m r_2 + \frac{B_m}{r_2} - \frac{\rho_m (1-\mu_m^2)\omega^2 r_2^3}{8E_m} \tag{6.9}$$

$$A_m = \frac{(3+\mu_m)(1-\mu_m)(r_1^2 + r_2^2)\rho_m \omega^2}{8E_m} \tag{6.10}$$

$$B_m = \frac{(3+\mu_m)(1+\mu_m) r_1^2 r_2^2 \rho_m \omega^2}{8E_m} \tag{6.11}$$

$$u'_{er} = A_e r_2 + \frac{B_e}{r_2} - \frac{\rho_e (1-\mu_e^2)\omega^2 r_2^3}{8E_e} \tag{6.12}$$

$$A_e = \frac{(3+\mu_e)(1-\mu_e)(r_2^2 + r_3^2)\rho_e \omega^2}{8E_e} \tag{6.13}$$

$$B_e = \frac{(3+\mu_e)(1+\mu_e) r_2^2 r_3^2 \rho_e \omega^2}{8E_e} \tag{6.14}$$

where ρ_m and ρ_e are the densities of the magnet and sleeve materials, respectively. Hence, the fit shrink range δ with rotor rotation considered can be obtained as:

$$\delta = \delta_0 - (u'_{er} - u'_{mr}) \tag{6.15}$$

Then the PM dynamic pressure P for the rotor in high speed operation can be obtained as:

$$P = \frac{\delta}{r_2 [\frac{1}{E_m}(\frac{r_2^2 + r_1^2}{r_2^2 - r_1^2} - \mu_m) + \frac{1}{E_e}(\frac{r_3^2 + r_2^2}{r_3^2 - r_2^2} + \mu_e)]} \tag{6.16}$$

Then the PM radial stress σ'_{mr} and tangential stress $\sigma'_{m\theta}$ for the rotor in high speed operation can be described as:

$$\sigma'_{mr} = \rho_m \omega^2 \frac{3+\mu_m}{8}(r_1^2 + r_2^2 - \frac{r_1^2 r_2^2}{r^2} - r^2) - P\frac{r_2^2}{r_2^2 - r_1^1}(1 - \frac{r_1^2}{r^2}) \tag{6.17}$$

$$\sigma'_{m\theta} = \rho_m \omega^2 \frac{3+\mu_m}{8}(r_2^2 + r_1^2 + \frac{r_1^2 r_2^2}{r^2} - \frac{1+3\mu_m}{3+\mu_m} r^2) \tag{6.18}$$

Then the equivalent stress can be obtained as:

$$\sigma'_{equ} = \sqrt{\frac{1}{2}\left[(\sigma'_{mr} - \sigma'_{m\theta})^2 + \sigma'^2_{mr} + \sigma'^2_{m\theta}\right]} \tag{6.19}$$

Based on the theory above, reference [143] also provided the analytical solution for a cylinder PM rotor retained by a non-magnetic sleeve. The following rotor parameters were used by [143]:

•Rotor speed: 60,000 rpm.

•Sleeve: Outer diameter: 0.063m; Inner diameter: 0.05074m; density: 8240 kg/m^3;

Young's modulus: 187.5 GPa Poisson's ratio: 0.28

•PM: Outer diameter: 0.051m; Inner diameter: 0.024m; density: 7400 kg/m^3;

Young's modulus: 150 GPa Poisson's ratio: 0.24

In this dissertation, the Finite Element Method (FEM) is employed to study the rotor strength for the surface-mounted HSPMM rotor introduced in referenced [143]. FEM software Ansys is utilized in this study due to its friendly user-oriented environment. A 3D rotor model is developed as shown in Fig. 6.2, while the sleeve face and PM face are coupled to imitate the interference fit assembly effect that exists between the faces of the two rotor components.

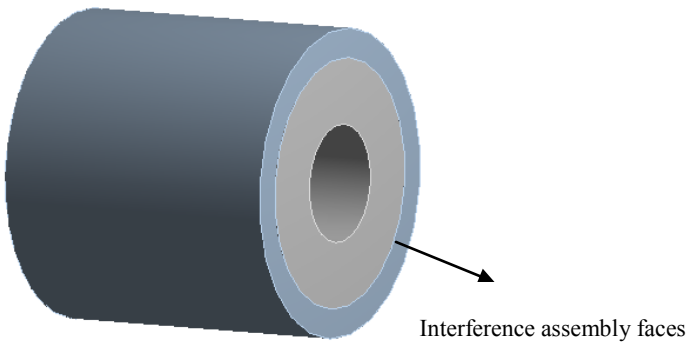

Fig. 6.2. Rotor model.

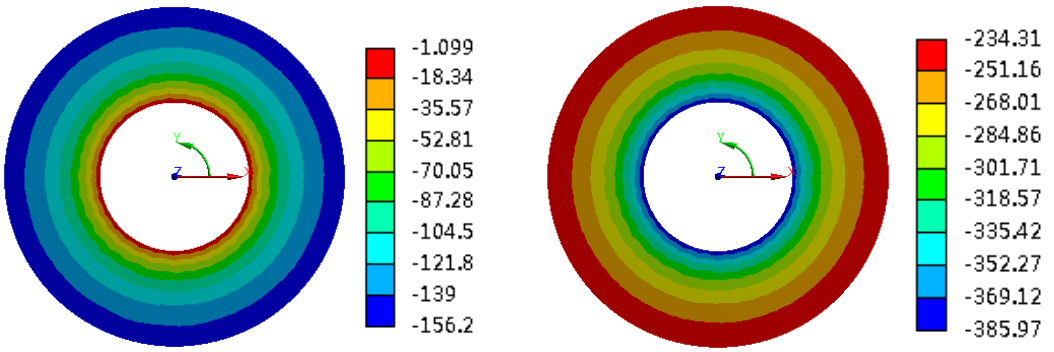

radial stress tangential stress

(a) Rotor stresses under static conditions.

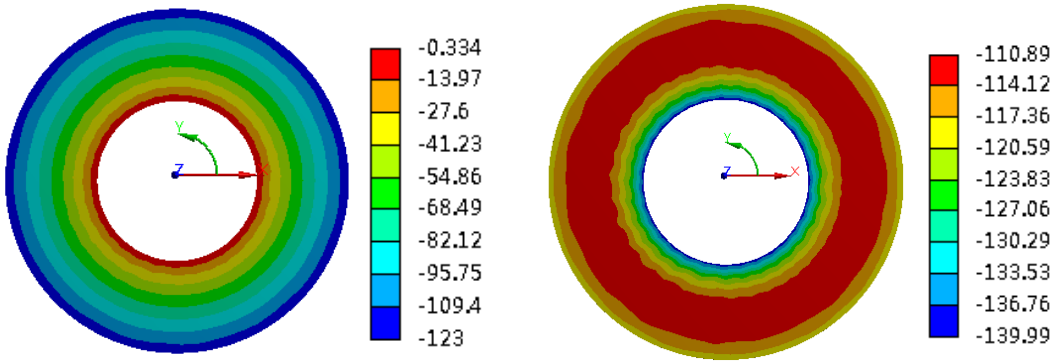

radial stress tangential stress

(b) Rotor stresses at rated speed operation.

Fig. 6.3 PM stress distribution (Unit: MPa)

Fig. 6.3 shows the radial and tangential stress distribution on the machine's ring-shape PM for the rotor under static and rated speed operating conditions, respectively. It can be observed that due to the centrifugal force experienced under high speed rotation, strain occurs in both the sleeve and PM; hence, the interference shrink range between the faces of the two components varies. Thus results in changes in the PM stress distribution. Fig. 6.4 further details the FEM predicted PM stress distribution in the radial direction for the rotor under the two operational conditions introduced. Table 6.1 further compares the PM stress range estimated by the analytical method and FEM, respectively. It can be seen that the FEM predicted results are consistent with the results calculated by the analytical method. This validates the effectiveness of the FEM rotor model built in this dissertation.

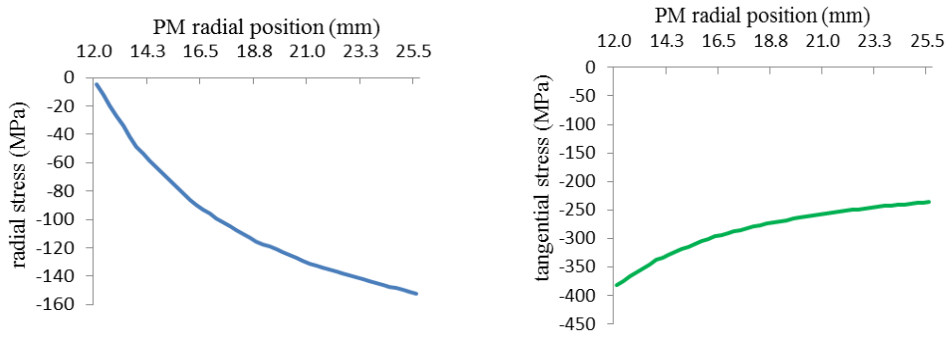

radial stress tangential stress

(a) Rotor stresses profile under static conditions.

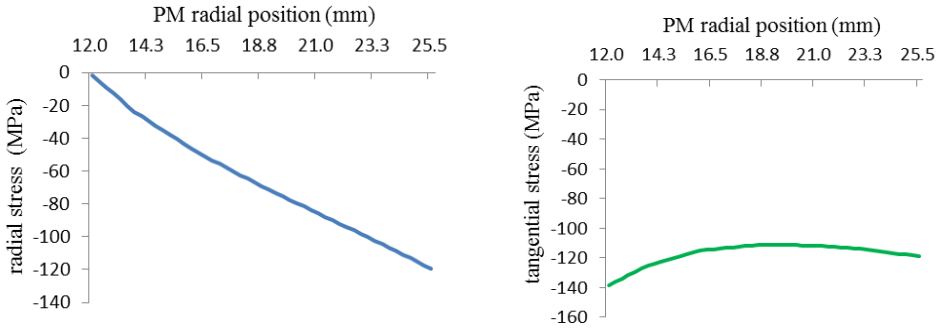

radial stress tangential stress

(b) Rotor stress profile at rated speed operation.

Fig. 6.4 PM stress distribution along the PM line in the radius direction.

Table 6.1 A comparison of the PM stress ranges obtained analytically and using FEM

	Static		Rated speed	
	Radial	Tangential	Radial	Tangential
Analytical (MPa)	0 ~ -144.8	-372.1 ~ -227.2	0 ~ -113.7	-130.2 ~ -102.0
FEM (MPa)	-4.6 ~ -152.0	-381.8 ~ -236.1	-1.8 ~ -119.5	-138.5 ~ -111.2

6.3 Rotor strength research with pole filler

The centrifugal force experienced by the PMs is significantly increased with

increasing rotor operating speed. Since the PM material is weak in tension, excessive force may cause PM damage and decrease rotor reliability when employing machine rotors with surface-mounted PMs. Therefore, a rotor sleeve is normally used to protect the PMs from the centrifugal force. Generally, there are two kinds of material that can be chosen: one is non-metal such as a carbon fiber bandage; the other is a non-magnetic alloy such as a titanium alloy [143]-[144]. Carbon fiber has lower electrical conductivity that benefits HSPMMs in terms of rotor eddy current loss reduction, but its thermal dissipation capability is lower than its metal counterpart. Table 6.2 provides the details of the mechanical properties of carbon fiber and Ti-alloy, together with that of the PM material NdFeB.

Table 6.2 Material mechanical properties

Material property	Ti alloy	Carbon fiber		PM
		Radial	Tangential	
Density (kg/m^3)	4500	1680		7400
CTE (1/K)	8.8 E-6	2.8E-5	-3.8E-7	4E-6
Young's Modulus (GPa)	105	8.8	120	160
Poisson's ratio	0.28	0.015	0.28	0.24
Maximum permitted stress (MPa)	850	-70	600	Tensile: 85 Compressive: 1100

For the HSPMM rotor considered in this study, the number of rotor pole pairs is 2, the sleeve outer diameter is 157 mm while the sleeve thickness is 5mm. As for the rotor PM, the pole arc pole pitch is set as 0.75, while its thickness is 10mm. As introduced previously the PM can sustain large compressive stress but is vulnerable to tensile stress. Hence, for surface-mounted PM rotors designed for high speed applications, the rotor sleeve and PM are normally interference fit assembled such

that the PMs are under pressure. This pressure can compensate for the tensile stress induced by the centrifugal force when rotating at high speed. It is an effective method of ensuring safe rotor operation at high speed. The interference fit δ has a significant impact on sleeve stress and the contact pressure between the rotor sleeve and PM: if δ is set too small, there is little PM and sleeve contact pressure and the protection effect is limited; however, if too large a δ is selected, the mechanical assembly process for the sleeve and PMs becomes very difficult and may even result in sleeve destruction. In this study, the interference fit δ is chosen as 0.12 mm following the analysis of rotor strength. The interference fit effect on rotor mechanical performance will be studied and illustrated in detail in the following sections. In order to leave a safety margin for the condition that the HSPMM rotor is able to operate in a safe state, the rotor speed is set 10% higher than the rated machine rotational speed in the analysis.

6.3.1 Rotor sleeve material comparison and temperature effects

Rotor mechanical strength is studied in this section with different rotor sleeve materials considered. Fig. 6.5 shows the Ti-alloy and carbon fiber sleeve stress distribution for a stationary HSPMM rotor; while Fig. 6.6 and Fig. 6.7 show the stress distributions on the PM and sleeve for the rotor rotating at high speed under normal (30 °C) and high (120 °C) temperature operating conditions when Ti-alloy and carbon fiber are used as sleeve material, respectively. As can be seen, the stress in both the sleeve and PMs is not uniformly distributed when the machine PM pole arc pole pitch is not set at 1.0 (compared with the results displayed in Fig. 6.3). When the machine is rotating at high speed, the maximum radial and tangential stress in the PM occurs in the inner pole side; while for the sleeve, the maximum stress occurs in the middle region of the sleeve between the two adjacent PM poles.

The temperature has a slight effect on the PM radial stress; however, it can be seen that the machine PM tangential stress is dramatically increased as the temperature rises. This can be explained as the pre-pressure effect, provided by the fit interference between the PM and sleeve surfaces, is weakened due to the thermal expansion of the rotor material. For the Ti –alloy-sleeve rotor and carbon-fiber-sleeve rotor, the PM tangential stress is 14.9 MPa and 9.8 MPa, respectively at normal temperature. This stress is tensile stress and can reach up to 82.7 MPa and 64.5 MPa

for the rotor at high temperature. Hence, the carbon fiber sleeve scheme is the preferred choice for the rotor considered in this dissertation, as it results in a lower PM tangential stress during high speed operation than a Ti-alloy sleeve.

The sleeve equivalent stress range shows a similar pattern to the tangential stress range; hence, the sleeve equivalent stress is mainly determined by tangential stress. Similar to the PM, the sleeve tangential stress is also found to increase substantially with rotor operating temperature. This is due to the fact that the rotor core coefficient of thermal expansion, CTE (1.1E-5), is larger than that of the PM and sleeve. Hence, the displacement of the rotor core outer surface due to thermal expansion is larger than that of the PM inner surface, while the sleeve hardly changes with operational temperature rise due to its low sleeve CTE. Therefore, the CTE diversity of the rotor components results in differences in thermal expansion displacement, and thus the contact pressure between the rotor sleeve and PM is increased when the rotor temperature rises. Hence, the sleeve tangential stress can be observed to increase with rotor operating temperature.

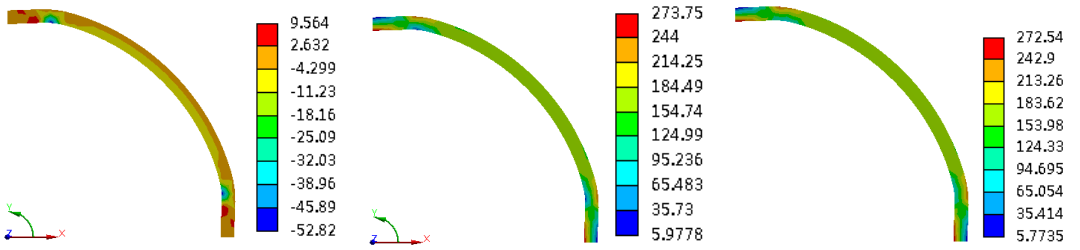

radial tangential equivalent

(a) Ti-alloy sleeve

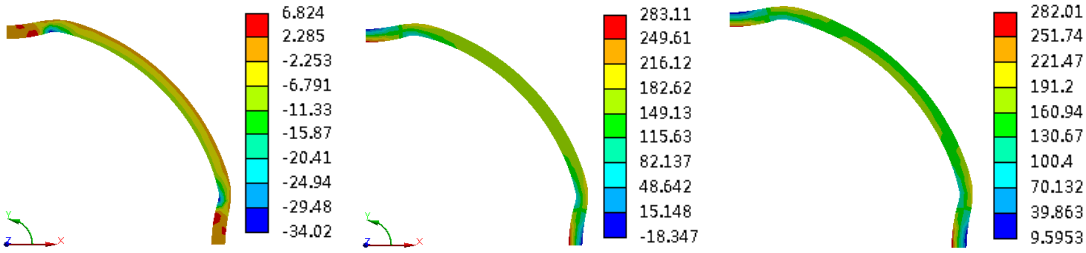

radial tangential equivalent

(b) Carbon fiber sleeve

Fig6.5. Sleeve stress for a stationary rotor (Unit:MPa).

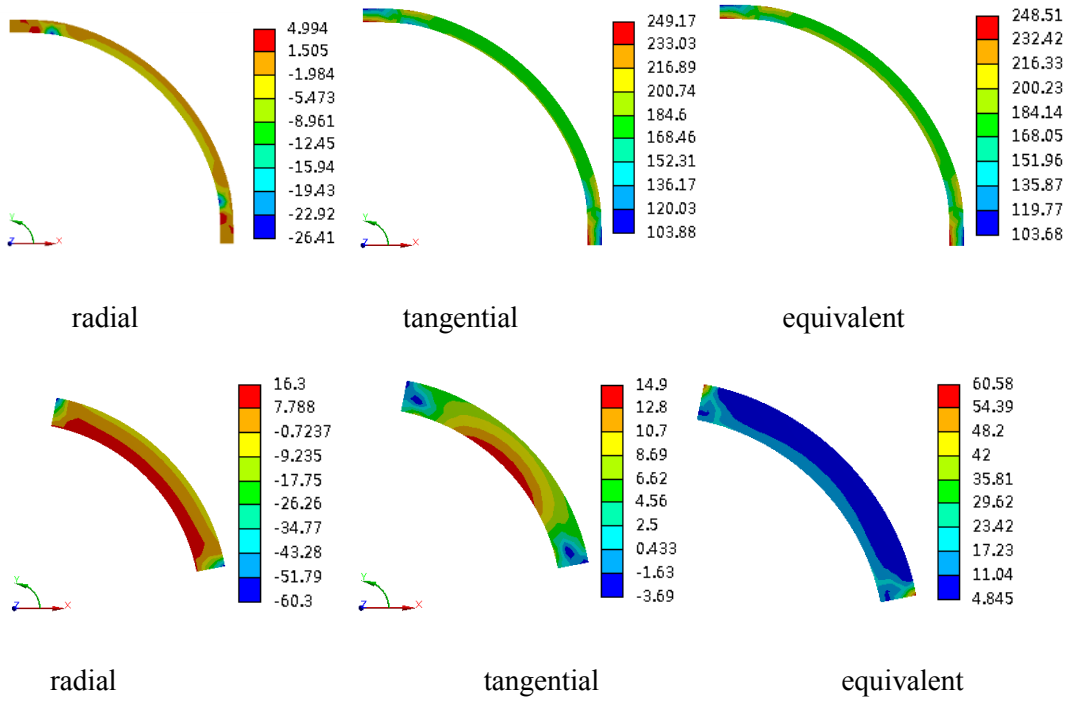

(a) Ti-alloy sleeve

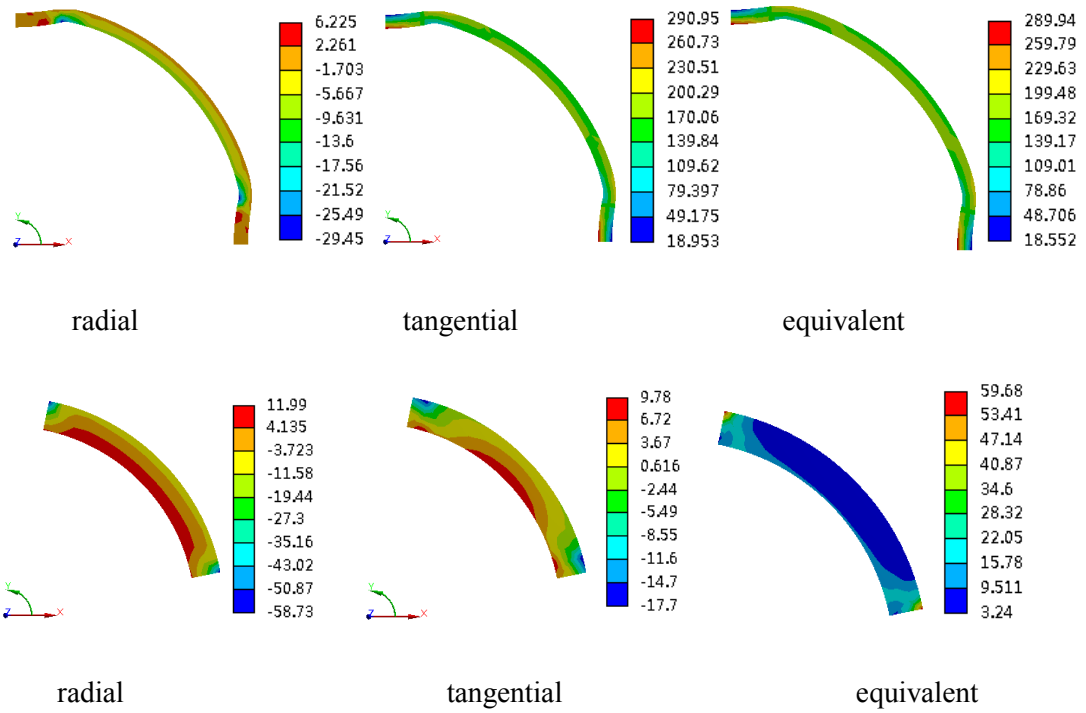

(b) carbon fiber sleeve

Fig 6.6. Sleeve and PM stress distributions for a rotor at normal temperature (Unit:MPa).

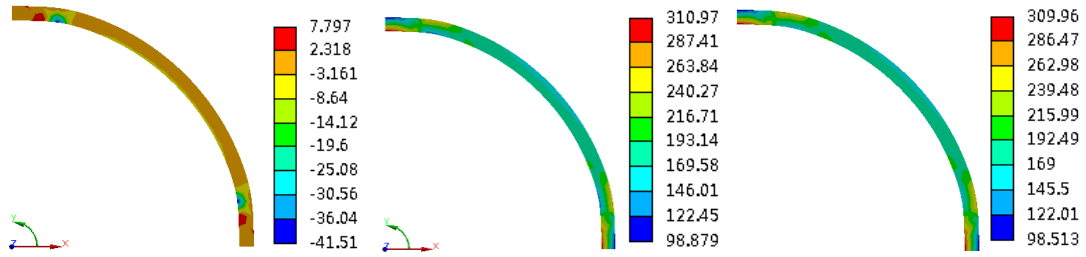

radial tangential equivalent

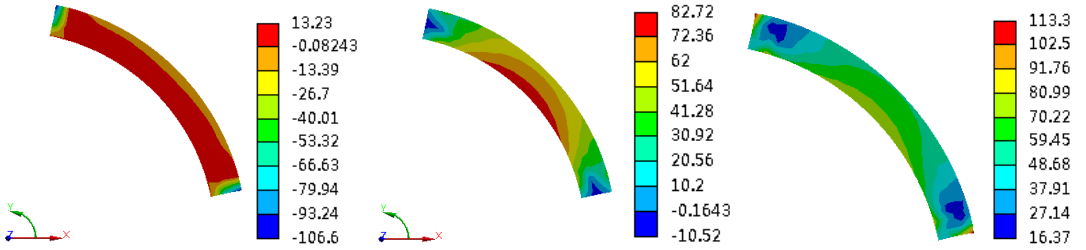

radial tangential equivalent

(a) Ti-alloy sleeve

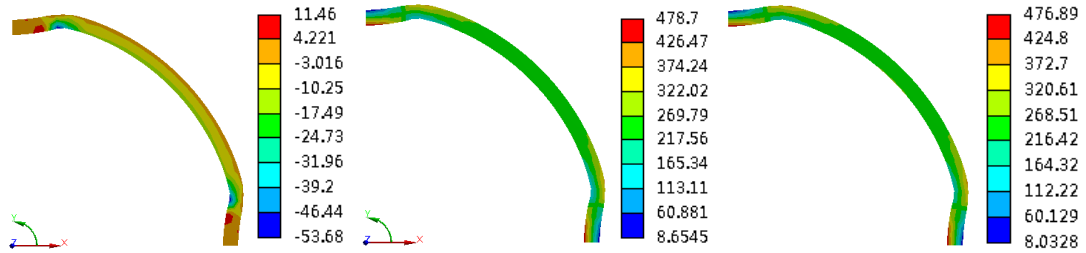

radial tangential equivalent

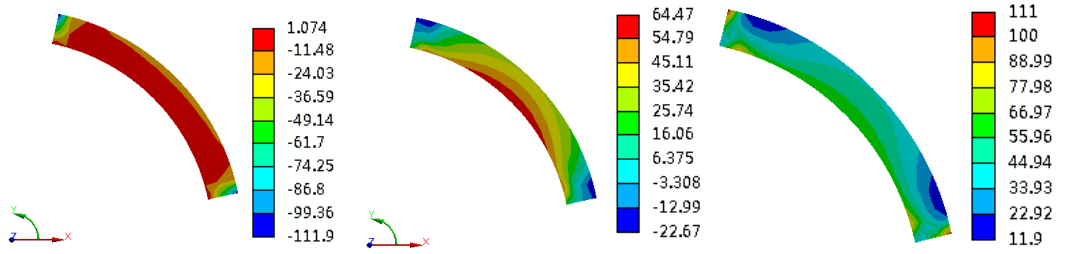

radial tangential equivalent

(b) Carbon fiber sleeve

Fig 6.7. Sleeve and PM stress distributions for a rotor at high temperature (Unit:MPa).

6.3.2 Selection of pole filler material

From the results of the previous section, it can be concluded that rotor sleeve stress concentration occurs, and the maximum stress is normally located at the middle region of the sleeve between two adjacent PM poles. Excessive concentrated sleeve stress due to the difference in thermal expansion of the rotor components may cause sleeve damage. Hence, in this section, a rotor structure with pole filler is studied with filler material considered. Fig. 6.8 presents the rotor structure with pole filler. Carbon fiber is chosen as the sleeve material, while Ti-alloy, Al-alloy and high mechanical strength plastic are considered as pole filler materials. Their mechanical properties are listed in Table.6.3. Fig. 6.9, Fig. 6.10 and Fig. 6.11 show the sleeve and PM stress distributions when the rotor is operating at high speed and high temperature (120 °C) with Ti-alloy, Al-alloy and plastic pole filler utilized, respectively. Table 6.4 further compares the sleeve and PM stress range for the rotor without pole filler structure and the rotors with the three pole filler materials introduced.

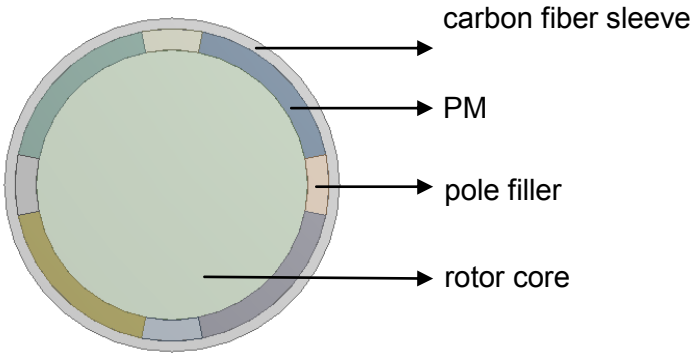

Fig. 6.8. Rotor structure with pole filler.

Table 6.3 Pole filler material mechanical properties

	Density (kg/m^3)	CTE (1/K)	Young's Modulus (GPa)	Poisson's ratio
Ti-alloy	4500	8.8 E-6	105	0.28
Al-alloy	2800	2.3E-5	69	0.32
Plastic	1300	3.2E-5	12	0.34

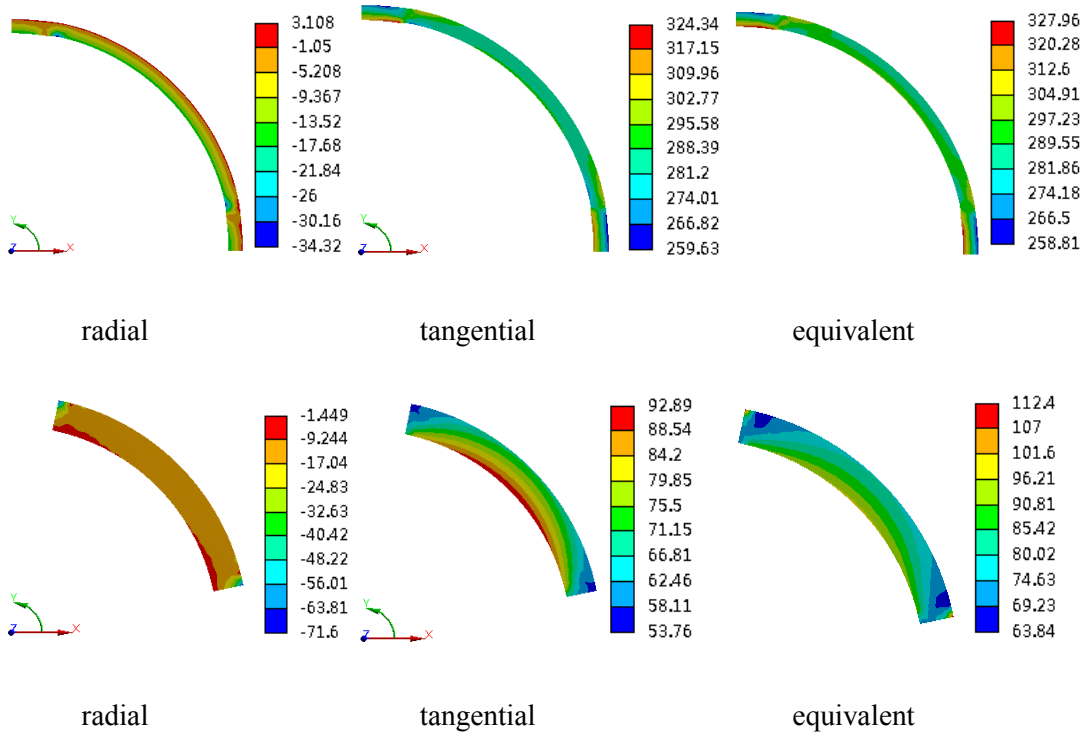

Fig. 6.9. Sleeve and PM stress distributions for rotor with a Ti-alloy pole filler (Unit: MPa).

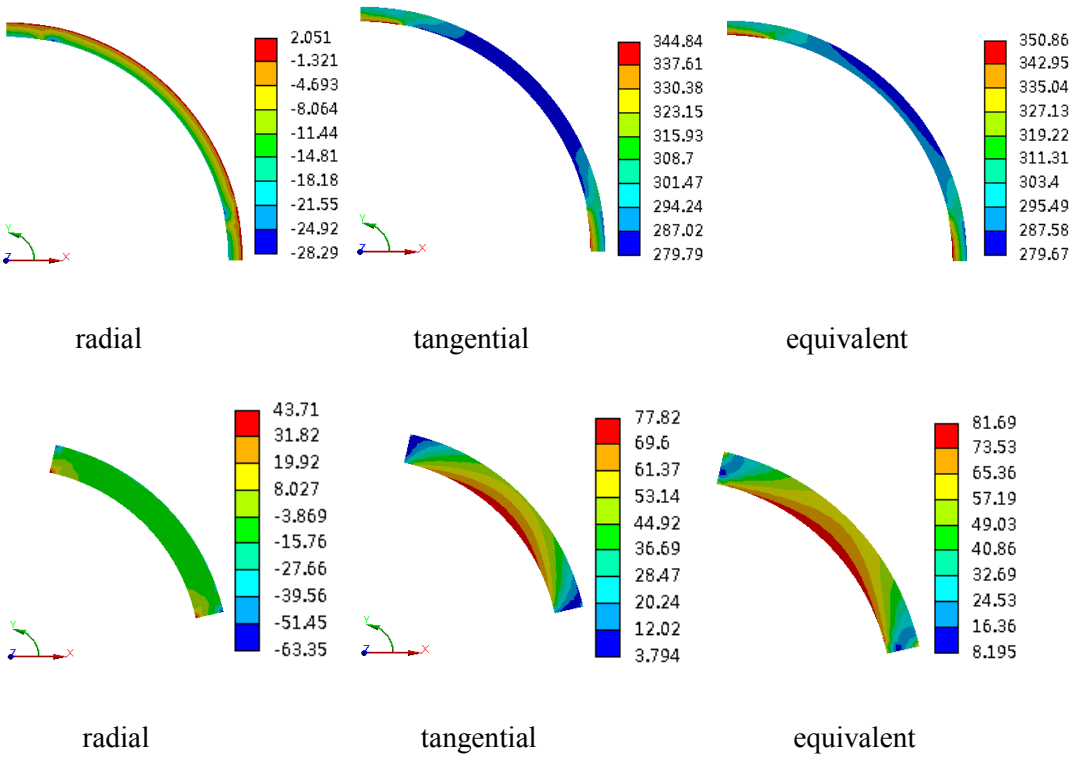

Fig. 6.10. Sleeve and PM stress distributions for a rotor with Al-alloy pole filler (Unit: MPa).

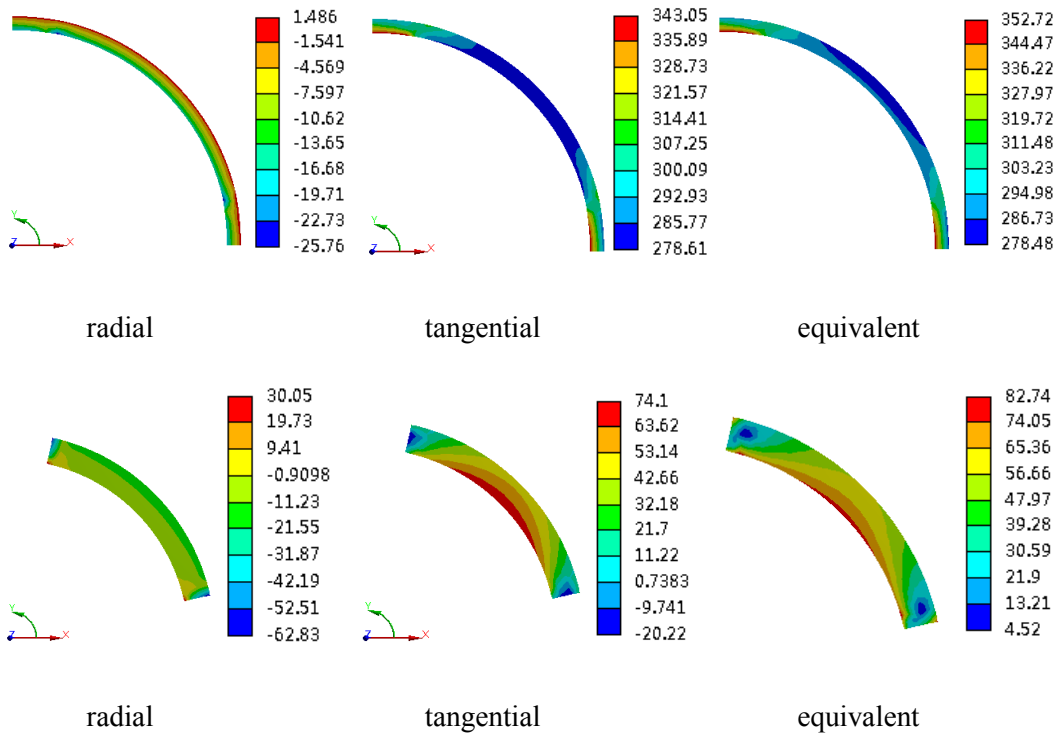

Fig. 6.11. Sleeve and PM stress distributions for a rotor with plastic pole filler (Unit: MPa).

Table 6.4 Sleeve and PM stress range (Unit: MPa)

	Sleeve stress		PM stress	
	radial	tangential	radial	tangential
No pole filler	-53.7-11.5	8.7-478.8	-111.9-1.1	-22.7-64.5
Ti-alloy pole filler	-34.3-3.1	259.6-324.3	-71.6— -1.5	53.8-92.9
Al-alloy pole filler	-28.3-2.1	279.8-344.8	-63.4-43.7	3.8-77.8
Plastic pole filler	-25.8-1.5	278.6-343.1	-62.8-30.1	-20.2-74.1

It can be seen that when the rotor is operating at high speed and high temperature, the sleeve maximum tangential stress is 478.8 MPa for a rotor without the pole filler structure; while it reduces to 324.3 MPa for a rotor with Ti-alloy pole filler, and 344.8 MPa and 343.1 MPa for rotors with Al-alloy and plastic filler, respectively. Therefore, using pole filler rotor structures dramatically reduces the maximum

equivalent stress on the sleeve, hence reducing the risk of sleeve damage. The Ti - alloy pole filler rotor is shown to give the least tangential and equivalent sleeve stress by FEM. In addition, the added pole filler material is also found to have an impact on the PM tensile stress due to thermal expansion. The PM maximum tangential tensile stress of a Ti-alloy pole filler rotor can increase by up to 92.9 MPa, which is greater than the PM permitted stress range. The sleeve and PM stress for the Al-alloy filler rotor approaches that of the carbon fiber one as the CTE of the two materials are quite similar. Considering that the carbon fiber sleeve has low thermal conductivity, the plastic pole filler is chosen in this study as there are almost no eddy current losses in the plastic material due to its low electrical conductivity.

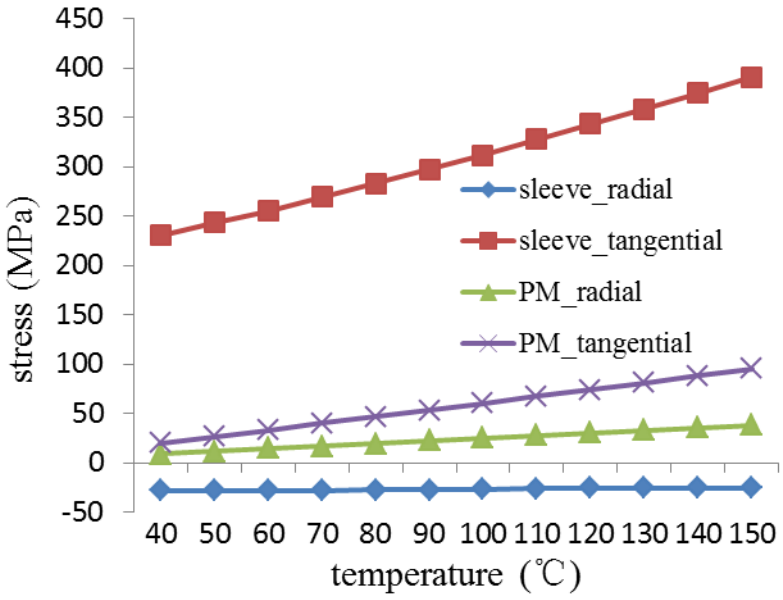

Fig. 6.12. Sleeve and PM radial and tangential stresses as a function of rotor temperature.

Fig. 6.12 presents the variation in sleeve and PM radial and tangential stress with operational temperature for the plastic-pole filler rotor given in Fig. 6.8. It can be seen that although rotor sleeve radial stress is not impacted by temperature, sleeve tangential stress is quite sensitive to the rotor operating temperature: the maximum sleeve tangential stress is 235 MPa at 40 °C. This nearly doubles in value (402 MPa) if the temperature increases to 150 °C. As for the PMs, their radial and tangential stresses are also observed to increase with temperature, with the PM tangential stress

remaining below the permitted stress if the rotor operating temperature does not exceed 130 °C.

6.3.3 Effects of rotor sleeve thickness and interference

Interference fitting is normally utilized for PM binding in HSPMMs for rotor mechanical assembly, with the rotor operational stress adjusted through the assembling interference provided by the carbon fiber sleeve. This section discusses the impacts of interference on HSPMM rotor strength as sleeve thickness is varied.

Sleeve tangential stress is much greater than radial stress; hence, Fig. 6.13 shows the sleeve tangential stress, and the PM radial and tangential stresses as functions of sleeve thicknesses and interferences for a carbon-fiber-sleeved rotor with plastic pole filler. In the analysis, the HSPMM rotor is set at an operating temperature of 120 °C. The sleeve thickness is varied from 1mm to 6 mm and the interference is varied from 0mm to 0.16 mm in the analysis.

From Fig.6.13 (a), it can be observed that the rotor sleeve tangential stress is greatly increased with rising interference, while the sleeve stress only shows a slight decrease with sleeve thickness: hence, increasing sleeve thickness has little impact with regard to alleviating the stress experienced by the rotor sleeve. The peak sleeve stress occurs when the rotor sleeve thickness is 1 mm and 0.16 mm interference fit assembly is employed. Both PM radial and tangential stresses are reduced by employing a thicker sleeve and larger interference. Thus, it can be concluded that increasing the sleeve interference is helpful for mitigating PM stress, but it does so at the expense of increasing sleeve tangential stress; hence a balance should be struck. It is also noticeable that for the rotor with 1mm-thickness sleeve, the PM radial and tangential stresses are reduced by 7.9% (from 84.3 MPa to 77.6 MPa) and 2.6% (from 80.9 MPa to 78.8 MPa), respectively, as the interference varies from 0 mm to 0.16 mm; while for a 6mm-thickness sleeve rotor, the PM radial and tangential stresses are reduced by up to 69.8% (from 73.4 MPa to 22.2 MPa) and 10.3% (from 78.8 MPa to 70.7 MPa), respectively. Therefore, the PM stress reduction achievable with interference is dependent on the rotor sleeve thickness, hence sleeve thickness and assembly interference should be collectively considered in mechanical design of HSPMMs.

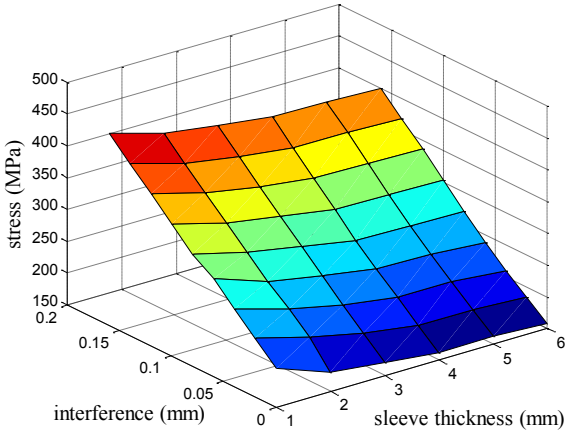

(a) sleeve tangential stress

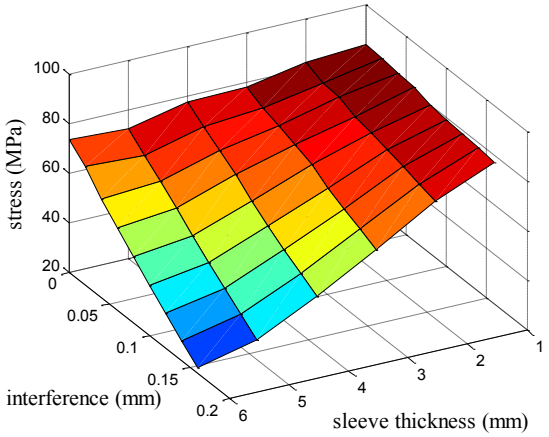

(b) PM radial stress

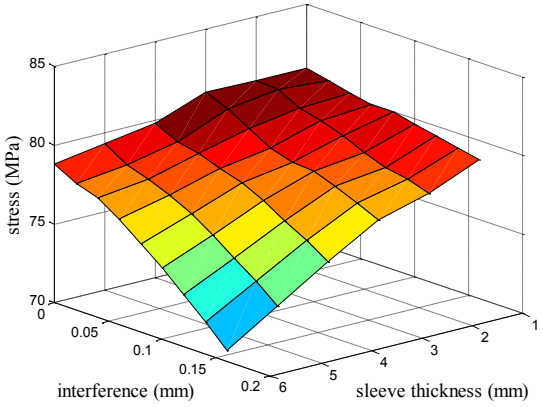

(C) PM tangential stress

Fig. 6.13. Sleeve and PM stress for a HSPMM rotor rotating at high speed.

6.4 Rotor dynamic analysis for HSPMMs

Rotor dynamic performance is another issue that should be considered in high speed machine mechanical design. In rotor dynamics, if the HSPMM rotor rotational frequency is synchronised with the rotor natural frequency, then rotor resonance will occur. The rotating speeds that correspond to these resonance frequencies are called critical speeds. As HSPMMs operate at very high speeds, it is critical to make sure that machine operational speeds are kept away from the critical speeds; otherwise, resonance may result in intensive machine vibration and excessive acoustic noise emission problems. Therefore, an accurate estimation of rotor critical speeds is important and necessary in machine design, particularly for high speed applications.

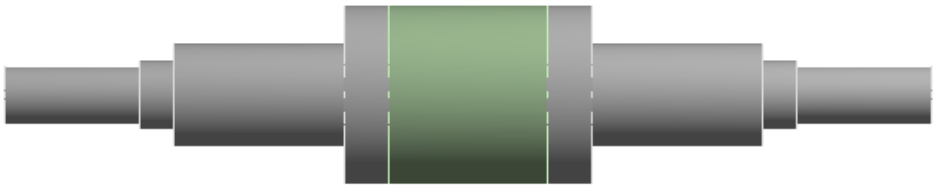

Fig. 6.14. Rotor model.

Table 6.5 Rotor natural frequencies and critical speeds

	First order	Second order	Third order	Fourth order
Natural frequency(Hz)	428	849	1156	1573
Critical speed(rpm)	25680	50940	69360	94380

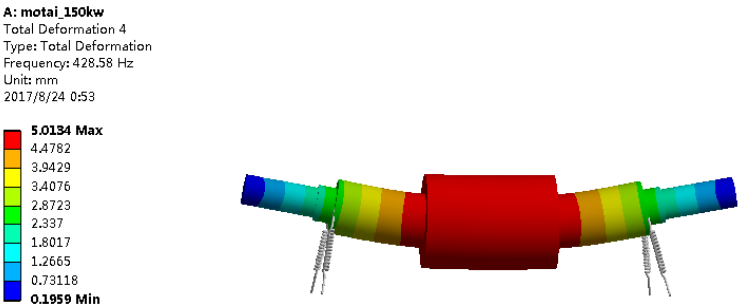

(a) First order

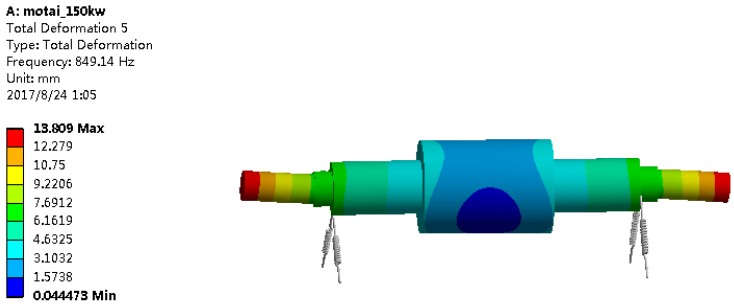

(b) Second order

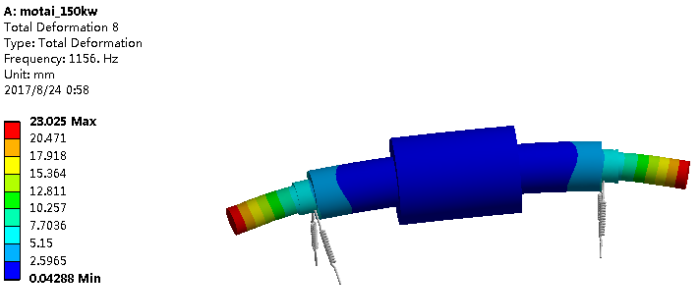

(c) Third order

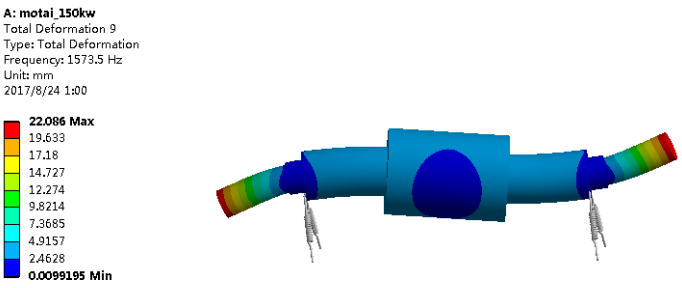

(d) Fourth order

Fig. 6.15. Rotor modal results.

A three-dimensional FEM rotor dynamics analysis was carried out in this study to calculate the rotor critical speeds. FEM software Ansys is utilized due to its friendly user-oriented environment. At first, a rotor with shaft is modelled, while Fig. 6.14 presents the dynamic model for the designed HSPMM rotor. Suitable conditions are applied on the rotor model, while the behaviour of the bearings supporting the rotor are represented by springs with stiffness in the simulation. Table 6.5 lists the rotor natural frequencies and speeds, while Fig. 6.15 shows the first to fourth order rotor modes. It can be seen that the rotor first order natural frequency is 428 Hz corresponding to a critical speed of 25,680 rpm. As the rotor rated operating speed is 17,000 rpm, the designed rotor ensures that the operating range of the machine is well away from the critical speeds.

6.5 Conclusions

In this chapter, rotor mechanical issues have been investigated in the context of HSPMM design. Initially, the rotor is studied and illustrated using thick-walled cylinder elasticity theory, A FEM model is also developed in this study for rotor strength analysis and verified by an analytical method. Then rotor strength is researched for different rotor sleeve materials and operational temperatures; As a means of reducing the sleeve operational stress, three materials acting as pole fillers are comparatively studied, with a plastic pole filler selected for a more detailed study of rotor strength performance with varying temperature. It is found that sleeve stress can be effectively reduced using the pole filler structure; due to thermal expansion, the pole filler material needs to be chosen taking into consideration PM operational stress. The impacts of sleeve thickness and assembly interference have also been studied. It is found that the rotor sleeve thickness has little effect on sleeve stress, and that increasing the interference helps to mitigate the PM stress, but at the same time presents challenges for sleeve mechanical strength. PM stress reduction through increased interference must also take account of the rotor sleeve thickness. Rotor dynamic analysis was carried out using a 3D calculation model, and this verified that the HSPMM rated operational speed is kept well away from the critical speeds of the designed rotor.

Chapter 7
Conclusions and future work

7.1 Conclusions

High speed permanent magnet machines (HSPMMs) are widely accepted and utilized in industrial applications due to their advantages of high power density and compact size. Compared to conventional speed permanent magnet machines, HSPMM power loss density is much greater, while machine thermal dissipation is more challenging due to the small machine size, hence, effective machine thermal dissipation and cooling methods are the key issues in HSPMM design. HSPMM mechanical rotor strength and dynamics also restrict HSPMM development in terms of the maximum rotational speed that can be achieved. Hence, HSPMM design requires careful consideration and analysis of electromagnetic-thermal-mechanical coupling impacts on machine performance. In this dissertation, to illustrate HSPMM design methodology, a 150 kW, 17,000 rpm HSPMM is comprehensively and

systematically researched. This includes the HSPMM design characteristics and process; electromagnetic analysis with a focus on machine power loss analysis; thermal field analysis with the machine cooling method considered and machine rotor mechanical strength and dynamics research. Using a combination of analytical calculation, FEM analysis and experimental verification, various research results were obtained which can be summarised as follows:

(1) A detailed HSPMM design process has been illustrated with rotor components, material and configurations considered; six different slot-pole machine structures are comparatively studied by FEM with regard to machine performance metrics, including cogging torque, back EMF and losses.

- HSPMM on-load torque is not greatly impacted by machine slot/pole combinations.

- Rotor eddy current loss distributions on rotor components vary due to machine stator slot number variation, and a multi-slot stator structure is shown to be beneficial in reducing the total rotor eddy current loss in HSPMMs.

- The role of PM pole arc pole pitch in machine performance improvement is also investigated. Results show that pole arc pole pitch should be selected in order to achieve a balance between the fundamental amplitude and THD in the generated EMF.

(2) HSPMM iron loss is estimated by an improved method involving the machine iron core magnetic flux density waveform, and incorporating harmonics and rotational magnetic field components to achieve high precision. The HSPMM air gap flux density distribution is analytically calculated with machine stator slot opening effects included, and its effectiveness is verified by comparison with FEM calculation results.

HSPMM rotor eddy current loss is comprehensively investigated for different machine configurations using FEM analysis.

- As sleeve conductivity is increased, rotor eddy current loss initially rises and then declines, due to the fact that eddy current loss is determined by both eddy current amplitude and distribution area.

- A composite rotor structure, involving a copper shielding inserted between the sleeve and PMs, is investigated as a means of reducing eddy current loss in PMs for rotors with either stainless steel or carbon fiber sleeves. The impact of the composite rotor structure on rotor total eddy current loss is shown to be dependent on the sleeve material used. With copper shielding thickness increasing, the total eddy current loss in a carbon-fiber-sleeve rotor increases when compared to the same rotor without copper shielding, while in a stainless-steel-sleeve rotor, the opposite trend is observed.

- The impact on rotor eddy current loss of varying stator slotting length and air gap length, is also explored, revealing that it is beneficial to shorten the slot opening width and increase machine air gap length, but challenges for the machine manufacturing process and mechanical issues should also be considered to strike a balance.

- A PM bevelling method is proposed as an effective way to reduce the rotor eddy current loss, and it is shown that this can be achieved with little effect on machine output performance.

Rotor air frictional loss has been investigated by fluid field analysis. This has shown that

- HSPMM air frictional loss dramatically increases with rotor speed.

- A smooth rotor surface is desirable to reduce machine rotor air frictional loss.

- A suitable forced cooling air speed should be chosen for the HSPMM cooling system.

(3) Based on the fluid and thermal characteristics of the machine, the HSPMM temperature distribution is investigated and analysed using the established 3-D fluid–thermal coupling CFD modelling technique with the calculated machine power losses as heat sources. The HSPMM thermal CFD modelling method is illustrated and detailed; then effects of cooling air velocity, rotor eddy current loss and carbon fiber thermal conductivity on HSPMM thermal performance are studied. It is concluded that:

- Increasing forced cooling air speed reduces the temperature of HSPMM components, however, there are diminishing returns with increasing speed due to the extra machine air frictional loss induced.

- The maximum temperature of the rotor increases approximately linearly with rotor eddy current loss, while the impact on machine stator and winding temperatures is negligible due to the low thermal conductivity of the air flow.

- The rotor sleeve material for HSPMM should be carefully chosen with high thermal conductivity a desirable characteristic.

(4) High speed rotor strength is investigated analytically using elasticity theory with the rotor modelled as a thick-walled cylinder, while the rotor strength FEM model can also be verified by analytical method.

- The rotor mechanical strength is analysed with regard to sleeve material and operational temperature; in order to reduce sleeve stress, three materials (Ti alloy, Al alloy and plastic) acting as pole filler are comparatively studied. It is found that the pole filler structure with the three materials can effectively reduce machine sleeve stress when the rotor is in high speed operation.

- Moreover, pole filler material is also found to have an impact on PM tensile stress due to thermal expansion. The plastic is deemed to be the optimum choice.

- Machine rotor stress variation due to operational temperature is also studied. It is found that sleeve tangential stress dramatically increases with increasing temperature.

- Rotor stress with sleeve thickness and interference variation is also comprehensively studied revealing that increasing sleeve interference is able to mitigate PM stress, while it also results in an increase in sleeve tangential stress. Increasing sleeve thickness has little impact on sleeve stress. However, PM stress reduction through increasing interference is dependent on rotor sleeve thickness, hence, the sleeve thickness and interference fit assembly should be considered together in HSPMM mechanical design.

- FEM is also utilized to study HSPMM rotor dynamics demonstrating that HSPMM operational speed is far away from the critical speeds with the designed rotor.

7.2 Future work

HSPMM electromagnetic, thermal and mechanical issues are comprehensively investigated and researched in this dissertation. Future works can focus on the consideration of improving HSPMM performance and application in industrial areas. Several recommendations on possible future work are listed as follows:

HSPMM optimization algorithm

HSPMM design is complicated work with machine electromagnetic performance closely related to machine parameters. Hence, optimization algorithms for HSPMM can be developed and employed in HSPMM design for machine electromagnet performance improvement. Moreover, optimization algorithms can also be proposed to optimise machine thermal performance in order to achieve a more reasonable machine temperature distribution by selecting suitable machine structure parameters. The highest temperatures of machine components can be chosen as the objective parameters in machine thermal optimization.

HSPMM cooling system design

Machine thermal performance is a major subject in HSPMM research, with an effective cooling system always desired for HSPMM drive systems. Electrical machine cooling methods include setting jacket cooling, introducing axial ducts in the winding region for cooling, and so on. These cooling methods have their own characteristics, which need to be applied for HSPMMs based on specific cases. Moreover, rotor temperature rise is the main challenge for HSPMMs; cooling systems for rotors should therefore be further researched to limit rotor temperature in high speed operation.

HSPMM control method

Advanced control methods can be applied in HSPMM drives. Research can be carried out for HSPMM drives on aspects such as novel machine sensorless control schemes and improving current dynamics. It is worth mentioning that sensorless

control is a hot topic in permanent magnet machine drive research with methods based on model reference adaptive system, [145], high frequency injection [146], and sliding mode observer methods [147]-[150]. Some of the approaches are already being considered with a focus on robustness and fast dynamic response.

HSPMM acoustic noise analysis

HSPMM acoustic noise analysis is also regarded as a promising research direction for HSPMMs. The noise of electrical machines usually comes from mechanical, aerodynamics and electromagnetic sources. Machine acoustic noise can be further investigated from the perspectives such as machine structure, saturation and manufacturing.

References

[1] D. Gerada, A. Mebarki, N. Brown, C. Gerada, A. Cavagnino, A. Boglietti. (2014) "High speed electrical Machines: Technologies, Trends, and Developments", IEEE transactions on industrial electronics, Vol. 61, no. 6, pp.2946- 2959.

[2] N. Bianchi, S. Bolognani, and F. Luise. (2004) "Potentials and limits of high speed PM motors," IEEE transactions on industrial applications, Vol. 40, no. 6, pp. 1570.

[3] S. Jang, H. Cho, and S. Choi. (2007) "Design and analysis of a high speed brushless DC motor for centrifugal compressor," IEEE transactions on magnetics, Vol. 43, no.6, pp. 2573-2575.

[4] K. Yamazaki, A. Suzuki and M. Ohto. (2012) "Harmonic loss and torque analysis of high speed induction motors," IEEE transactions on industry applications, Vol.48,no. 3,pp.933-941.

[5] A. Nagorny, R. Jansen and D. Kankam, "Experimental performance evaluation of a high speed permanent magnet synchronous motor and drive for a flywheel at different frequencies," 17th international conference on electric machines, Greece: IEEE: pp.1-6.

[6] C. Huynh, L. Zheng and P. McMullen (2007) "Thermal performance evaluation of a high speed flywheel energy storage system," 33th annual conference of the IEEE industrial electronics society, Taibei: IEEE: 163-168.

[7] W. Soong, G. Kliman and R. Johnson. (2000) "Novel high speed induction motor for a commercial centrifugal compressor," IEEE transactions on industrial applications, Vol.36, no.3, pp. 706-713.

[8] S. Jang, H. Cho and J. Vhoi. (2005) "Development of high speed brushless DC motor for turbo-compressor," 8th international conference on electrical machines and systems, Nanjing, China: IEEE: 877-882.

[9] D. Hong. J. Choi and D. Kim. (2013) "Development of a high speed induction motor for spindle systems," IEEE transactions on magnetics, Vol.49, no.7, pp. 4088-4091.

[10] A. Tenconi, S. Vaschetto and A. Vigliani. (2014) "Electrical machines for high speed applications: design considerations and tradeoffs," IEEE transactions on industrial electronics, Vol.61, No.6, pp.3022-3029.

[11] S. Kim, Y. Kim and G. Lee. (2012) "A novel rotor configuration and experimental verification of interior PM synchronous motor for high speed applications," IEEE transactions on magnetics, Vol. 48, No.2, pp. 843-846.

[12] D. Gerada, K. Bradley and C. Gerada. (2011) "Design aspects of high speed high power density laminated rotor induction machines," IEEE transactions on industrial electronics, Vol.58, no. 9, pp. 4039-4067.

[13] A. Boglietti, A. Cavagnino and A. Tenconi. (2010) "Key design aspects of Electrical machines of high speed spindle applications," 36th Annual conference on industrial electronics society, Glendale, USA: IEEE: 1735-1740.

[14] Z. Kolondzovski, P.Sallinen and A. Arkkio. (2010) " Thermal analysis of a high speed PM machine using num and thermal network method," 2010 XIX internal conference on electrical machines, Rome, Italy: IEEE:1-6.

[15] A. Darbyshire, (2010) "Mechanical Engineering", Routledge Publications, Inc., Oxford, UK, ISBN-10 0080965776.

[16] J. Saari. (1998) "Thermal analysis of high speed induction machines", Acta Polytechnica Scandiavica, Electrical engineering series, No. 90, Helsinki, Finnish Academy of Technology.

[17] Q. He, H. Liu and Y. Zhang. (2009) "The characteristics of high hybrid ceramic ball bearings for high speed spindle," 2009 IEEE international conference on mechatronics and automation, Changchun, China: IEEE: 2489-2494.

[18] T. Waumans, C.Zwyssig and J.Peris. (2011) "High speed electrical motor/generator supported by air bearings," 11th international workshop on Micro and nanotechnology for power generation and energy conversion applications, Seoul, Korea: 458-461.

[19] K. Lee, Y. Ho and D. Koo. (2006) "Development of a radical active magnetic bearing for high speed turbo-machinery motors", SICE- ICASE international joint conference, Busan, Korea: 1543-1548.

[20] D. Papaoikonomou, M. VanderGeest. (2014) "Comparison between induction and PM machine for high speed starter-generator applications", 7th IET international conference on power electronics, machines and drives, Manchester, UK: IET 1-6.

[21] J. Gieras, J. Saari. (2012) "Performance calculation for a high speed solid rotor induction motor", IEEE transactions on industrial electronics, Vol. 59, no. 6, pp.2689-2700.

[22] M. Ahrens, U. Bikle and R. Gottkehaskamp (2002) "Electrical design of high speed induction motors of up to 15 MW and 20 000 rpm", International conference on power electronics, machines and drives, UK: IET 381-386.

[23] D. Popa, D.Fodorean (2014) "Design and performances evaluation of a high speed induction motor used for the propulsion of an electrical vehicle", 2014 international symposium on power electronics, electrical drives, automation and motion, Ischia, Italy: IEEE 88-93.

[24] D. Gerada, A. Mebarki and N. Brown (2012) "Design modelling and testing of a high speed induction machine drive", 2012 IEEE energy conversion congress and exposition, Raleigh, NC: IEEE 4649-4655.

[25] Y. Gessese, A. Binder and B. Funiero (2010) "Analysis of the effect of radical rotor surface grooves on rotor losses of high speed solid rotor induction motor",

International symposium on power electronics electrical drives automation and motion, Pisa, Italy: IEEE 1762-1767.

[26] M. Dems, K. Komeza (2014) "Performance characteristics of a high speed energy saving induction motor with an amorphous stator core", IEEE transactions on industrial electronics, Vol. 61, no. 6, pp.3046- 3055.

[27] R. Lateb, J. Enon and L.durantay (2009) "High speed high power electrical induction motor technologies for integrated compressors", 2009 international conference on electrical machines and systems, Tokyo, Japan: IEEE 1-5.

[28] M. Caprio, V. Lelos and J. Herbst (2005) "Advanced induction motor end-ring design features for high speed applications", 2005 international conference on electric machines and drives, San Antotio, USA: IEEE 993-998.

[29] L. Papini, C. Gerada and D.Gerada (2014) "High speed solid rotor induction machine: Analysis and performances", 17th international conference on electrical machines and systems, Hangzhou, China: IEEE 2759-2765.

[30] J. Bumby, E. Spooner and M. Jagiela (2006) "Equivalent circuit analysis of solid rotor induction machines with reference to turbocharger accelerator applications", IEE elect Power appl, Vol.153, no 3, pp. 31-39.

[31] T. Mauffrey, J. Pradurat and L. Durantay (2013) "Comparison of 5 different squirrel cage rotor designs for large high speed induction motors", 2013 conference record PCIC Europe, Istanbul, Turkey: IEEE 1-9.

[32] W. Ding, L. Liu and J. Lou (2013) " Design and control of a high speed switched reluctance machine with conical magnetic bearings for aircraft application", IET on electric power applications, Vol. 7, no 3, pp. 179-190.

[33] J. Kim, R. Krishnan (2008) " High efficiency single-pulse controlled switched reluctance motor drive for high speed (48k rpm) application: analysis, design and experimental verification", 2008 IEEE industry applications society annual meeting, Edmonton, Alta: IEEE:1-8.

[34] L. Morel, H. Fayard and R. VivesFos (2000) " Study of ultra high speed switched reluctance motor drive", 2000 IEEE industry applications conference, Rome, Italy: IEEE 87-92.

[35] Q. Zhou, C. Liu and X. Zhu (2009) " Design of super high speed switched reluctance machine", Proceedings of the CSEE, Vol. 29, no. 9, pp.87- 92.

[36] J. Dang, J.Mayor and S. Semidey (2015) "Practical considerations for the design and construction of a high speed SRM with a flux bridge rotor", IEEE transactions on industrial applications, Vol. 51, no. 6, pp.4515- 4520.

[37] S. Won, J. Choi and J. Lee (2008) " Windage loss reduction of high speed SRM using rotor magnetic saturation", IEEE transactions on magnetics, Vol. 44, no. 11, pp.4147-4150.

[38] C. Bateman, B. Mecrow, and A. Clothier (2009) " Sensorless operation of an ultra high-speed switched reluctance machine", 2009 IEEE energy conversion congress and exposition, San Jose, CA: IEEE: 3992-3999.

[39] Q. Ma, W. Liang and F. Ferreira (2014) "Improved flux linkage method for position sensorless control of high-speed SRM", 2014 international conference on electrical machines, Berlin, German: IEEE: 783-788.

[40] C. Bateman, B. Mecrow, and A. Clothier (2010) " Sensorless operation of an ultra-high-speed switched reluctance machine", IEEE transactions on industry applications, Vol. 46, no. 6, pp.2329- 42337.

[41] S. Mariokov, B. Jager (2015) "Control of a high-speed switched reluctance machine using only DC-link measurements", 2015 IEEE international conference on industrial technology, Seville, Spain: IEEE: 677-682.

[42] TurboPower Inc, [Online]. Available:

http://turbopowersystems.com/why-us/efficiency-power-generation/

[43] ABBInc,[Online].Available:

http://www.abb.com/cawp/seitp202/1f7082049eb90e33c1257c19003a8952.aspx

[44] D. Gerada, A. Mebarki, R.P. Mokbadar and C. Gerada (2009) "Design issues of high speed permanent magnet machines for high temperature applications" 2009 international electric machines and drives conference, Miami, USA: IEEE: 1036-1042.

[45] L. Papini, T. Raminosoa, D. Gerada and C. Gerada (2014) "A high speed permanent magnet machine for fault-tolerant drivetrains", IEEE transactions on industrial electronics, Vol. 61. No.6, pp. 3071-3080.

[46] H. Zhang, X. Zhang, C.Gerada, M. Gelea and D. Gerada (2015) "Design considerations for the tooth shoe shape for high-speed permanent magnet generators", IEEE transactions on magnetics, Vol. 51. No.11, Article # 8112904.

[47] H. Zhang, X. Zhang, C. Gerada and J. Li (2015) "Optimization on the tooth top shape of a high speed permanent magnetic generator", 2015 IEEE magnetics conference, Beijing, China: IEEE: 1.

[48] N. Bernard, L. Dang and J. Olivier (2015) " Design optimizations of high-speed PMSM for electric vehicles", 2015 IEEE vehicle power and propulsion conference, Montreal, Canada: IEEE: 19-22.

[49] N. Bernard, R. Missoum and L. Dang (2016) "Design methodology for high speed permanent magnet synchronous machines", IEEE transactions on energy conversion, Vol. PP. No.99, pp.1-9.

[50] C. Zwyssig, M. Duerr, D. Hassler and J. W. Kolar (2007) " An ultra-high-speed 500 000 rpm, 1 kW electrical drive system", 2007 Power conversion conference, Nogoya, Japan: IEEE: 1577-1583.

[51] J. Loumi, C. Zwyssig, A. Losser and J. Kolar (2009) " Efficiency optimization of a 100-W 500 000 r/min permanent-magnet machine including air friction losses" IEEE transactions on industry applications, Vol. 45, No.4, pp.1368- 1377.

[52] G. Munteanu, A. Binder, T. Schneider and B. Funier (2010) " No load tests of a 40 kW high speed bearingless permanent magnet synchronous motor" 2010 International symposium on power electronics electrical drives automation and motion, Pisa, Italy: IEEE: 1460-1465.

[53] G. Munteanu, A. Binder and T. Schneider (2011) "Loss measurement of a 40 kW high speed bearingless PM synchronous motor" 2011 IEEE energy conversion congress and exposition, Phoenix ,USA: IEEE: 722-729.

[54] T. Schneider, J. Petersen and A. Binder (2008) " Influence of pole pair combinations on high speed bearingless permanent magnet motor performance", 4th IET conference on power electronics, machines and drives, York, UK: IET: 707-711.

[55] A. Binder, T. Schneider and M. Klohr (2006) "Fixation of buried and surface-mounted magnets in high-speed permanent-magnet synchronous machines" IEEE transactions on industry applications, Vol.42, No. 4, pp.1031-1037.

[56] S. Jang, H. Cho and S. Choi (2007) " Design and analysis of a high speed brushless DC motor for centrifugal compressor", IEEE transactions on magnetics, Vol. 43, No.6, pp. 2573-2575.

[57] S. Jang, K. Ko, H. Cho and J. Choi (2007) " Characteristic analysis of a 2 kW high speed permanent magnet synchronous generator using the equivalent circuit method", 2007 international conference on electrical machines and systems, Seoul, Korea: IEEE: 868-873.

[58] F. Luise, A. Tessarolo, F. Agnolet and S. Pieri (2014) " A high-performance 640 kW 10 000 rpm Halbach array PM slotless motor with active magnetic bearings. Part Ⅰ: Preliminary and detailed design", 2014 international symposium on power electronics, electrical drives, automation and motion, Ischia, Italy: IEEE: 1237-1244.

[59] F. Luise, A. Tessarolo, F. Agnolet and S. Pieri (2014) " A high-performance 640 kW 10 000 rpm Halbach-array PM slotless motor with active magnetic bearings. Part Ⅱ: Manufacturing and testing", 2014 international symposium on power electronics, electrical drives, automation and motion, Ischia, Italy: IEEE: 1245-1250.

[60] N. Bianchi, S. Bolognani and F. Luise (2005) "Analysis and design of a PM brushless motor for high speed operations", IEEE transactions on energy conversion, Vol.20, No.3, pp. 629-637.

[61] N. Bianchi, S. Bolognani and F. Luise (2006) "High speed drive using a slotless PM motor", IEEE transactions on power electronics, Vol. 21, No.4, pp. 1083-1090.

[62] F. Wang, D. Zhang, J. Xing and Y. Xu (2009) " Study on air friction loss of high speed PM machine", 2009 IEEE conference on industrial technology, Gippsland, Australia: IEEE: 1-4.

[63] F. Wang, X. Xu, X. Kong and D. Zhang (2009) "Study on core loss of high speed PM machine", 2009 IEEE conference on industrial technology, Gippsland, Australia: IEEE: 1-4.

[64] X. Kong, F. Wang and J. Xing (2012) "Losses calculation and temperature field analysis of high speed permanent magnet machines", Transactions of China electro-technical society, Vol. 27, No.9, pp. 166-173.

[65] X. Kong, F. Wang and J. Xing (2011) "Temperature rise calculation of high speed PM machine based on thermal-circuit method and 3D fluid field method", 2011 international conference on electrical machines and systems, Beijing, China: IEEE: 1-5.

[66] T. Wang, F. Wang, H. Bai and H. Cui (2008) "Stiffness and critical speed calculation of magnetic bearing-rotor system based on FEM" 2008 international conference on electrical machines and systems, Wuhan, China: IEEE: 575-578.

[67] T. Wang, F. Wang, H. Bai and J. Xing (2007) "Optimization design of rotor structure for high speed permanent magnet machines", 2007 international conference on electrical machines and systems, Seoul, Korea: IEEE:1438-1442.

[68] J. Xing, F. Wang, T. Wang and Y. Zhang (2010) "Study on anti-demagnetization of magnet for high speed permanent magnet machine", IEEE transactions on applied superconductivity, Vol. 20, No. 3, pp. 856-860.

[69] X. Kong, F. Wang, Y. Xu and J. Xing (2010) "Analysis and calculation of iron losses of high speed permanent magnet machines", Electrical machines and control, Vol. 14, No.9, pp.26-30.

[70] J. Daesuk, D. Hong, B. Woo and Y. Jeong (2012) " Iron loss of 50W, 100 000 rpm permanent-magnet machine in micro gas turbine", 6th international conference on electromagnetic field problems and application, Dalian, China: IEEE: pp. 1-4.

[71] J. Shen, P. Li and H. Hao (2013) "Study on electromagnetic losses in high-speed permanent magnet brushless machines- the state of the art", Proceedings of the CSEE, Vol. 33, No.3, pp. 62-74.

[72] Jiang S. High speed permanent magnet synchronous motor loss analysis and temperature field calculation [D]. Harbin: Harbin institute of technology, 2010.

[73] Y. Xu, F. Wang (2008) "Experiment study on magnetizing and loss characteristics of electrical strip for different frequencies", 11th international conference on electrical machines and systems, Wuhan, China: IEEE: 156-159.

[74] G. Bertotti (1988), "General properties of power losses in soft ferromagnetic materials", IEEE transactions on magnetics, Vol. 24, No. 1, pp. 621-630.

[75] Z. Cheng, N. Takahashi, and B. Forghani (2014), "Modeling of magnetic properties of GO Electrical steel based on Epstein combination and loss data weighted processing", IEEE transactions on magnetics, Vol. 50, No. 1, #6300209.

[76] M. Ranlof, A. Wolfbrandt and J. Lidenholm (2009), "Core loss prediction in large hydropower generator: influence of rotating fields", IEEE transactions on magnetics, Vol. 45, No. 8, pp. 3200-3206.

[77] J. Zhu and V. Ramsden (1998), "Improved formulations for rotational core losses in rotational electrical machines", IEEE transactions on magnetics, Vol. 34, No. 4,pp.2234-2242.

[78] L. Ma, M. Sanada and S. Morimoto (2003), "Prediction of iron loss in rotating machines with rotational loss induced", IEEE transactions on magnetics, Vol. 39, No. 4, pp. 2036-2041.

[79] J. Seo, T. Chung and C. Lee (2009),"Harmonic iron loss analysis of electrical machines for high-speed operation considering driving condition", IEEE transactions on magnetics, Vol. 45, No. 10, pp. 4656-4659.

[80] J. Seo, S. Kwak and S. Jung (2009),"A research on iron loss of IPMSM with a fractional number of slot per pole", IEEE transactions on magnetics, Vol. 45, No.3, pp. 1824-1827.

[81] J. Seo, D. Woo and T. Chung (2010), "A study on loss characteristics of IPMSM for FCEV considering the rotating field", IEEE transactions on magnetics, Vol. 46, No.8, pp. 3213-3216.

[82] Y. Huang, J. Dong, J. Zhu and Y. Guo (2012), " Core loss modelling for permanent magnet motor based on flux variation locus and finite element method", IEEE transactions on magnetics, Vol. 48, No.2, pp. 1023-1026.

[83] R. Fang and R. Wang (2004), "Calculation of iron loss in high speed induction motor fed by non-sinusoidal voltage source based on harmonic analysis method", Electrical machines and control, Vol. 8, No.1, pp.25-27.

[84] K. Yamazaki and Y. Seto (2006), "Iron loss analysis of interior permanent magnet synchronous motors- Variation of main loss factors due to driving condition", IEEE transactions on industry applications, Vol. 42, No.4, pp. 1045-1052.

[85] K. Yamazaki and A. Abe (2009), "Loss investigation of interior permanent magnet motors considering carrier harmonic and magnet eddy currents", IEEE transactions on industry applications, Vol. 45, No.2, pp. 659-665.

[86] J. Zou, S. Jiang and W. Liang (2010), "AC loss in a high speed BLPM motor considering proximity effect", Electric machines and control, Vol. 14, No.5, pp. 49-55.

[87] D. Gonzalez and D. Saban (2014), "Study of the copper losses in a high-speed permanent-magnet machine with form-wound windings", IEEE transactions on industrial electronics, Vol. 61, No.6, pp. 3038-3045.

[88] A. Tessarolo, F. Agnolet and M. Mezzarobba (2012), " Use of time-harmonic finite element analysis to compute stator winding eddy current losses due to rotor motion in furface permanent magnet machines", IEEE transactions on enery conversion, Vol. 27, Vol. 3,pp. 670-679.

[89] S. Iwasaki, P. Deodhar and Y. Liu (2009), "Influence of PWM on the proximity loss in permanent magnet brushless AC machines", IEEE transactions on industry applications, Vol.45, No.4, pp.1359-1367.

[90] M. Popesuc and D. Dorrell (2013), "Proximity losses in the windings of high speed brushless permanent magnet AC motors with single tooth windings and parallel paths", IEEE transactions on magnetics, Vol. 49, No.7, pp. 3913-3916.

[91] O. Drubel and R. Stoll (2001), "Comparison between analytical and numerical methods of calculating tooth ripple losses in salient pole synchronous machines", IEEE transactions on energy conversion, Vol. 16, No.1, pp. 61-67.

[92] K. Atallah, D. Howe and P. Mellor (2000), "Rotor loss in permanent-magnet brushless ac machines", IEEE transactions on industrial applications, Vol. 36, No.6, pp. 1612-1618.

[93] F. Deng (1997), "Commutation caused eddy current losses in permanent magnet brushless DC motors", IEEE transactions on magnetics, Vol. 33, No.5,pp.4310-4318.

[94] Z. Zhu, K. Ng and N. Schofield, (2004), "Improved analytical modelling of rotor eddy current loss in brushless machines equipped with surface-mounted permanent magnets", IEE proceedings of electric power applications, Vol. 151, No.6, pp. 641-650.

[95] D. Ishak, Z. Zhu and D. Howe, (2005), "Eddy-current loss in the rotor magnets of permanent-magnet brushless machines have a fractional number of slots per pole", IEEE transactions on magnetics, Vo. 41, No.9, pp. 2462-2469.

[96] L. Wu, Z. Zhu and D. Staton (2012), "Analytical modeling and analysis of open-circuit magnet loss in surface-mounted permanent-magnet machine", IEEE transactions on magnetics, Vol.48, No.3, pp. 1234-1247.

[97] L. Wu, Z. Zhu and D. Staton (2012), "Analytical model for predicting magnet loss of surface-mounted permanent magnet machines accounting for slotting effect and load", IEEE transactions on magnetics, Vol. 48, No.1, pp. 107-117.

[98] H. Toda, Z. Xia and J. Wang (2004), "Rotor eddy current loss in permanent magent brushless machines", IEEE transactions on magnetics, Vol.40, No.4, pp. 2104-2106.

[99] J. Wang, K.Atallah and R. Chin (2010), "Rotor eddy current loss in permanent-magnet brushless AC machines", IEEE transactions on magnetics, Vol. 46, No.7, pp. 2701-2707.

[100] H. Xuan, D. Lahaye, and H. Polinder (2013), "Influence of stator slotting on the performance of permanent-magnet machines with concentrated windings", IEEE transactions on magnetics, Vol. 49, No.2, pp.929-938.

[101] N. Zhao, Z. Zhu and W. Liu (2011), "Rotor eddy current loss calculation and thermal analysis of permanent magnet motor and generator", IEEE transactions on magnetics, Vol. 47, No.10, pp. 4199-4202.

[102] L. Wu, R. Qu and D. Li (2014), "Reduction of rotor eddy current losses for surface PM machines with fractional slot concentrated windings and retaining sleeve", IEEE transactions on magnetics, Vol. 50,No.11, Articale#:8205704.

[103] G. Choi and T. Jahns (2016), "Reduction of eddy-current losses in fractional-slot concentrated-winding synchronous PM machines", IEEE transactions on magnmetics, Vol.pp, No. 99, pp.1.

[104] S. Niu, S. Ho and W. Fu (2012), "Eddy current reduction in high speed machines and eddy current loss analysis with multislice time-stepping finite-element method", IEEE transactions on magnetics, Vol. 48, No.2, pp. 1007-1010.

[105] J. Li, Y. Xu and J. Zou (2015), "Analysis and reduction of magnet loss by deepening magnets in interior permanent-magnet machines with a pole/slot ratio 2/3", IEEE transactions on magnetics, Vo. 51, No.11, Article#: 8112004.

[106] M. Koo, J. Choi and K. Hong (2015), "Comparative analysis of eddy current loss in permanent magnet synchronous machine considering PM shape and skew effect using 3-D FEA", IEEE transactions on magnetics, Vol.51, No.11,Articale#: 6301104.

[107] K. Yamazaki, Y. Fukushima and M. Sato (2009), "Loss analysis of permanent-magnet motors with concentrated windings-Variation of magnet eddy-current loss due to stator and rotor shapes", IEEE transactions on industry applications, Vol. 45, No.4,pp. 1334-1342.

[108] K. Yamazaki, Y. Kanou and Y. Fukushima (2010), "Reduction of magnet eddy-current loss in interior permanent-magnet motors with concentrated windings", IEEE transactions on industry applications, Vol.46, No.6, pp.2434-2441.

[109] K. Yamazaki, and Y. Kanou (2009), "Rotor loss analysis of interior permanent magnet motors using combination of 2-D and 3-D finite element method", IEEE transactions on magnetics, Vol. 45, No.3,pp. 1772-1775.

[110] Z. Kolondzovski, A. Belahcen and A.Arkkio (2008), "Comparative thermal analysis of different rotor types for a high speed permanent magnet electrical machine", IET electric power applications, Vol. 3, No.4, pp. 279-288.

[111] W. Li, H. Qiu and X. Zhang (2012), "Influence of copper plating on electromagnetic and temperature fields in a high speed permanent magnet generator", IEEE transactions on magnetics, Vol. 48, No.8, pp. 2247-2253.

[112] M. Shah, A.El-Refale (2009), " Eddy-current loss minimization in conducting sleeves of surface PM machine rotors with fractional-slot concentrated armature windings by optimal axial segmentation and copper cladding", IEEE transactions on industry applications, Vol. 45, No.2, pp.720-728.

[113] J. Shen, H. Hao and M. Jin (2013), "Reduction of rotor eddy current loss in high speed PM brushless machines by grooving retaining sleeve", IEEE transactions on magnetics, Vol.49, No.7, pp.3973-3976.

[114] J. Xing, F. Wang, D. Zhang (2010), "Research on rotor air friction loss of high-speed permanent magnet machines", Proceedings of the CSEE, Vol. 30, No.27, pp. 14-19.

[115] J. Dong, Y. Huang and L. Jin (2014), "Review on high speed permanent magnet machines including design and analysis technologies", Proceedings of the CSEE, Vol. 34, No.27, pp. 4640-4653.

[116] B. Guo, Y. Huang J. Dong (2015), "Transient thermal analysis of the conical rotor motor using LPTN and Finite Volume Method", 2015 IEEE conference on magnetics, Beijing, China: IEEE: 1.

[117] P. Ponomarev, M. Polikakarpova and J. Pyrhonen (2012), "Thermal modeling of directly-oil-cooled permanent magnet synchronous machine", 2012 international conference on electrical machines, Marseille, France: IEEE: 1882-1887.

[118] A. Boglietti, A. Cavagnino and D. Staton (2009), "Evaluation and modern approaches for thermal analysis of electrical machine", IEEE transactions on magnetics, Vol.56, No.3, pp.871-882.

[119] C. Kral, A. Haumer and M. Haigis (2009), "Comparison of a CFD analysis and a thermal equivalent circuit model of a TEFC induction machine with measurements", IEEE transactions on magnetics, Vol.24, No.4, pp.809-818.

[120] C. Jungreuthmayer, T. Bauml and O. Winter (2012) "A detailed heat and fluid flow analysis of an internal permanent magnet synchronous machine by means of computational fluid dynamics", IEEE transactions on industrial electronics, Vol. 59, No.12, pp. 4568-4578.

[121] M. Polikarpova, P. Lindh and J. Tapia (2014) "Application of potting material for a 100kW radical flux PMSM", 2014 international conference on electrical machines, Berlin, German, IEEE: 2146-2151.

[122] X. Zhang, W. Li and B. Kou (2015) "Electro-thermal combined optimization on notch in air-cooled high speed permanent-magnet generator", IEEE transactions on magnetics, Vol.51, No.1, Article#: 8200210.

[123] J. Dong, Y. Huang and L. Jin (2014) "Electromagnetic and thermal analysis of open-circuit air cooled high-speed permanent magnet machines with gramme ring windings", IEEE transactions on magnetics, Vol.50, No.11, Article#: 8104004.

[124] H. Cho, K. Ko and J. Choi (2011) "Rotor natural frequencies in high speed permanent-magnet synchronous motor for turbo-compressor application", IEEE transaction on magnetics, Vol.47, No.10, pp. 4258-4261.

[125] Z. Kolondzovski, P. Sallinen and A. Belahcen (2010) "Rotordynamic analysis of different rotor structures for high-speed permanent-magnet electrical machines", IET on electric power applications, Vol.4, No. 7, pp. 516-524.

[126] D. Wang, X. Wang and D. Qiao. (2011) "Reducing cogging torque in surface-mounted permanent magnet motors by nonuniformly distributed teeth method", IEEE transactions on magnetics, Vol. 47, No.9, pp. 2231-2239.

[127] D. Wang, X. Wang and S. Jung. (2013) "Cogging torque minimization and torque ripple suppression in surface-mounted permanent magnet synchronous machines using different magnet widths", IEEE transactions on magnetics, Vol. 49, No.5, pp. 2295-2298.

[128] L. Zhu, S. Jiang and Z. Zhu. (2009) "Analytical methods for minimization cogging torque in permanent magnet machines", IEEE transactions on magnetics, Vol. 45, No.4, pp. 2023-2030.

[129] Y. Yang, X. Wang and R. Zhang (2006) " The optimization of pole arc coefficients to reduce cogging torque in surface-mounted permanent magnet motors", IEEE transactions on magnetics, Vol. 42, No.4, pp. 1135-1138.

[130] D. Dorrell and M. Popescu (2011) "Odd stator slot numbers in brushless DC machines- An aid to cogging torque reduction", IEEE transactions on magnetics, Vol. 47, No.10, pp. 3012-3015.

[131] K. Kim, D. Koo and J. Hong (2007) "A study on the characteristics due to pole arch to pole pitch ratio and saliency to improve torque performance of IPMSM", IEEE transactions on magnetics, Vol. 43, No.6, pp. 2516-2518.

[132] Z. Q. Zhu, S. Ruangsinchaiwanich and N. Schofield (2003) "Reduction of cogging torque in interior magnet brushless machines", IEEE transactions on magnetics, Vol. 39, No.5, pp. 3238-3240.

[133] Z. Q. Zhu, D. Howe and E. Bolte (1993) "Instantaneous magnetic field distribution in brushless permanent magnet DC motors, Part1: open circuit field", IEEE transactions on magnetics, Vol. 29, No.1, pp. 124-135.

[134] Z. Q. Zhu, D. Howe and C. Chan (2002) "Improved analytical model for predicting the magnetic field distribution in brushless permanent magnet machines", IEEE transactions on magnetics, Vol. 38, No.1, pp. 229-238.

[135] Z. Q. Zhu, D. Howe (1993) " Instantaneous magnetic field distribution in brushless permanent magnet DC motors, part Ⅲ. Effect of stator slotting", IEEE transactions on magnetics, Vol. 29, No.1, pp. 143-151.

[136] N. Zhao, Z.Q. Zhu and W. Liu (2011), "Comparison of rotor eddy current losses in permanent magnet motor and generator", 2011 international conference on electrical machines and systems, Beijing, China: IEEE: pp. 1-6.

[137] W. Li, H.Q and X. Zhang (2014), "Influence of rotor sleeve electromagnetic characteristics on high speed permanent magnet generator", IEEE transactions on industrial electronics, Vol. 61, No.6, pp. 3030-3037.

[138] W. Li, Y. Zhang and Y. Chan (2011) "Calculation and analysis of heat transfer coefficients and temperature fields of air cooled large Hydro-Generator rotor excitation windings", IEEE transactions on energy conversion, Vol. 26, No.3, pp. 946-952.

[139] A. Boglietti, A. Cavagnino and D. Staton (2009) "Evolution and modern approaches for thermal analysis of electrical machines", IEEE transactions on industrial electronics, Vol. 56, No.3, pp. 871-882.

[140] W. Li, S. Li and Y. Xie (2007) "Stator rotor coupled thermal field numerical calculation of induction motors and correlated factors sensitivity analysis", Proceedings of CSEE, Vol. 27, No. 24, pp. 85-91.

[141] G. Burnand, D. Araujo and Y. Perriard (2017) "Very high speed permanent magnet motors: mechanical rotor stresses analytical model", International electric machines and drives conference, Miami, USA: IEEE: 1-7.

[142] D. Xu, X. Wang and G. Li (2016) "Optimization design of the sleeve for high speed permanent magnet machine", 11th conference on industrial electronics and applications, Hefei, China: IEEE: 2531-2535.

[143] J. Wang, F. Wang, W. Bao and E. Guan (2005) "Rotor design and strength analysis of high speed permanent magnet machine", Proceedings of the CSEE, Vol. 25, No.15, pp. 140-145.

[144] J. Yon, P. Mellor, R. Wrobel. J. Booker and S. Burrow (2012) "Analysis of semipermeable containment sleeve technology for high speed permanent magnet machine", IEEE transactions on energy conversion, Vol. 27, No.3, pp. 646-653.

[145] K. Zhao and S. Qi (2017) "A simplified model reference adaptive control method for sensorless surface permanent magnet synchronous motor drives", 43rd Annual conference of IEEE industrial electronics society, Beijing, China: IEEE: 1754-1758.

[146] M. Zhou, R. Zhang, Y. Du and Q. Ge (2017) "Research on speed sensorless method for permanent magnet linear synchronous motor based on high frequency pulsating voltage signal injection", 20th International conference on electrical machines and systems, Sydney, Australia: IEEE:1-4.

[147] H. Kim, J. Son and J. Lee (2011) "A high speed sliding mode observer for the sensorless speed control of a PMSM", IEEE transactions on industrial electronics, Vol. 58, No.9, pp. 4069-4077.

[148] C. You, J. Li, X. Huang, Y Fang and J. Ma (2017) "A full speed sensorless control algorithm for interior permanent magnet synchronous motor using sliding mode observer and HF signal injection", 2017 IEEE vehicle power and propulsion conference, Belfort, France: IEEE:1-6.

[149] C. You, R. Zhang, Y. Du and Q. Ge (2017) "Speed sensorless control of maglev permanent magnet linear synchronous motor based on sliding mode observer", 20th International conference on electrical machines and systems, Sydney, Australia: IEEE:1-5.

[150] J. Ma, J. Zhao, J. Sun and C. Yan (2017) "A novel PMSM speed control scheme based on sliding mode and fuzzy disturbance observer", 43rd Annual conference of IEEE industrial electronics society, Beijing, China: IEEE: 1704-1710.